Rotary Laser Thinning of Silicon Wafer via Diffractive Optical Element

By Qingfeng Li

Supervisors Prof. Haonan Li
Dr. Yixiang Xu
Dr. Gongyu Liu
Dr. Haohua Xiu

A master thesis submitted for the degree of Master of Mechanical Engineering of University of Nottingham

Department of Mechanical, Materials, and Manufacturing Engineering

September 2024

(This page is left blank)

Abstract

Integrated circuits generate excessive heat during operation. Effective heat dissipation is necessary to maintain optimal performance and prevent overheating. The reduced silicon wafer thickness can increase circuit layer density, support multi-chip packaging, and make chips light and compact. Backside thinning technology is an effective solution to thin the non-functional side of a silicon chip without affecting the circuit function, and can be classified into Mechanical Grinding (MG), Chemical-Mechanical Polishing (CMP), and Electrochemical Mechanical Polishing (ECMP). MG suffers from low efficiency and significant tool wear due to the high hardness of silicon. CMP compromises backside uniformity and can not accurately control wafer thickness. ECMP requires complex equipment and precise control of the chemical environment. Laser thinning can effectively solve the above issues via providing high Material Removal Rate (MRR) while maintaining a smooth and uniform surface with effective management of thermal challenges. However, the problems of current laser thinning technology can include:

- **Non-Uniform Material Removal:** The Gaussian (GAU) distribution of energy at the laser's focal point results in deeper material removal in the central region of each scan path, with less material removed towards the edges.
- **Unwanted Material Generation:** High laser energy rapidly heats and cools silicon, resulting in the formation of amorphous silicon and silicon dioxide (SiO_2), which severely impacts the electrical conductivity of the silicon wafer.
- **Regenerative Effect:** Laser thinning of surfaces with pre-existing scratches or cracks can exacerbate these defects, causing them to be widened and deepened and, therefore leading to increased scrap rates and reduced processing efficiency.

To address the issues in the above thinning methods, this thesis investigates a new technique for rotational laser thinning of silicon wafers using diffractive optical element (DOE). The study begins by analysing the importance of wafer thinning technology in enhancing integrated circuit performance and explores the global thinning equipment market along with the advantages and disadvantages of the main technological methods (see Chapter 1.1). It establishes the aim of developing a novel laser thinning technology to optimize the silicon wafer manufacturing process

(see Chapter 1.2). This is followed by a literature review of the methods for thinning the back side of silicon wafers and the application of DOE (see Chapter 2.1 and 2.2), and gaps in these methods are identified (see Chapter 2.3). The paper then examines specific issues in traditional laser thinning technology (see Chapter 3.1) and proposes a new rotating laser thinning technique based on DOE beams (see Chapter 3.2), including the design of the DOE (see Chapter 3.3). An experimental platform is subsequently established (see Chapter 4.1). The study uses DOE laser beams and GAU laser beams to thin a flat surface and compares the results in terms of surface morphology, surface roughness, material behaviour, surface wettability, and ablation mechanisms (see Chapter 4.2). For non-flat surfaces, the study compares the thinning results of DOE laser beams and GAU laser beams concerning regeneration effect (see Chapter 4.3). It then explores the optimal processing parameters for laser thinning with DOE beams (see Chapter 4.4). Finally, the paper summarizes the results obtained (see Chapter 5.1) and outlines plans for future work (see Chapter 5.2).

Based on this study, the key conclusions can include:

- **Flat Surface:** The uniform energy distribution of the DOE spot effectively avoids the ridge-like projections caused by GAU spots, resulting in a smooth post-processing surface.
- **Low Roughness:** By converting traditional Gaussian laser spots into uniform linear spots, this method achieves a surface with low surface roughness.
- **Reduced By-products:** The use of DOE-based beams minimizes the formation of amorphous silicon and oxides, as confirmed by X-ray diffraction (XRD) and energy-dispersive spectroscopy (EDS) analysis.
- **Excellent Hydrophilicity:** DOE-based thinning enhances surface hydrophilicity, with consistent hydrophilic properties in all directions.
- **Regeneration Effect:** DOE-based beams effectively mitigate the replication phenomenon encountered during laser thinning of uneven surfaces, both in width and depth directions.

This innovative technology offers a promising alternative for high-quality, efficient and controlled precision machining of silicon wafer surfaces for semiconductor device manufacturing and other high-precision applications.

Acknowledgements

I would like to express my sincere gratitude to Prof. Li Haonan. During my master's degree, Prof. Li would patiently point out my problems and analyse them with me, which made me deeply aware of my weakness in experimental planning, writing and communication. He also urged me to improve the problems. This enabled me to improve very quickly in a very short period of time. In the process of setting up the experimental platform and developing the project, his rich experience provided me with valuable guidance, which enabled me to avoid many potential pitfalls. In the process of writing the thesis, Prof. Li gave me extremely detailed guidance. He not only carefully reviewed each draft of my thesis, but also continuously provided valuable feedback and encouragement. Prof. Li corrected the thesis with me in online meetings until late at night for at least five times. I was deeply moved by this effort and cherished it very much. There is no doubt that it was because of Prof. Li's meticulous guidance and rigorous high standards that I was able to successfully complete the master's program and make rapid progress.

I am also deeply thankful to Dr. Gongyu Liu from the China Beacons Institute at the University of Nottingham Ningbo China. His expertise and guidance were invaluable to me during my master's degree. Dr Liu played a key role in the design of the experimental platform and the development of the experimental protocol. As we discussed the observed phenomena and challenges encountered during the experiments, he provided insights that constantly inspired innovative and insightful solutions. His unique and professional perspective greatly enriched my understanding and advanced the project.

I would also like to express my heartfelt thanks to Dr Haohua Xiu of Ningbo University of Technology, whose invaluable help made my thesis possible. Dr Xiu's expertise in academic writing and meticulous editing were invaluable to me throughout the writing and revision process. His insightful feedback and constructive suggestions greatly improved the clarity, coherence, and overall quality of my thesis. I am deeply grateful for his dedication and support.

Finally, I wish to acknowledge the invaluable contributions of the PhD/Master students at the Advanced Manufacturing Centre. They include Bixuan Wang, Haoyu Shi, Muyang Ye, Pengyuan Guan, Kunyang Li, Yizheng Wang, Haozhong Yang, Kexin Huang. Their collaborative spirit and willingness to

assist have fostered a rich and supportive research environment, which has been instrumental in the successful completion of this study. I am also deeply indebted to my family for their unwavering love, understanding, and encouragement throughout this demanding academic journey. Their steadfast belief in my abilities has been an unwavering source of strength and motivation.

This thesis is dedicated to all those who have played a pivotal role in my academic journey, shaping my knowledge, nurturing my passion for research, and providing unwavering support along the way. I am deeply grateful to my teachers, mentors, and friends for their invaluable guidance, encouragement, and friendship. To each of them, I extend my sincerest gratitude and heartfelt best wishes for the future.

Contents

Abstract .... *I*

Acknowledgements .... *III*

Contents .... *V*

List of Figures and Tables .... *IX*

Chapter 1 Introduction *1*

1.1 Background 1

1.2 Aims and objectives 7

1.3 Thesis structure 7

Chapter 2 Literature review *10*

2.1 Silicon Wafer Backside Thinning 10

2.1.1 Mechanical Grinding 10

2.1.2 Chemical Mechanical Polishing 12

2.1.3 Electrochemical Mechanical Polishing 15

2.1.4 Dry etching 17

2.1.5 Wet etching 20

2.1.6 Laser thinning 23

2.2 Diffractive Optical Element (DOE) 25

2.2.1 Focusing DOE 25

2.2.2 Polarization DOE 27

2.2.3 Beam splitter DOE 28

2.2.4 Holographic DOE 29

2.2.5 Beam shaping DOE 31

2.3 Research Gaps 32

Chapter 3 Rotary laser thinning theoretical basis *32*

3.1 Challenges in conventional linear & rotary laser thinning 32

3.2 Rotary laser thinning based on diffractive optical elements 33

3.3 DOE design 35

3.4 Summary 39

Chapter 4 Rotary laser thinning experimental results and discussion *39*

4.1 Experiment platform 39

4.2 Flat surface thinning with DOE-based laser compared to GAU laser 41
4.2.1 Machined surface morphology 41
4.2.2 Surface roughness 43
4.2.3 Material behaviours (Amortization and oxidation)....................................45
4.2.4 Surface wettability 47
4.2.5 Different DOE-based ablation mechanisms compared with GAU laser beam....................................49
4.3 Non-flat surface thinning with DOE-based laser compared to GAU laser....................................51
4.4 Effects of process parameters in DOE-based laser thinning process 53
4.5 Summary....................................56
Chapter 5 Conclusion....................................58
5.1 Research outcomes....................................58
5.2 Future works....................................59
Reference....................................60

Abbreviations

CPU	Central processing unit
RAM	Random access memory
GPU	Graphics processing unit
LED	Light-emitting diode
MG	Mechanical Grinding
CMP	Chemical Mechanical Polishing
ECMP	Electrochemical Mechanical Polishing
pH	Potential of hydrogen
HF	Hydrofluoric acid
HNO3	Nitric acid
KOH	Potassium hydroxide
NaOH	Sodium hydroxide
TMAH	Tetramethylammonium hydroxide
DOE	Optical diffractive element
GAU	Gaussian
TTV	Total thickness variation
MRR	Material removal rates
F/H	Scratch depth and the hardness ratio
SSD	Subsurface damage
IPA	Isopropyl alcohol
AH	Ammonium hydroxide
Nd: YAG	Neodymium-doped Yttrium Aluminium Garnet
FWHM	Full width at half maximum
SEM	Scanning Electron Microscope
EDS	Energy dispersive spectrometer
XRD	X-ray diffractometer
AFM	Atomic force microscopy

Nomenclatures

ω	angular velocity
v	linear velocity
D	width of laser spot
L	Length of laser spot
d	distance between adjacent engraved lines
θ	diffraction angle
λ	wavelength of the light wave
n	diffraction order
r	diameter of the incident light
a	width of the spot target shape
f	focal length of the focusing mirror
m	refractive index of sapphire
β	inclination angle of the inclined surface of the diffraction grating groove
R_Z	maximum surface roughness
I_D	DOE-based peak single pulse energy density
μ	energy transmission coefficient of DOE
E	single pulse energy
l	length of the DOE-based beam at the intersection point
w	width of the DOE-based beam at the intersection point
I_G	GAU peak single pulse energy density
r	radius of the Gaussian beam at the focal point

List of Figures and Tables

Figure 1-1 Wafer applications ··· 1

Figure 1-2 The wafer manufacturing process ··· 2

Figure 1-3 Backside thinning equipment market size and scope ··· 3

Figure 1-4 Backside thinning mothed ··· 5

Figure 1-5 Scope of the study ··· 8

Figure 2-1 Research on mechanical grinding process. (i) A highly efficient thinning method for silicon wafers using constant-pressure diamond grinding; (ii) Exploring factors affecting surface quality; (iii) Effect of grinding speed, grinding wheel speed and feed rate on surface quality; (iv) Study on edge chipping phenomenon ··· 11

Figure 2-2 Research on chemical mechanical polishing process. (i) Effects of different crystallographic planes on material removal behaviour; (ii) Effect of chemical reaction rate on surface morphology; (iii) Effect of abrasive on surface roughness; (iv) Effect of solid-liquid reaction mode on chemical mechanical polishing performance ··· 13

Figure 2-3 Research on electrochemical mechanical polishing process. (i) A three-step slurryless ECMP process; (ii) A paddles ECMP process; (iii) A metal electrochemical corrosion process; (iv) An ECMP process using polystyrene sulfonic acid as electrolyte ··· 16

Figure 2-4 Research on dry etching process. (i) An NF3/Ar-based dry etching process; (ii) Effect of suboxide on etching rate; (iii) A plasma-based atomic layer selective dry etching process; (iv) A dry etching process using Cl2/BCl3 inductively coupled plasma ··· 18

Figure 2-5 Research on wet etching process. (i) Effect of the internal structure of batch-processed wet etching reactors on fluid flow and heat transfer; (ii) Ozone-based wet etching processes; (iii) A ultrasonic wet etching process; and (iv) A wet etching method for removing polysilicon in narrow pattern gaps ······ 20

Figure 2-6 Research on laser thinning process. (i) Effect of energy density on wafer surface quality; (ii) Influence of ambient gases on the wafer surface morphology; (iii) A backside thinning process using femtosecond laser pulses; (iv) Polarized Laser Scattering for Subsurface microcracks ······ 23

Figure 2-7 Research on focusing DOE ······ 25

Figure 2-8 Research on polarization DOE ······ 26

Figure 2-9 Research on beam splitter DOE ······ 28

Figure 2-10 Research on Holographic DOE. (i) A lens-free digital holographic microscopy technique based on DOE; (ii) A holographic imprinting technique based on DOE ······ 29

Figure 2-11 Research on Beam shaping DOE ······ 30

Figure 3-1 Conventional linear laser thinning (a) Schematic diagram of a wafer thinned using a galvanometer-moving laser spot; (b) Spot movement trajectory using a galvanometer-moving laser; (c) Visible trajectory topography of a galvanometer-thinned wafer using scanning electron microscope observation (SEM); (d) Overheated crater topography formed at an inflection point; (e) Highly protruding topography between neighbouring scanning paths; Conventional rotary laser thinning (f) Schematic diagram of a wafer thinned using a turntable; (g) Spot movement trajectory for rotary laser thinning; (h) Visible trajectory topography of a wafer thinned by rotary laser thinning using scanning electron microscopy (SEM); (i) Trenches still formed between neighbouring scanning paths ······ 34

Figure 3-2 (a) Schematic diagram of DOE-based laser thinning; (b) Diagram of spot shape; (c) DOE-based laser thinning optical path diagram; (d) Spot size and beam energy distribution at different positions ······ 35

Figure 3-3 (a) Physical figure of DOE; (b) Shape of DOE under orthogonally polarized light; (c) Shape of the focused spot after the laser passes through the DOE; (d) Schematic of the microstructure of the grating on the surface of the DOE; (e) Diffraction schematic diagram of the laser passing through the DOE; (f) Energy distribution of the focused spot ······ 38

Figure 4-1 (a) Laser thinning platform; (b) Platform details and laser head; (c) Effect of laser focus defocus ······ 40

Figure 4-2 When the pulse energy is 38 μJ and the feed rate is 0.14mm/s, (a) The surface morphology of the wafer is treated by GAU laser beam; (b) Surface morphology of DOE-based laser beam treated silicon wafer; When the pulse energy was 48 μJ and the feed rate was 0.14 mm/s, (c) GAU laser beam treated the wafer surface morphology; (d) Surface morphology of DOE-based laser beam treated silicon wafer; When the pulse energy was 58 μJ and the feed rate was 0.14 mm/s; (e) GAU laser beam treated wafer surface morphology; (f) Surface morphology of DOE-based laser beam treated silicon wafer; When the pulse energy is 58 μJ and the feed rate is 0.30mm/s; (g) GAU laser beam is used to treat the wafer surface morphology; (h) Surface morphology of DOE-based laser beam treated silicon wafer ······ 42

Figure 4-3 (a) Effect of different single pulse energies on roughness; (b) Surface morphology of silicon wafer thinned by DOE-based laser beam under different single pulse energies; (c) Surface morphology of silicon wafers thinned by GAU laser beam under different single pulse energies; (d) Effect of different thinning times on roughness; (e) Morphologies of silicon wafers thinned by DOE-based laser beam under different thinning thorns; (f) Morphology of silicon wafers thinned by GAU laser beam under different thinning spines ······ 44

Figure 4-4 Comparison of crystallinity between Gaussian spot and DOE-based linear spot; (a)

Different single pulse energy; (b) Different thinning times; Comparison of oxygen content between Gaussian spot and DOE-based linear spot; (c) Different single pulse energy; (d) Different thinning times ······ 46

Figure 4-5 (a) Contact angles of DOE-based and GAU beam-machined surfaces at different monopoles energies; (b) SEM image of surface texture processed by GAU beam; (c) SEM image of surface texture processed by DOE-based beam ······ 48

Figure 4-6 (a) Single hole ablation morphology of DOE-based beam machining; (b) DOE-based laser thinning diagram; (c) Planar morphology of DOE-based beam ablation; (d) Single hole ablation morphology of GAU beam machining; (e) GAU laser thinning diagram; (f) Planar morphology of GAU beam ablation ······ 51

Figure 4-7 (a) Groove experiment and laser principle; (b) Depth curve of groove; (c) SEM image of groove; (d) AFM image of DOE-based laser thinning final pass; (e) AFM image of GAU laser thinning final pass ······ 53

Figure 4-8 Surface depth and surface roughness curves of a wafer at different laser frequencies ·· 54

Figure 4-9 Surface depth and surface roughness curves of a wafer at rotational speed ······ 55

Figure 4-10 (a) Variation of mean depth and maximum roughness at different frequencies; (b) Variation of average depth and maximum roughness at different rotational speeds ······ 56

Table 1 DOE-based and GAU Peak Energy Density Calculations ······ 50

Chapter 1 Introduction

1.1 Background

Silicon wafers are fundamental materials for the fabrication of integrated circuits and advanced microelectronic devices [1]. Silicon wafers are widely used in (i) chips, including central processing unit (CPU), random access memory (RAM) and graphics processing unit (GPU) [2]; (ii) sensors including pressure, temperature and acceleration sensors; and (iii) optoelectronic devices, such as solar panel [3], light-emitting diode (LED), and laser (see Figure 1-1).

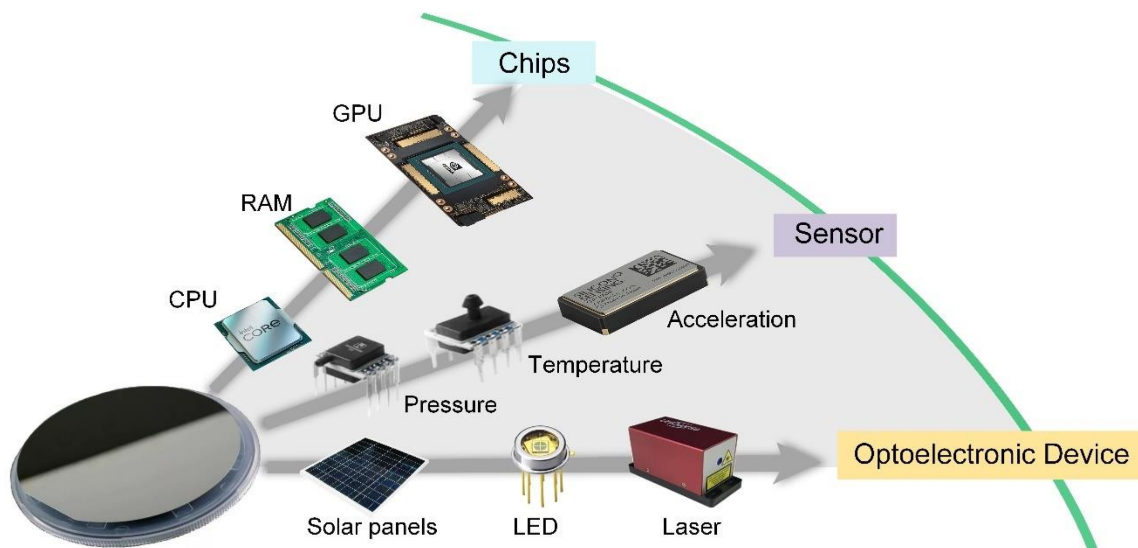

Figure 1-1 Wafer applications

To achieve these applications, silicon wafers must undergo a complex and precise manufacturing process. The process begins with crystal growth to form the ingot, followed by cutting and grinding it into a cylindrical shape, and then slicing it into wafers. The silicon wafers are subsequently ground and polished to ensure uniform thickness, smooth edges, and nanometre-level surface flatness. To enhance wafer performance and achieve the required thickness, backside thinning is necessary. Finally, the silicon wafers are diced into individual chips and packaged, becoming the core components of electronic devices [4] (see Figure 1-2).

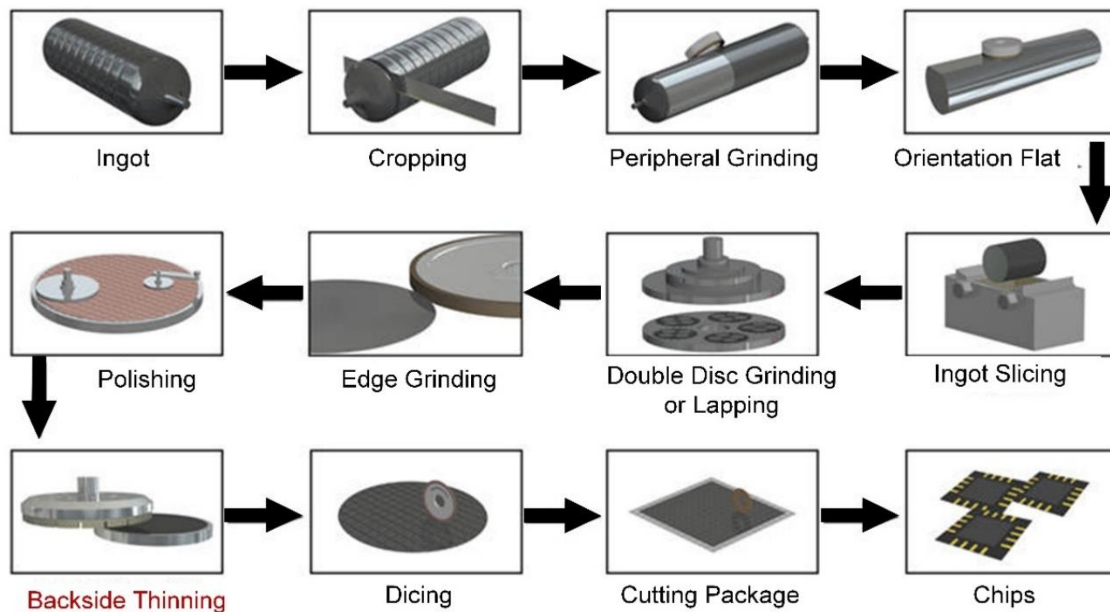

Figure 1-2 The wafer manufacturing process [4]

Backside thinning is a critical process in silicon wafer manufacturing because the wafer thickness directly affects chip thermal management [5], circuit performance [6], and surface damage [7]. Thinning wafer enhances thermal conductivity, reduces overheating during high-power operation, and helps maintain stable operating temperatures, thereby extending device longevity. Additionally, thinning wafers can decrease parasitic capacitance and resistance in circuits, improving signal transmission speed and signal integrity. Backside thinning also addresses surface defects and residual stress on the wafer's backside, enhancing overall wafer strength and stability. Additionally, it improves wafer flatness, ensuring a uniform surface. In conclusion, backside thinning is instrumental in optimizing wafer characteristics to enhance device performance, reliability, and manufacturability.

The global backside thinning equipment market plays a pivotal role in the semiconductor manufacturing industry, and its regional development shows a clear pattern of differentiation. North America, with its leading position in the field of semiconductor technology [8], occupies a market share of up to 34% [9], holding the leading position. Asia-Pacific region is followed by 30% market share, and with a compound annual growth rate of 7.55% to lead the world, which is mainly attributable to the region as a global semiconductor manufacturing centre of the rise, as well as China, South Korea and other countries on the strong demand for advanced chip technology. In 2020, the global market size of the backside thinning equipment market reached

a staggering 584.69 billion U.S. dollars, which fully highlights the importance of the market. The market size is expected to grow further to USD 615.74 billion by 2029, at a CAGR of 5.31% [9].

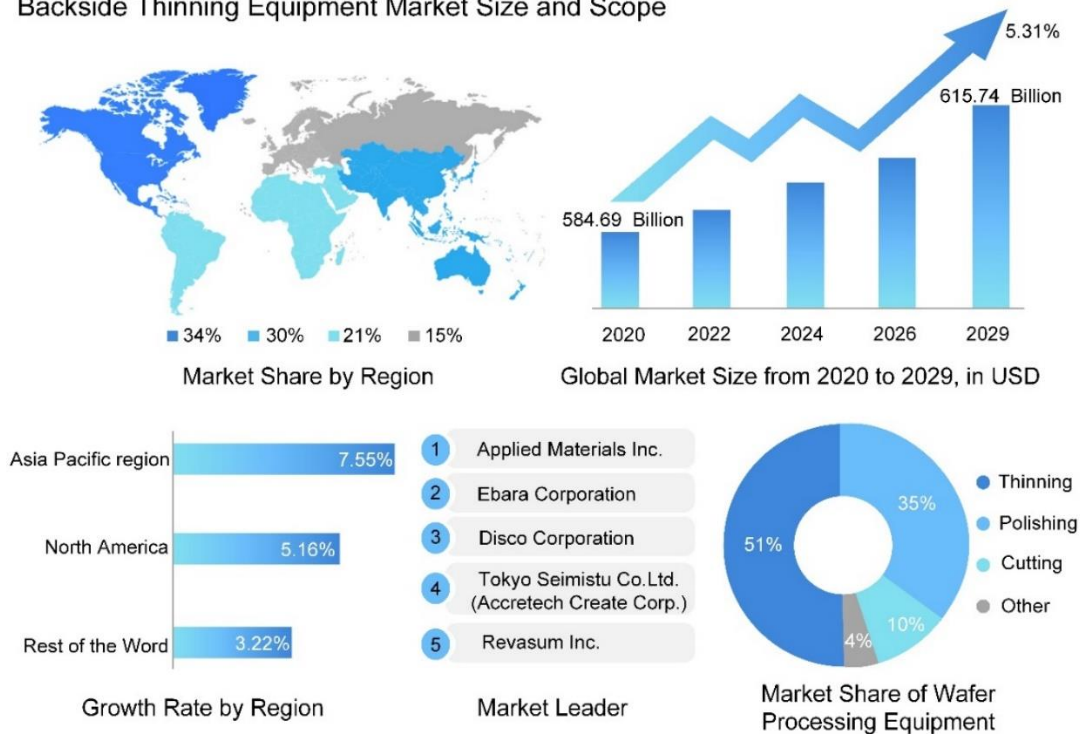

Figure 1-3 Backside thinning equipment market size and scope

The global backside thinning equipment market is highly competitive, with industry giants such as Applied Materials Inc., Ebara Corporation, Disco Corporation, Tokyo Seimitsu Co. Ltd. and Revasum Inc. Backside thinning processes accounted for a whopping 51% share of the overall wafer processing equipment market [9], underscoring their centrality to the semiconductor manufacturing process. In contrast, the polishing process occupies 35% of the market share, the cutting process accounts for 10%, and other processes account for only 4%. The demand for high-performance chips will continue growing as emerging technologies such as 5G, artificial intelligence, and the Internet of Things flourish, which will drive the expansion of the backside thinning equipment market. In addition, the continuous progress of technology (such as accurate thinning processes and high degrees of automation) will also inject a steady stream of vitality for market growth. It can be predicted that the backside thinning equipment market will continue to grow in the future, and play an increasingly important role in the semiconductor industry (see Figure 1-3).

There are general six backside thinning technologies including (i) mechanical grinding, (ii)

chemical mechanical polishing, (iii) electrochemical mechanical polishing, (iv) dry etching, (v) dry etching wet etching, and (vi) laser thinning.

Mechanical Grinding (MG) uses a rotating wheel or belt with an abrasive to grind the wafer surface. The abrasive can be a hard material such as diamond, silicon carbide or aluminium oxide. The wafer material is removed by pressing the abrasive against the wafer surface with mechanical force and rotating or reciprocating motion [10] (see Figure 1-4 a). However, MG leads to surface scratches or microcracks and is challenging to achieve nanometre-level flatness, making it unsuitable for high-precision processing requirements.

Chemical Mechanical Polishing (CMP) is a process that combines chemical and mechanical grinding to achieve backside thinning. In this process, the wafer is secured in a carrier and pressed against a rotating polishing pad, while a polishing solution containing abrasive particles and chemical reagents is applied to the pad. The rotating pad and abrasive particles remove material from the wafer surface through mechanical friction, while the chemical reagents in the solution facilitate the removal of material by reacting with the wafer surface [11] (see Figure 1-4 b). Despite its advantages in backside thinning, CMP has certain drawbacks. The process requires precise control of various parameters, including polishing pressure, polishing solution composition, and polishing pad type. Additionally, CMP equipment and consumables are costly, and the process is inefficient.

Electrochemical Mechanical Polishing (ECMP) is an advanced material removal technique that combines electrochemical passivation and mechanical grinding to achieve ultra-smooth surfaces [12]. During the ECMP process, the workpiece is set as the anode and immersed with the cathode in an electrolyte. The application of external voltage causes anodic dissolution, forming a passivation layer. Simultaneously, a rotating polishing pad applies mechanical abrasion to the workpiece, effectively removing the passivation layer and fine protrusions, resulting in high-efficiency material removal and an ultra-smooth surface with nanometre-level roughness (see Figure 1-4 c). However, ECMP also faces challenges, which require precise control of multiple parameters, including electrolyte composition, polishing pad material, voltage, current density, temperature, and pH.

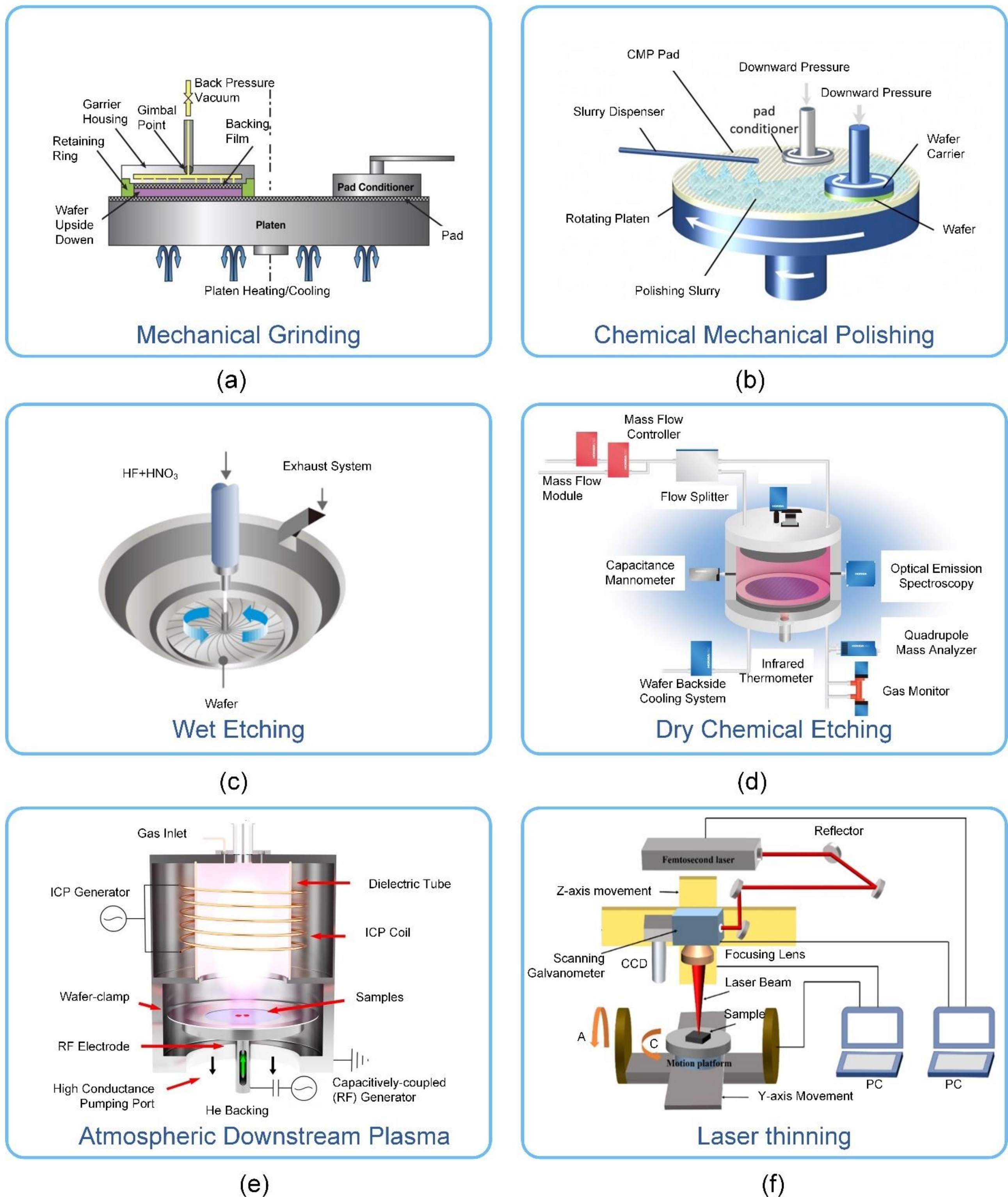

Figure 1-4 Backside thinning mothed

Dry etching is a technique used to selectively remove silicon material in a vacuum using gaseous chemicals. Silicon wafers are exposed to specific gases that react with silicon to produce volatile by-products, which remove the material [13]. By precisely controlling gas composition, pressure, temperature, and radio frequency power, dry etching can achieve precise thickness control and

uniform surfaces (see Figure 1-4 d). However, high-energy ion bombardment during the dry etching process can cause surface defects and increased roughness, potentially affecting device performance.

Wet etching involves immersing the wafer in a specific chemical solution, where the chemicals in the etching solution react with the silicon material to dissolve and remove it. Common etching solutions include mixtures of hydrofluoric acid (HF) and nitric acid (HNO3), potassium hydroxide (KOH), sodium hydroxide (NaOH), and tetramethylammonium hydroxide (TMAH) [14]. While wet etching can rapidly remove large amounts of silicon (see Figure 1-4 e), it is challenging to control the etching shape precisely, which can lead to over-etching and a rough surface. The etching solutions are corrosive and toxic, requiring proper subsequent handling.

Laser thinning is a process that uses a laser to precisely remove material from semiconductor silicon wafers to achieve a target thickness. It is a non-contact and high-precision thinning method. Laser thinning uses a high-power pulsed laser beam to irradiate the silicon wafer surface. The laser energy is absorbed by the wafer material and converted into heat, resulting in localized melting or vaporization of the material. By controlling the laser parameters (For example, power, pulse width, repetition frequency) and the scanning path, the material can be precisely removed to achieve backside thinning. Laser thinning can achieve precise thickness control, down to the sub-micron level. At the same time, non-contact thinning avoids the tool loss, material damage and environmental contamination that can be caused by mechanical thinning [15]. It is also possible to selectively thin specific areas to achieve complex geometries (see Figure 1-4 f). In laser thinning, most studies rely on laser beams with Gaussian energy distribution, the non-uniform energy distribution of Gaussian laser beams can result in uneven material removal, making it difficult to achieve the desired flatness, which can lead to numerous defects affecting surface quality in actual processing.

Each of the above six backside thinning methods has its drawbacks. MG can cause surface scratches or micro-cracks. CMP involves high equipment and consumable costs. ECMP requires precise parameter control and has a low material removal rate. Dry etching can result in surface damage. Wet etching may lead to surface roughness and over-etching. Traditional laser thinning methods rely on Gaussian energy distribution, resulting in uneven material removal. In contrast,

laser beams based on DOE can achieve uniform energy distribution, producing a consistent beam profile. Compared to the six methods mentioned above, the laser thinning method based on DOE beams offers unique advantages such as a smooth surface, high thinning efficiency, minimal surface damage, no tool wear, and high processing precision, making it worthy of in-depth study in this thesis. Therefore, this thesis explores a new technique using rotating lasers with DOE-based beams for thinning silicon wafers.

1.2 Aims and objectives

In order to address the problems that arise during laser backside thinning and with the aim of eliminating these defects, this research project specifically explores the following areas:

- Explore the specific defects that occur in conventional Gaussian laser thinning of silicon wafers.
- Propose a new laser thinning method to eliminate these defects and to improve the backside thinning efficiency and quality.
- Build a new laser thinning machine to achieve high precision thinning function.
- Conduct comparison experiments for flat wafer surfaces between the new and traditional backside thinning method, to verify the feasibility and advantages of the new method.
- Conduct comparative experiments for uneven wafer surfaces between the new and traditional backside thinning method, to confirm the feasibility and advantages of the new method under actual processing conditions.
- Explore the optimal process parameters of the new processing method and the effects of different process parameters on the surface quality of the workpiece.

1.3 Thesis structure

To address the shortcomings of the traditional laser thinning process, this thesis aims to explore the new DOE-based rotary laser thinning technology from the aspects of design, fabrication, mechanism, and process parameters. The context of this thesis is as follows (see Figure 1-5):

Chapter 1 provides a general introduction, covering the background of silicon wafer backside

thinning, market demand, the advantages and disadvantages of various backside thinning methods, and the associated issues (Section 1.1). Section 1.2 discusses the research content and directions proposed to address these issues. Section 1.3 explains the structure of the thesis.

Chapter 2 presents a detailed literature review on silicon wafer backside thinning (Section 2.1) and the application of DOE (Section 2.2). Section 2.3 identifies the research gaps.

Chapter 3 investigates the issues associated with traditional laser thinning and conventional rotary laser thinning (Section 3.1). It proposes a new rotating laser thinning technique based on DOE beams (Section 3.2) and designs the DOE.

Chapter 4 establishes the experimental platform for rotating laser thinning using DOE beams (Section 4.1). It uses both DOE and GAU beams to thin flat and uneven surfaces. For flat surfaces, it compares the differences and advantages of the two beams in terms of surface morphology, surface roughness, material behaviour, surface wettability, and ablation mechanisms (Section 4.2). For uneven surfaces, it explores the differences in replication phenomena during thinning of grooves and compares the processing efficiency of the two beams (Section 4.3). It also examines the effect of processing parameters in DOE-based thinning on surface roughness and thinning depth (Section 4.4).

Chapter 5 summarizes the research work and discusses the research findings (Section 5.1), and outlines plans for future work (Section 5.2).

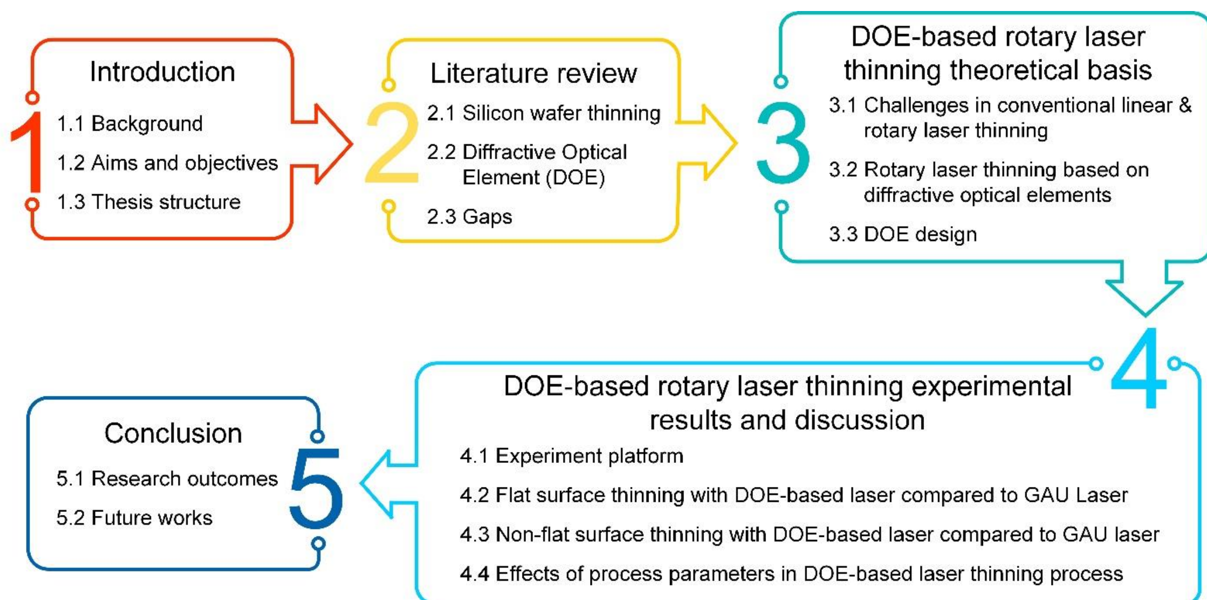

Figure 1-5 Scope of the study

Chapter 2 Literature review

2.1 Silicon Wafer Backside Thinning

The silicon wafer backside thinning process refers to the reduction of the thickness of silicon wafers to the desired level, down to tens of micrometres or even thinner, during semiconductor manufacturing. This technology is crucial for meeting the requirements of various chip packaging formats, enhancing the processing speed and storage capacity of integrated circuit chips. The thinning process involves several methods, including (i) Mechanical Grinding, (ii) Chemical Mechanical Polishing, (iii) Electrochemical Mechanical Polishing, (iv) Dry etching, (v) Wet etching, and (vi) Laser thinning.

2.1.1 Mechanical Grinding

Mechanical Grinding (MG) is a crucial precision surface finishing technique that plays a vital role in achieving ultra-smoothness and high reflectivity on silicon wafer surfaces. MG is an effective method for achieving the backside thinning of silicon wafers. However, the MG process also leads to low surface quality and surface damage.

To address the issue of low surface quality, Li et al. [16] proposed a highly efficient thinning method for silicon wafers using constant-pressure diamond grinding. By adjusting the applied pressure, they achieved high material removal rates, and superior surface quality. This technique produced wafers with surface roughness below 2 nm and surface stress below 200 MPa (see Figure 2-1 a). Additionally, Yang et al. and Sun et al. explored the factors influencing surface quality during the MG process. Yang et al. [17] studied the evolution of single-crystal silicon surface morphology with varying particle sizes, revealing distinct effects of different abrasive particle sizes on surface roughness. While 50 nm particle initially smoothened the surface faster, 20 nm particle ultimately achieved lower surface roughness (see Figure 2-1 b). Sun et al. [18] investigated the factors influencing surface quality during the self-rotating grinding of silicon wafers, exploring the effects of grinding speed, wheel speed, and feed rate. Their results demonstrated that increasing wheel speed reduces surface roughness, while

increasing wafer speed and feed rate lead to increased roughness. Furthermore, the radial distance on the wafer also played a role, with edge regions exhibiting higher roughness than the centre (see Figure 2-1 c). Based on this phenomenon, Zhang et al [19] employed finite element modelling to explore the formation mechanism of centre depressions during silicon wafer grinding in MG. Their research revealed that using grinding wheels with higher Young's modulus, optimizing chuck shape, and reducing grinding force can effectively minimize or eliminate depressions. To detect the presence of depressions, Chen and Hsu [10] developed a wafer thinning process model to estimate the total thickness variation (TTV) of wafers during MG. Their experimental results showed that the model successfully predicted TTV values below 3 μm under specific grinding parameters, approaching the ideal state of 0 μm TTV.

To address the issue of surface damage, Gao et al. [20] established a mathematical model to analyse wafer warpage during ultra-precision MG, to reduce surface damage, considering factors such as processing stress, wafer thickness, damage layer thickness, and material properties. They successfully predicted wafer warpage behaviour, providing a theoretical foundation for understanding and predicting surface damage during grinding. Gao et al. [21] experimentally investigated the phenomenon of edge chipping, a form of surface damage during silicon wafer MG and identified the critical thickness that leads to chipping, along with its relationship to the grinding mode. Their findings indicated that down-grinding effectively reduced edge chipping and minimized surface damage. Additionally, the chip size decreased as wafer thickness increased (see Figure 2-1 d). The generation of chips can be related to the brittle nature of the silicon wafer. Cheng and Dong [22] investigated the surface formation mechanisms and grinding force prediction models for microscale MG of silicon wafers. Their experiments revealed a transition from plastic to brittle behaviour during micro-grinding, providing a theoretical basis for microscale machining of hard and brittle materials. Additionally, to address the issue of surface damage caused by grinding marks, Pei et al. [23] proposed an improved grinding technique for manufacturing flatter and cost-effective silicon wafers. Their experiments demonstrated that soft pad grinding effectively removed wire saw marks, and a 7 μm polishing removal was sufficient to eliminate grinding marks. The resulting wafer flatness met the stringent specifications of future silicon wafers, offering new possibilities for efficient and low-cost wafer manufacturing in the semiconductor industry.

In conclusion, many researchers have made significant contributions to the mechanical processing of silicon wafers, particularly in improving surface quality and reducing surface damage. However, low machining efficiency and the susceptibility of wafers to cracking when excessively thinned remain significant challenges.

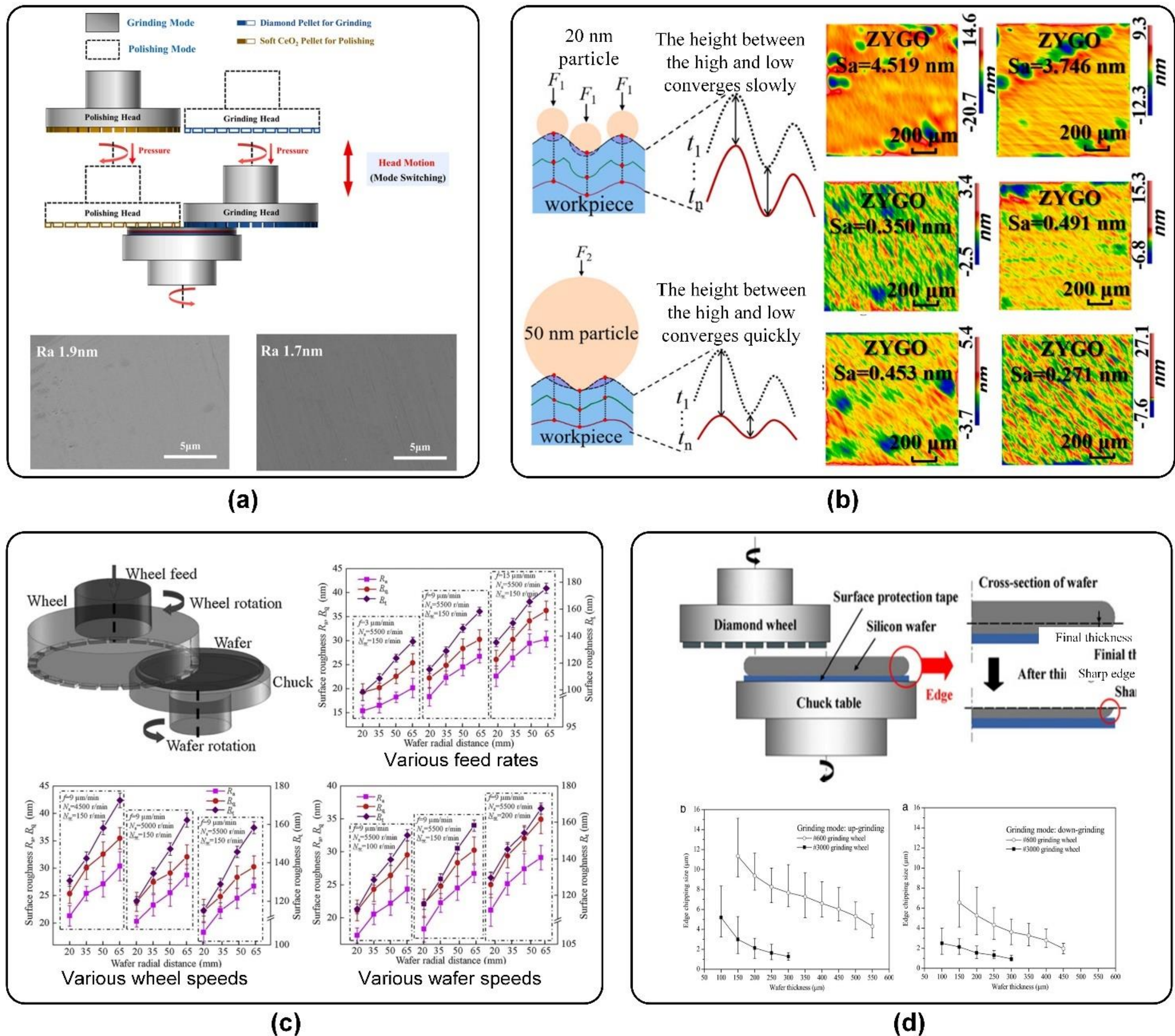

(Source: a [16], b [17], c [18], d [21])

Figure 2-1 Research on mechanical grinding process. (a) A highly efficient thinning method for silicon wafers using constant-pressure diamond grinding; (b) Exploring factors affecting surface quality; (c) Effect of grinding speed, grinding wheel speed and feed rate on surface quality; (d) Study on edge chipping phenomenon

2.1.2 Chemical Mechanical Polishing

Chemical Mechanical Polishing (CMP) plays a crucial role in semiconductor manufacturing and high-

precision machining. CMP is a process that combines mechanical grinding with chemical methods. Compared to MG, CMP offers higher polishing efficiency. However, CMP technology also faces challenges such as low surface quality, surface damage, and low material removal rates (MRR).

To improve surface quality, Xie et al. [24] explored the influence of different crystallographic planes of CeO_2 on silicon material removal behaviour during CMP. Experimental results demonstrated a positive correlation between scratch depth and the hardness ratio (F/H), and a negative correlation between scratch depth and surface roughness, confirming that the CeO_2(111) crystal plane exhibits the ability to improve surface quality due to its higher hardness and friction (see Figure 2-2 a). Additionally, Yang et al. [17] investigated the evolution of wafer surface quality during CMP from the perspective of chemical reaction rates. Single-crystal silicon wafers were subjected to CMP using slurries with pH values of 10 and 11. Results showed that during the initial 20 minutes of polishing, the mid-to-high spatial frequency roughness of the wafer polished with the pH 11 slurry decreased more rapidly compared to the pH 10 slurry. Subsequently, the pH 11 slurry achieved the minimum roughness first, while the mid-to-high spatial frequency roughness of the wafer polished with the pH 10 slurry continued to decrease, reaching its minimum at 40 min. This study highlights the role of higher chemical reaction rates in improving surface quality (see Figure 2-2 b). Gao et al. [25] approached the issue from the perspective of abrasive materials, they successfully synthesized a series of non-spherical SiO_2 abrasives with controlled size and ordered mesoporous structure using the Stober extension method. These abrasives, when applied to sustainable CMP of wafers, exhibited superior elastic deformation capability and surface precision cutting performance due to their unique mesoporous and rod-like structure, achieving a wafer surface roughness of 0.259 nm and a maximum peak-to-valley difference of only 1.36 nm (see Figure 2-2 c). Hooper et al. [26] examined the impact of pad properties on surface quality, finding that pad performance degrades during polishing due to plastic deformation, resulting in reduced polishing rate and planarity.

To address the issue of surface damage, Zhang et al. [27] compared the effects of solid-solid and solid-liquid reaction modes on CMP performance. Their findings revealed that under identical conditions, the solid-liquid reaction mode yielded a significantly lower wafer surface roughness of 0.45 nm compared to 0.64 nm for the solid-solid mode. (see Figure 2-2 d). To further understand the issue of surface damage, Liang et al. [7] explored wear phenomena during CMP, investigated the

wear phenomena during the CMP process. Their research found that surface damage during the wear process may be attributed to the unevenness of the polishing pad surface and the contact points under high pressure.

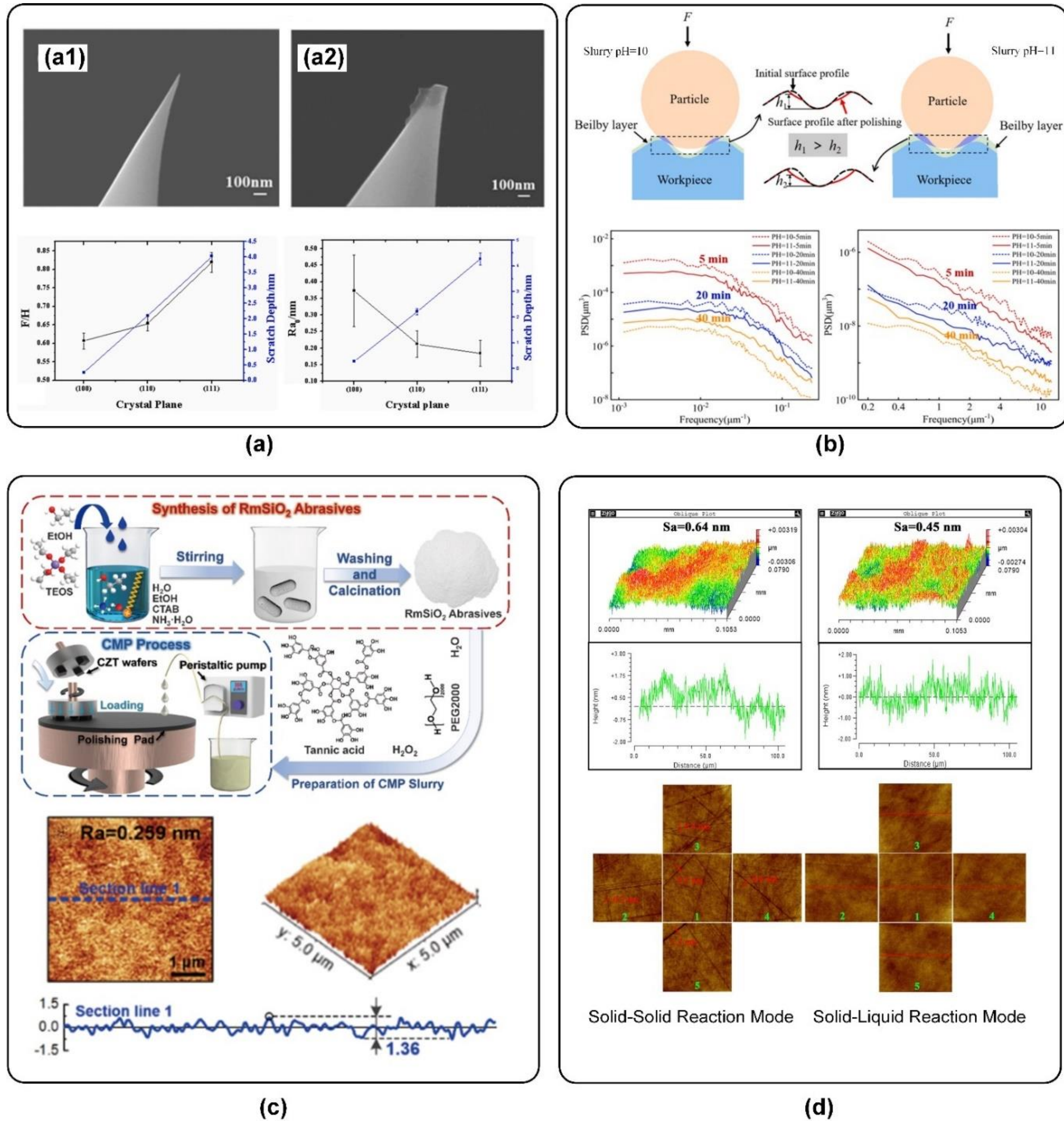

(Source: a [24], b [17], c [25], d [27])

Figure 2-2 Research on chemical mechanical polishing process. (a) Effects of different crystallographic planes on material removal behaviour; (b) Effect of chemical reaction rate on surface morphology; (c) Effect of abrasive on surface roughness; (d) Effect of solid-liquid reaction mode on chemical mechanical polishing performance

To improve the MRR, Chen et al. [28] proposed a novel model to investigate the impact of abrasive deformation on MRR during the CMP process. This model accurately predicted the correlation

between MRR and abrasive deformation, enhancing understanding of the CMP process. Park et al. [29] analysed the fluid dynamics of the CMP process, and the results indicated that by adjusting the pressure distribution of the polishing slurry, as well as the roll and pitch angles of the wafer, MRR during the CMP process can be effectively controlled. Forsberg [30] investigated the non-linear influence of process parameters on MRR during CMP, revealing a sub-linear increase in MRR with increasing applied pressure, platen speed, and silica concentration in the slurry, which provided valuable guidance for process optimization. Kwon et al. [31] demonstrated that frictional heat generated during CMP affects both MRR and the performance of consumables such as pads and slurries. Wang et al. [32] proposed a nanosecond laser irradiation-assisted CMP process for wafer polishing, achieving a significant enhancement in MRR, with a maximum rate of 9.22 μm/h. Lee et al. [33] introduced a method to improve CMP wastewater treatment and enhance MRR by modifying CMP consumables, addressing the environmental impact of CMP and proposing strategies for reducing environmental burden, thus promoting the sustainable development of CMP technology.

In conclusion, many researchers have made significant contributions to chemical-mechanical polishing of silicon wafers, especially in terms of improving surface quality, reducing surface damage and improving MRR. However, the environmental problems caused by chemicals in chemical mechanical polishing are still challenging.

2.1.3 Electrochemical Mechanical Polishing

Electrochemical Mechanical Polishing (ECMP) is an advanced wafer surface treatment technique that combines electrochemical passivation and mechanical grinding to achieve an ultra-smooth surface. However, improving surface quality, reducing surface damage, and enhancing MRR remain challenges for this technology.

Surface roughness is still an important factor affecting surface quality. To reduce surface roughness, Chen and colleagues [34] conducted in-depth studies on the working mechanisms of ECMP, which revealed the formation of a passivation film on the metal surface under electrochemical action, followed by the removal of this film through mechanical abrasion, resulting in a reduction in surface roughness. Yang [35] and his team introduced a slurry less ECMP technique utilizing a #8000 cerium oxide sintered grinding stone and a current density of 10 mA/cm² in a sodium chloride aqueous

solution. This method achieved an ultra-smooth surface. with a reduction in wafer surface roughness from 286 nm to 1.352 nm. Building upon this work, Yang [36] and his team proposed a three-step slurry less ECMP technique. The first step employed fixed abrasive ECMP to rapidly remove subsurface damage (SSD) and waviness induced during the wafer cutting process, reducing surface roughness to 24.45 nm. The second step utilized a cerium oxide grinding stone for ECMP to further remove residual SSD and achieve a surface roughness of 0.82 nm. The final step involved low-potential ECMP to ultimately reduce surface roughness to 0.11 nm. This three-step slurry less ECMP method enabled rapid transformation of unprocessed wafers into atomically smooth surfaces, potentially reducing costs and labour requirements in wafer manufacturing (see Figure 2-3 a). Additionally, Murata [37] and his team proposed an innovative paddles ECMP technique, utilizing specially designed polyurethane-cerium oxide (PU-CeO_2) core-shell particles for efficient wafer polishing. Compared to conventional CMP, this method demonstrated higher polishing efficiency, reducing wafer surface roughness from 5.43 nm to 0.51 nm (see Figure 2-3 b).

To reduce surface damage, Luo et al. [38] investigated a method based on metal electrochemical corrosion. Polishing experiments conducted in deionized water and Na_2SO_4 solution demonstrated superior polishing performance in the electrolyte, resulting in a smooth wafer surface, significantly reduced scratch depth, and minimized surface damage (see Figure 2-3 c).

To enhance MRR, Inada et al. [39] proposed an ECMP technique employing polystyrene sulfonic acid as the electrolyte, demonstrating high MRR of 37 and 14 μm/h for 2-inch and 4-inch wafers, respectively (see Figure 2-3 d). Murata's [40] team developed an environmental-friendly and highly efficient paddles ECMP method, employing a conductive composite pad composed of solid polymer electrolyte and CeO_2 particles. This approach achieved a high MRR of approximately 15 μm/h, nearly 10 times that of CMP. Yang [41] and his team presented a novel selective ECMP method using porous materials impregnated with electrolyte, addressing the limitation of conventional slurry less ECMP in processing curved surfaces. This method achieved an MRR of 4.5 μm/h within 20 minutes. On this basis, Yang [42] and his team investigated the influence of electrolyte type and concentration on wafer anodization in slurry less ECMP. The results indicated that with the increase in electrolyte concentration, the uniformity of anodic oxidation and the compactness of the formed oxide layer were improved, which enhanced MRR in the ECMP process.

In conclusion, significant progress has been made by numerous researchers in the field of ECMP for silicon wafers, particularly in enhancing surface quality, reducing surface damage, and increasing MRR. However, the complex nature of the ECMP process remains a critical issue that needs to be addressed.

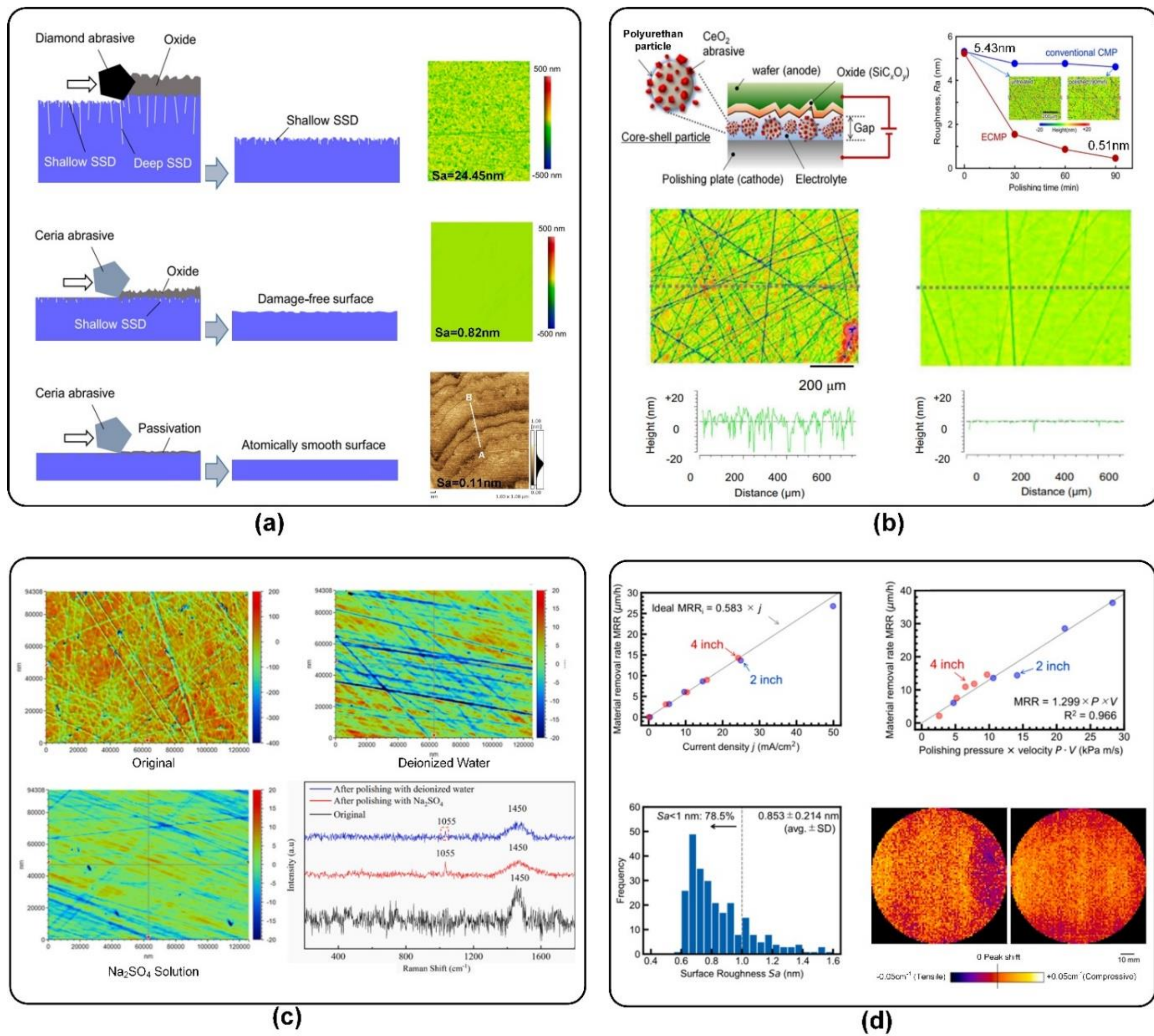

(Source: a [36], b [37], c [38],d [39])

Figure 2-3 Research on electrochemical mechanical polishing process. (a) The three-step slurry less ECMP process; (b) The paddles ECMP process; (c) The metal electrochemical corrosion process; (d) The ECMP process using polystyrene sulfonic acid as electrolyte

2.1.4 Dry etching

Dry etching technology is one of the cornerstone techniques for achieving miniaturization and functional diversification of integrated circuits. This technology employs the chemical reactivity of

plasma to selectively remove wafer surface materials through the combined effects of physical sputtering and chemical reactions. As the demand for semiconductor manufacturing continues to grow, it is crucial to enhance etching rate, improve surface quality, and minimize surface damage.

One of the primary challenges faced by dry etching technology is its low etching rate. To improve etching rate, Baik and Peaeton [43] investigated the dry etching characteristics of wafers intended for blue/green light-emitting diode (LED) fabrication under Cl_2/Ar plasma chemistry. Their findings revealed that Cl_2 gas significantly enhances the wafer etching rate, with a chemical enhancement factor exceeding 40. Cecchetto and colleagues [44] developed an NF_3/Ar-based dry etching technique that employs a multi-step process to efficiently remove saw damage and achieve surface texturing on silicon wafers within a short timeframe, resulting in high etching rate and reduced reflectivity (see Figure 2-4 a). Lee et al. [45] studied the characteristics of etching residues on the upper sidewalls after anisotropic dry etching of silicon, which revealed that increasing Cl_2 content leads to an increase in SiO_2 and suboxide residues, with a corresponding increase in etching rate (see Figure 2-4 b). Streller et al. [46] investigated photon-induced dry etching of Si (100) wafers using synchrotron radiation in the vacuum ultraviolet range. Their study found that high-resolution etching on Si wafers can be achieved when illuminated with specific wavelengths of light, with etching rate significantly increasing as the wavelength decreases. Etching rate is extremely high for wavelengths shorter than 122 nm.

To improve surface quality, Han et al. [47] utilized real-time ellipsometry to analyse the evolution of interfacial roughness during high-concentration Cl_2 dry etching of silicon wafers, establishing a linear relationship between ellipsometry parameters and RMS roughness. This provided a novel non-destructive method for in-situ monitoring and optimization of the etching process. Jiang [48] and colleagues proposed a kinetic etching front instability mechanism to explain the development of surface roughness during dry etching, which demonstrated that the three-dimensional island growth of etch inhibitors can induce surface roughness. Zhang et al. [49] developed a plasma-based atomic layer selective dry etching technique. The technique achieved an ultra-low surface roughness (0.527 nm) and an exceptionally high material removal rate (93.01 μm/min) (see Figure 2-4 c).

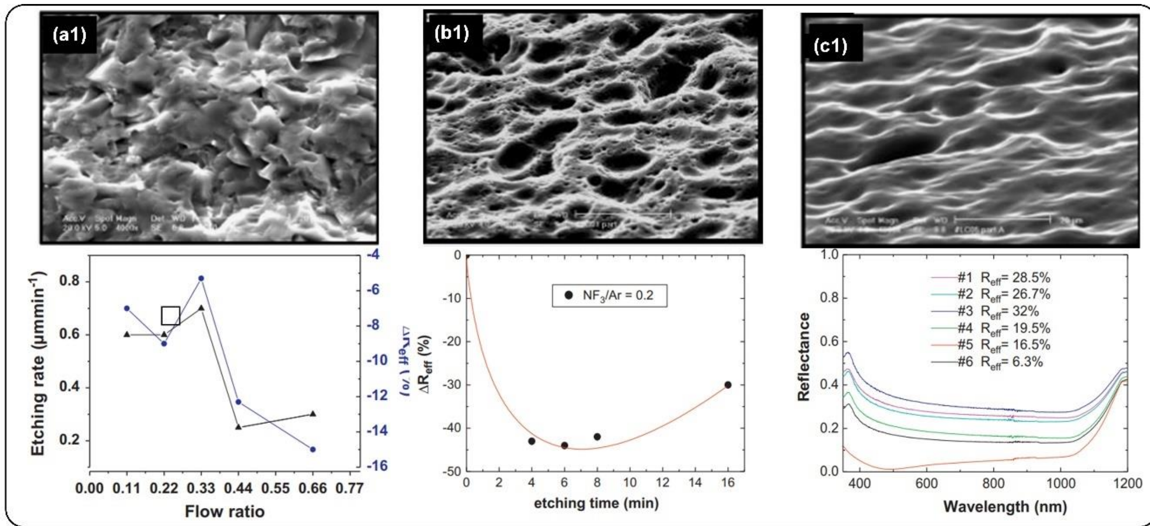

(a)

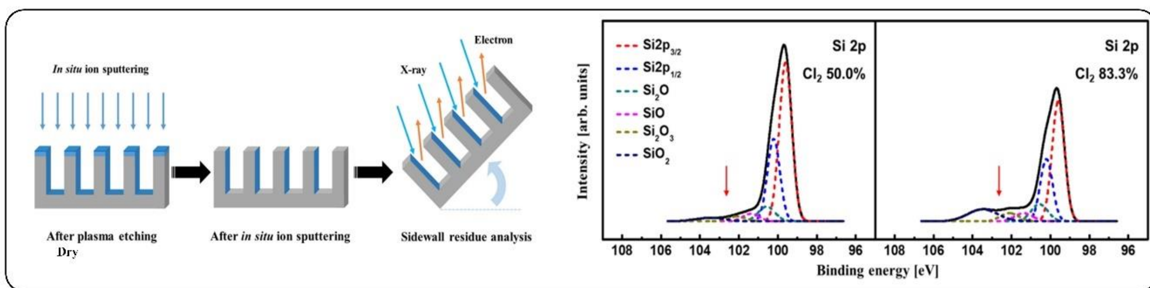

(b)

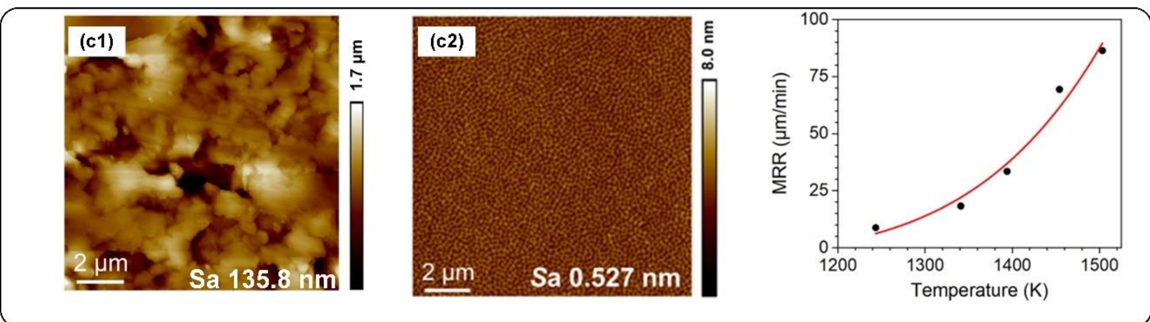

(c)

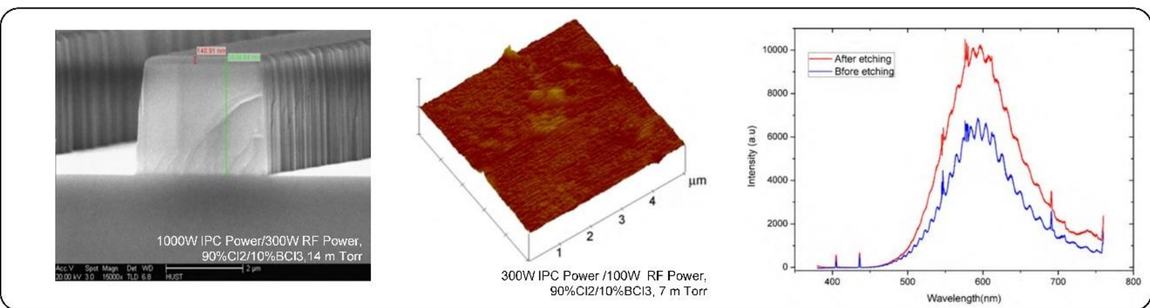

(d)

(Source: a [44], b [52], c [49], d [52])

Figure 2-4 Research on dry etching process. (a) The NF3/Ar-based dry etching process; (b) Effect of suboxide on etching rate; (c) The plasma-based atomic layer selective dry etching process; (d) The dry etching process using Cl_2/BCl_3 inductively coupled plasma

Subsurface vacancy defects are a type of surface damage. To address this issue, Heinke et al. [50] explored a novel dry etching technique capable of maintaining the atomic order of the silicon surface while forming a thin (about 2 nm) silicon oxyfluoride layer, preventing surface roughening and subsurface vacancy defects formation. Inoue et al. [51] investigated the application of dry etching for backside thinning, which demonstrated that SF_6-based dry etching can effectively reduce subsurface vacancy defects. Zhou et al. [52] employed Cl_2/BCl_3 inductively coupled plasma for dry etching of wafers, exploring the influence of process parameters on etching characteristics and analysing plasma-induced wafer damage using photoluminescence (PL) measurements (see Figure 2-4 d).

In conclusion, significant progress has been made by numerous researchers in the field of dry etching for silicon wafers, particularly in enhancing etching rate, improving surface quality, and reducing surface damage. However, minimizing surface damage during the dry etching process remains a critical challenge that needs to be addressed.

2.1.5 Wet etching

Wet etching plays a crucial role in the backside thinning of silicon wafers and directly impacts the performance and manufacturing cost of semiconductor devices. Wet etching involves immersing the wafer into a specific chemical solution, where the chemical substances in the solution react with the silicon material to dissolve and remove it. In the wet etching process, the primary issues are poor etching uniformity, low surface quality, and slow etching rate.

To address the issue of poor etching uniformity, Chein et al. [53] designed an innovative single-wafer wet etching processor that incorporates an upper heating plate to maintain the high temperature of the phosphoric acid etchant, addressing the issue of poor etching uniformity. Deng [54] and colleagues investigated the influence of internal structures within batch-processing wet etching reactors on fluid flow and heat transfer. They developed a three-dimensional computational fluid dynamics model that considers the heat generation of the wet etching reaction, which revealed that optimizing the inlet angle and wafer quantity can achieve optimal temperature and etching uniformity (see Figure 2-5 a). Monteiro [55] studied the effect of isopropyl alcohol (IPA) availability on the final structure during anisotropic wet etching of silicon wafers, proposing a dynamic wet

etching method for precise control of the etching process and mitigation of non-uniformities caused by IPA concentration variations. Additionally, Mohr et al. [56] investigated the causes of surface non-uniformity in silicon wafers during ozone-based wet etching processes and developed a model that accounted for the effects of the water layer and the processing system. Their study found that the primary cause of surface non-uniformity was the uneven removal of the water layer and the shadowing effects caused by the rapid movement of the processing system (see Figure 2-5 b).

To address surface quality issues caused by surface roughness, Bauhuber et al. [57] investigated an isotropic wet etching process for fabricating deep channels with optical surface quality on silicon wafers. By selecting an appropriate etching mixture and employing a rotating etching tool, they successfully fabricated semicircular microfluidic channels with depths of 300 mm and roughness ranging from 10 nm to 22 nm. Zeng [58] and colleagues developed a ultrasonic wet etching process for backside thinning silicon wafers, achieving ultra-thin wafers with significantly reduced stress and surface roughness (see Figure 2-5 c).

To increase the etching rate, Habuka et al. [60] developed a numerical model to calculate the etching rate of oscillating nozzles in single-wafer wet etching. This model specifically focused on the application of oscillating nozzles during the etching process on silicon wafer surfaces. The research results indicated that the position of the nozzle oscillation had a significant impact on the etching rate, with the maximum etching rate occurring particularly at the outer edge of the nozzle's oscillation. Qin and Li [61] proposed a quantitative mechanism for removing surface particles from silicon wafers using a wet chemical cleaning process. Their study determined that the optimal etching rate is approximately 0.25 nm/min. Shin et al. [59] examined a wet etching method for removing polysilicon in narrow pattern gaps, revealing that chemical concentration, particularly hydroxide ion concentration, was a primary factor influencing the etching rate. They optimized the concentration and temperature of TMAH solution, achieving a significantly higher etching rate compared to ammonium hydroxide (AH) solution (see Figure 2-5 d). Staudegger et al. [62] investigated the wet etching of bare silicon wafers under a configuration involving wafer rotation and vertical etchant jet impingement at the wafer centre, revealing the radial distribution of the etching rate.

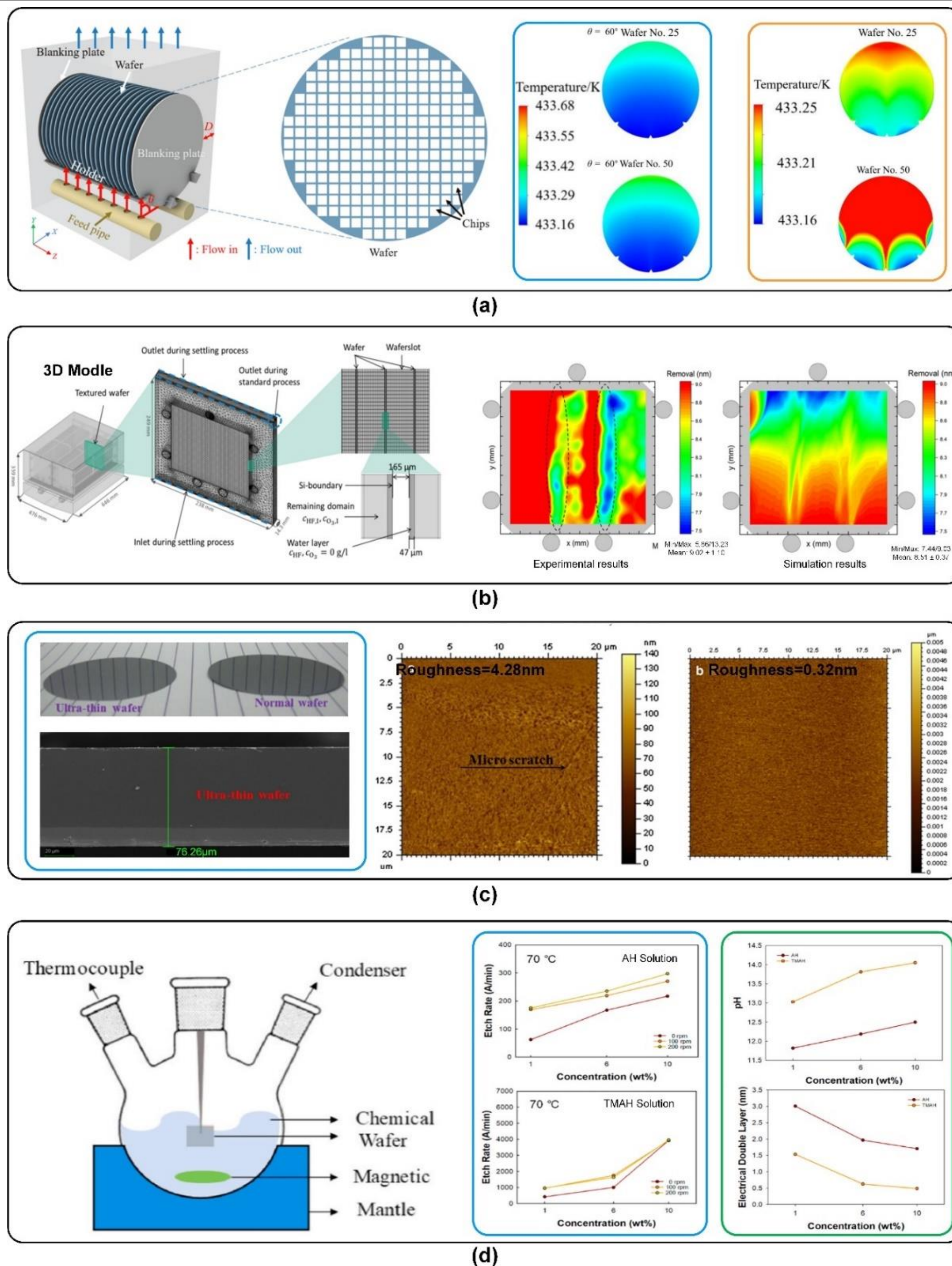

(Source: a [54],b [56],c [58],d [59])

Figure 2-5 Research on wet etching process. (a) Effect of the internal structure of batch-processed wet etching reactors on fluid flow and heat transfer; (b) Ozone-based wet etching processes; (c) The ultrasonic wet etching process; and (d) The wet etching method for removing polysilicon in narrow pattern gaps

In conclusion, numerous researchers have explored the field of wet etching for silicon wafers, making progress particularly in addressing issues such as poor surface uniformity, low surface quality, and slow etching rate. However, achieving precise control over etch depth in dry etching processes remains a significant challenge.

2.1.6 Laser thinning

Laser thinning is a commonly used method for back thinning of wafers and is a non-contact, high-precision processing technique. This method removes material from the wafer surface through the thermal or photochemical effects resulting from the interaction between the laser and the material, thereby achieving precise thickness reduction. However, enhancing surface quality and minimizing surface damage remain significant challenges in the laser thinning process.

Reducing surface roughness is one of the approaches to enhancing surface quality. Therefore, Huang and colleagues employed laser thinning to process single-crystal silicon surfaces, achieving various surface morphologies ranging from protrusions to smooth surfaces and grooves by precisely controlling the laser energy density. Their results demonstrated that laser thinning could effectively reduce surface roughness (from 6 nm to 0.7 nm), enhancing quality of the silicon surface [15] (see Figure 2-6 a). Chen et al. [63] studied a laser pre-treatment process that significantly enhances the efficiency of laser thinning, achieving a wafer surface roughness of 4.5 nm within a few hours. To improve wafer surface quality, Yuan [64] and his colleagues, as well as Zheng et al., conducted related studies. Yuan and colleagues investigated a femtosecond laser thinning system, focusing on the impact of laser incident angle on the processed surface. By optimizing laser parameters, they significantly improved the surface quality of the material and reduced processing defects. Zheng et al. [65] proposed an ultrasonic vibration-assisted femtosecond laser thinning method, demonstrating that it significantly improves wafer surface quality compared to single femtosecond laser thinning. In addition, smooth and pit-free are factors in assessing surface quality. Wang et al. [66] investigated the influence of ambient gas on material surface morphology during laser thinning. By developing an improved numerical model, they analysed the evolution mechanisms of single-crystal silicon surface morphology during laser thinning in air and argon atmospheres. Their findings revealed that the ambient gas significantly affects the laser thinning outcome, with smoother surfaces obtained in an argon atmosphere (see Figure 2-6 b). Zheng et al. [67] explored a novel backside thinning method using femtosecond laser pulses, analysing and optimizing the influence of different laser processing parameters on the machined surface. They achieved smooth, flat, and pit-free surfaces under optimized parameter combinations (see Figure 2-6 c).

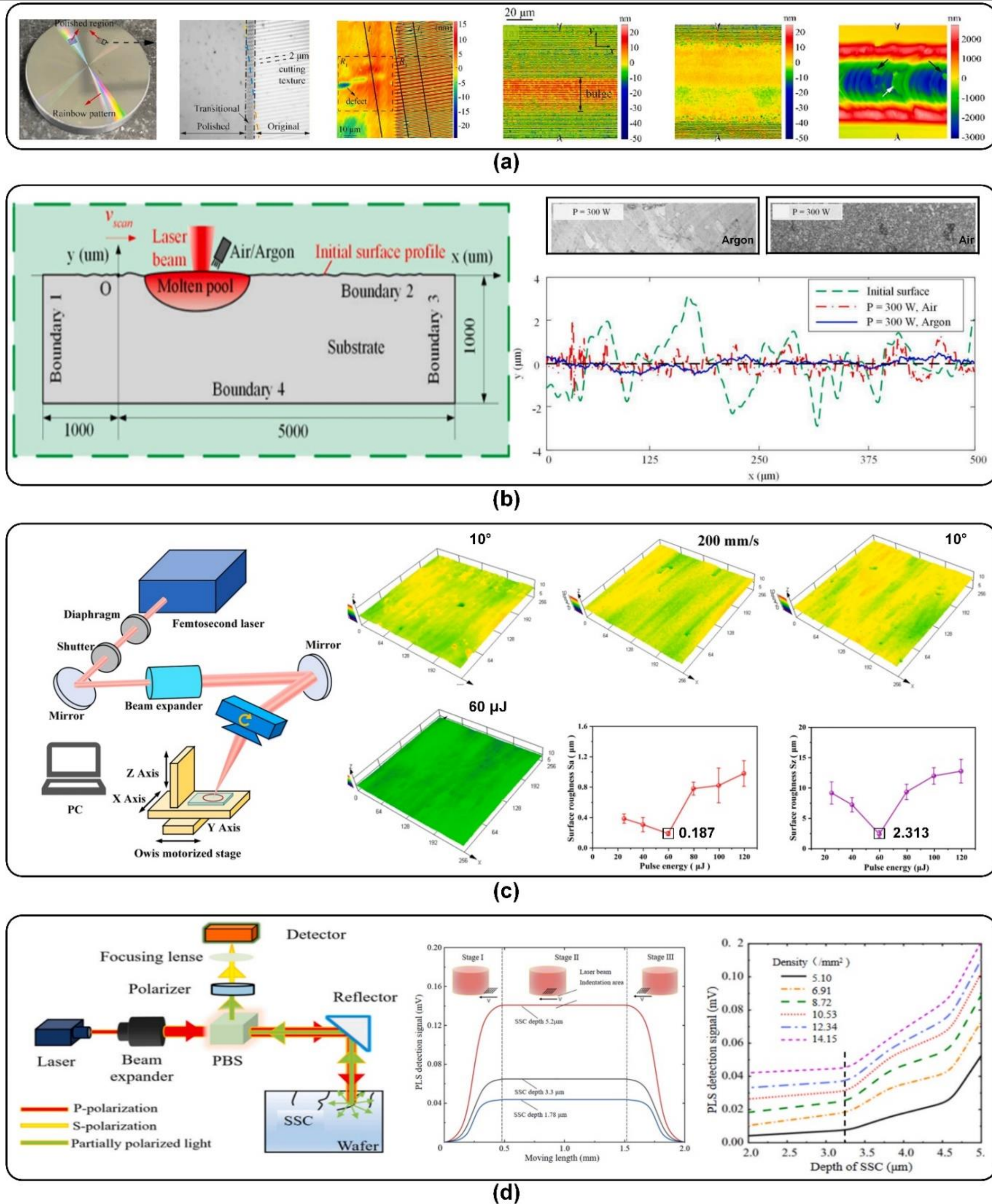

(Source: a [15],b [66],c [67],d [68])

Figure 2-6 Research on laser thinning process. (a) Effect of energy density on wafer surface quality; (b) Influence of ambient gases on the wafer surface morphology; (c) A backside thinning process using femtosecond laser pulses; (d) Polarized laser scattering for subsurface microcracks

Subsurface microcracks are a type of surface damage. To minizine subsurface damage, Shi [68] and colleagues conducted research on the subsurface microcracks in silicon wafers. They focused on the study of polarization laser scattering detection technology. The results in the polarization laser

scattering detection system were capable of detecting sub-surface cracks at low-density levels and micrometre-scale depths. When the depth of the sub-surface cracks was less than 3.25 µm, the signal was primarily determined by the density of the sub-surface cracks; whereas, when the depth exceeds 3.25 µm, the signal was predominantly determined by the depth of the sub-surface cracks (see Figure 2-6 d). Additionally, Niitsu et al. [69] utilized nanosecond pulsed Nd: YAG laser for laser repair of single-crystal silicon wafers to restore subsurface damage caused by grinding. Their experimental results indicated that the repaired silicon wafer surfaces did not exhibit grooves or pile-up.

In conclusion, many researchers have made significant contributions to the thinning of wafer backsides using lasers, particularly in improving surface quality and reducing surface damage. However, conventional laser thinning methods still face challenges with uneven material removal.

2.2 Diffractive Optical Element (DOE)

To address the issue of uneven material removal in traditional laser thinning methods, beam shaping has emerged as a novel and effective technique. Among the various beam shaping technologies, Diffractive Optical Element (DOE) have demonstrated particularly outstanding advantages. DOE not only allows precise control over the shape and distribution of the laser beam but also significantly enhances the uniformity of material removal and surface quality. DOE are a class of optical components that utilize the principles of diffraction to control the characteristics of light wavefronts. These elements modulate light waves by creating microscopic structures on their surfaces, such as periodic relief or etched patterns. They play an increasingly important role in optical systems, with applications spanning a wide range of fields, including optical sensing, optical communication, computational imaging, laser beam shaping, biomedical applications, and optical data storage. Key types of DOEs include (i) focusing DOE, (ii) polarization DOE, (iii) beam splitter DOE, (iv) holographic DOE, and (v) beam shaping DOE.

2.2.1 Focusing DOE

Focusing DOE utilizes the phenomenon of diffraction to achieve light focusing through the precise design of surface patterns. These elements feature periodic microstructures, such as etched patterns,

microlens arrays, or other optical designs. When light interacts with these finely engineered structures, different components of the light wavefront are diffracted at varying angles, resulting in a concentrated focal spot at a designated location. Current research is focused on optimizing the shape and distribution of the focused light spot to enhance the optical performance and efficacy of these elements in various applications.

Angelskar et al. [70] conducted an in-depth study on focusing DOE, analysing the performance of binary optical elements in separating and focusing specific infrared wavelengths through simulations and experiments. The study revealed the impact of Wood anomalies on the performance of DOE, particularly noting that both Rayleigh and resonance-type Wood anomalies were observed when the grating walls were smooth. Liu et al. [71] successfully designed and validated a novel diffraction optical element by introducing a half-π phase shift scheme. This element not only achieved multifunctionality by generating hollow beams and dual foci but also significantly reduced the interference issues between element arrays. Soria-Garcia [72] and their team innovatively defined the focal length angle distribution as a Fourier series, successfully designing a novel Fourier series diffraction lens. For a Fourier series diffraction lens with a focal length of 125 mm and a depth of focus of 25 mm, experimental results showed an average beam width of 59.7 µm, representing a reduction of 19.8% compared to lotus lenses and sectorized Fresnel lenses (see Figure 2-7).

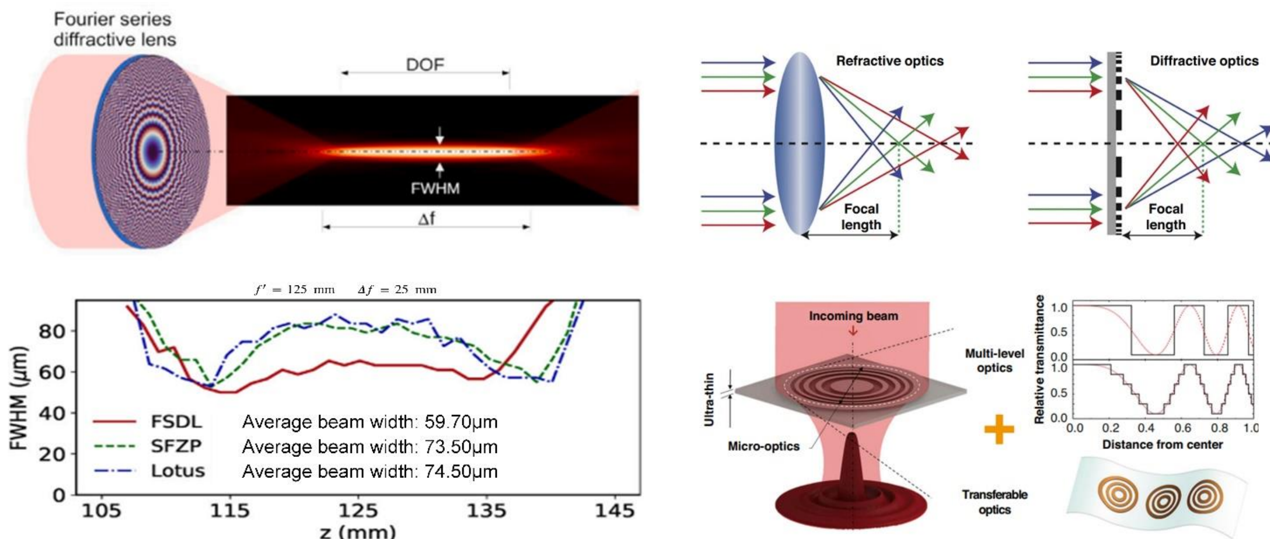

(Source: [72])

Figure 2-7 Research on focusing DOE

2.2.2 Polarization DOE

Polarization DOE manipulates and controls different polarization states of light through the precise design of their surface microstructures. The fundamental principle relies on the polarization characteristics of light, enabling these elements to selectively diffract or modulate light with various polarization directions. By doing so, Polarization DOE can effectively enhance or suppress specific polarization states, altering their propagation paths or polarization states and thereby creating predetermined optical patterns or spot distributions in space. Current research focuses on polarization conversion and multi-level polarization generation to advance the performance and functionality of these elements in practical applications.

Li et al. [73] designed and implemented a versatile polarization converter capable of executing 10,000 independent spatially encoded polarization scattering matrices. In experiments, the research team demonstrated the converter's efficiency and accuracy in handling spatially varying polarization fields through testing in the terahertz frequency range. Pavelyev et al. [74] demonstrated an innovative silicon-based subwavelength diffraction optical element capable of precisely generating terahertz coherent beams with preset polarization states. By accurately designing subwavelength micro-relief structures, these DOE produced radially polarized beams with polarization orders reaching the first, second, and third orders. In the research by P.S. Ramanujam et al. [75], polarization-sensitive holographic optical elements were successfully fabricated using polarization holography in azobenzene polyester materials. Experimental results revealed a diffraction efficiency of approximately 15% achieved with a single polarized laser beam. Tripathy et al.'s [76] study showcased a method for fabricating polarization-selective gratings on azopolymer films. By employing specific combinations of polarized beams for holographic writing, these grating elements exhibited varying diffraction efficiencies under orthogonal polarized readout beams. The lowest diffraction efficiency observed was 0.1% for vertically polarized beams, while the highest efficiency reached 6% for horizontally polarized beams. Nakata et al. [77] utilized circularly polarized continuous-wave lasers and interference patterns generated by DOE to fabricate helical structures on azopolymer films. At a laser power of 35.8 mW and an exposure time of 6 seconds, a regular triangular lattice structure with a period of 11.8 μm and a density of 8.29×10^5 cm^{-2} was formed (see Figure 2-8).

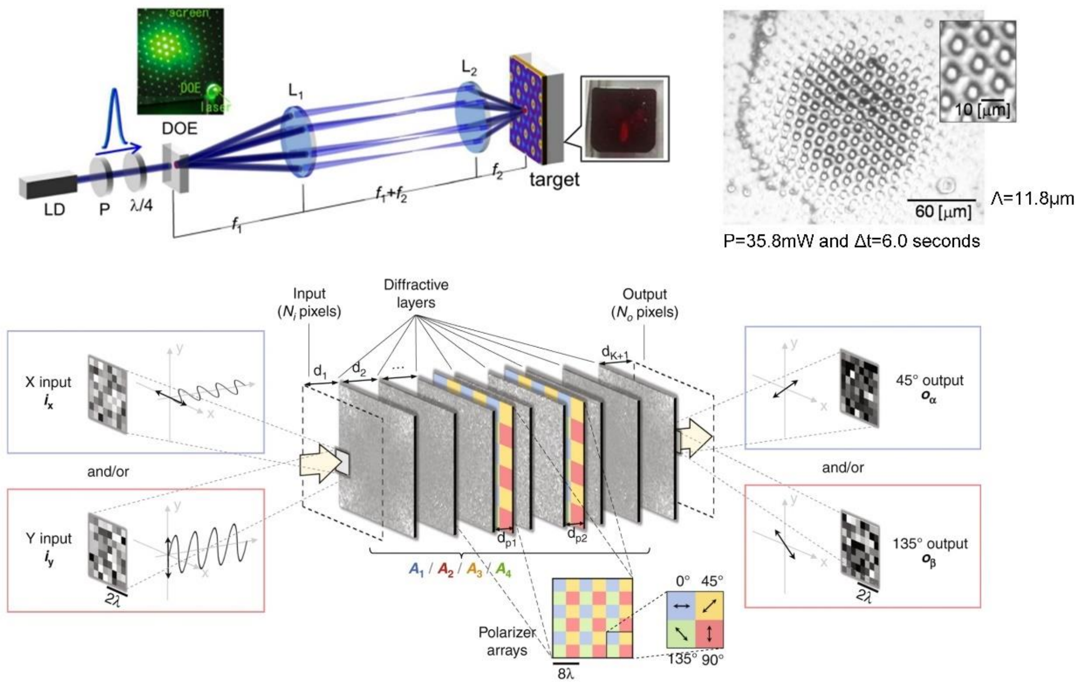

(Source: [77])

Figure 2-8 Research on polarization DOE

2.2.3 Beam splitter DOE

Beam splitter DOE utilizes the phenomenon of diffraction to divide an incident light beam into multiple paths with specific intensity ratios. These elements are engineered with periodic microstructures or patterns that diffract light in various directions. The underlying principle involves manipulating the phase and amplitude of light waves as they interact with the surface of the DOE to achieve beam separation. By precisely designing these microstructures, a Beam splitter DOE can attain the desired splitting ratios and output distributions, enabling efficient beam separation and routing for diverse optical applications. Current research focuses on enhancing the alignment accuracy and adjustable splitting angles of these elements to further improve their performance and broaden their application range.

J. Amako and E. Fujii [78] developed a non-digital diffraction beam splitter that achieved efficient and precise laser drilling on silicon wafers. In their experiments, the diffraction beam splitter attained an alignment accuracy of 5 μm across a 12 mm-wide beam array and successfully drilled 10,000 points in one minute, significantly enhancing production efficiency. This beam transmission approach was suitable for various laser applications requiring parallel processing, and by improving efficiency and accuracy, it significantly boosted overall productivity. Tomas Tamulevičius et al. [79]

explored a white light scattering technique for analysing and validating diffraction beam splitters. By precisely controlling the line heights of phase-shifting diffraction gratings (400–800 nm), the researchers achieved a diffraction efficiency exceeding 60% within the target wavelength range (405–633 nm). Wang et al. [80] proposed an innovative optical distortion measurement technique utilizing a phase diffraction beam splitter. Experimental results demonstrated that this method achieved a focal length measurement uncertainty of ±0.019% and a distortion measurement uncertainty of ±0.02% (see Figure 2-9). Wang [81] and colleagues proposed a tunable beam splitter using dual-layer geometric meta surfaces within the visible spectrum. By adjusting the relative displacement between the two layers, the splitter precisely tuned the splitting angle, with a range of up to ±60°. Wei et al. [82] introduced a novel side-absorbing concentration module that employs a diffraction grating as a spectral-beam splitter to divide sunlight into visible and infrared bands. Both simulation and experimental results demonstrated that the module achieved efficiencies of 45.2% and 34.8% across the entire solar spectrum, respectively.

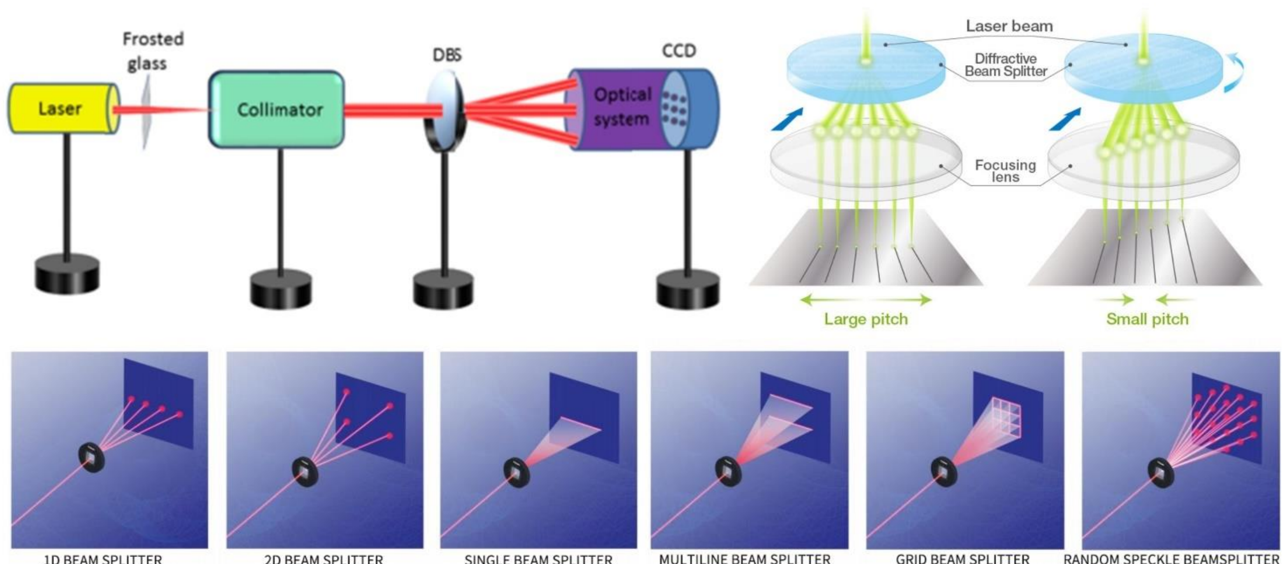

(Source: [80])

Figure 2-9 Research on beam splitter DOE

2.2.4 Holographic DOE

Holographic DOE leverages holographic technology to record the phase information of light waves, utilizing interference and diffraction principles to achieve complex optical functions. These elements are designed with precisely engineered microstructures within optical materials, allowing the incident light beam to be diffracted in a controlled manner, thereby producing predetermined beam

shapes and distributions. Holographic DOE enable accurate control over the propagation and wavefront characteristics of light. Current research focuses on optimizing holographic DOE for applications such as molecular orientation visualization, expanding the field of view in digital holography systems, and achieving efficient multi-wavelength energy coupling, aiming to enhance their performance and broaden their application potential.

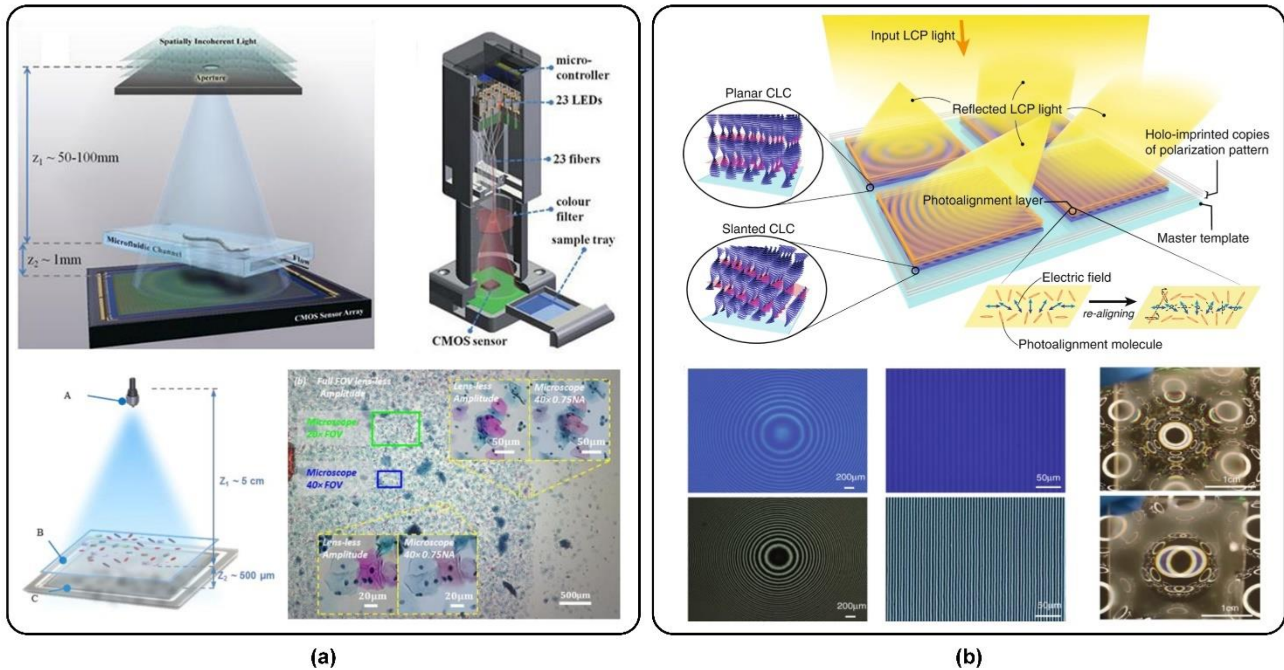

(Source: a [83], b [84])

Figure 2-10 Research on Holographic DOE. (a) A lens-free digital holographic microscopy technique based on DOE; (b) A holographic imprinting technique based on DOE

Wu et al. [83] introduced a lens-free digital holographic microscopy technique based on DOE. Experimental results indicated that this technique was able to synthesize pixel sizes much smaller than the wavelength of light at the digital level, achieving imaging of periodic structures with approximately 300 nm linewidth at a 530 nm illumination wavelength, which corresponds to an effective numerical aperture of about 0.9 (see Figure 2-10 a). Xiong et al. [84] introduced a holographic imprinting technique based on DOE. Experimental results indicated that, at a 457 nm laser wavelength, the efficiency of the high-angle reflection grating templates was approximately 97%, while the efficiency of the low-angle templates was approximately 99% (see Figure 2-10 b). Pensia et al. [85] developed a compact digital holography system based on multifunctional holographic optical elements, which improved resolution and field of view to record high-resolution digital holograms of larger objects. Experimental validation showed that the proposed system

achieved a 423% increase in the field of view compared to conventional digital holography systems. Ajay Kumar Singh et al. [86] designed and optimized holographic optical elements to achieve efficient energy coupling across different optical transmission windows. The research team achieved maximum diffraction efficiency at three key communication wavelengths (850 nm, 1310 nm, and 1550 nm). Experimental data indicated that the optimized holographic optical elements exhibited coupling efficiencies exceeding expectations, with the full width at half maximum (FWHM) range being broader than the anticipated operating wavelength range.

2.2.5 Beam shaping DOE

Beam shaping DOE employ diffraction principles to modify the spatial distribution and shape of an incident light beam. These elements achieve this by incorporating precisely engineered microstructures on their surfaces, which diffract the incoming light and redistribute its energy to transform the beam into a desired shape and intensity distribution. This process allows the conversion of an initial, non-uniform beam into specific patterns, such as a uniform flat-top beam or other specialized modes. Beam shaping DOE is widely applied in various optical tasks, including laser processing, optical imaging, and display systems, enabling precise control over beam characteristics. Current research focuses on optimizing beam shaping for laser beam shape conversion, the application of hybrid optical elements, customized beam shaping, focal plane intensity distribution, and multi-wavelength laser beam shaping, with the aim of further enhancing their performance and expanding their application range.

In Li et al.'s [88] study, a diffraction optical element with 16 phase levels was designed using the YG algorithm, successfully transforming a single-mode He-Ne laser beam into an annular intensity distribution. The experimentally measured diffraction efficiency reached 87.2%, differing from the theoretical value by only 3%. Qu et al. [89] innovatively combined DOE with different types of lenses to develop refractive/diffractive hybrid optical elements, effectively broadening the application range of beam shaping. Their research demonstrated that at a working distance of 800 mm, a convex lens could produce a ring-shaped diffraction pattern with a diameter of 124 mm, while a concave lens could generate a pattern with a diameter of 132 mm. Taghizadeh et al. [90] explored the potential of DOE in customizing laser beam shaping. By carefully designing DOE, traditional Gaussian beams or other laser modes can be converted into specific beam shapes tailored to different

processing requirements. This customized beam shaping enabled efficient use of laser energy, thereby improving processing quality and productivity. Tan et al. [91] proposed a novel design method that achieved the desired intensity distribution in the focal plane by adopting a new sampling interval. Experimental results showed that the DOE designed using this method achieved a uniform focused spot with an optical efficiency of 93.0% and a non-uniformity of 6.7%. For two symmetric uniform focused spots, the optical efficiency was 86.5%, with a non-uniformity of 10.6%. Han et al. [87] successfully used diffraction optical element to achieve precise shaping of multi-wavelength laser beams, generating high-quality rectangular spots. These spots enabled absolute size measurements of microparticles and real-time flow velocity detection. Experimental data showed that the measured flow velocity closely matched theoretical and simulated values, with an error of less than 5% (see Figure 2-11).

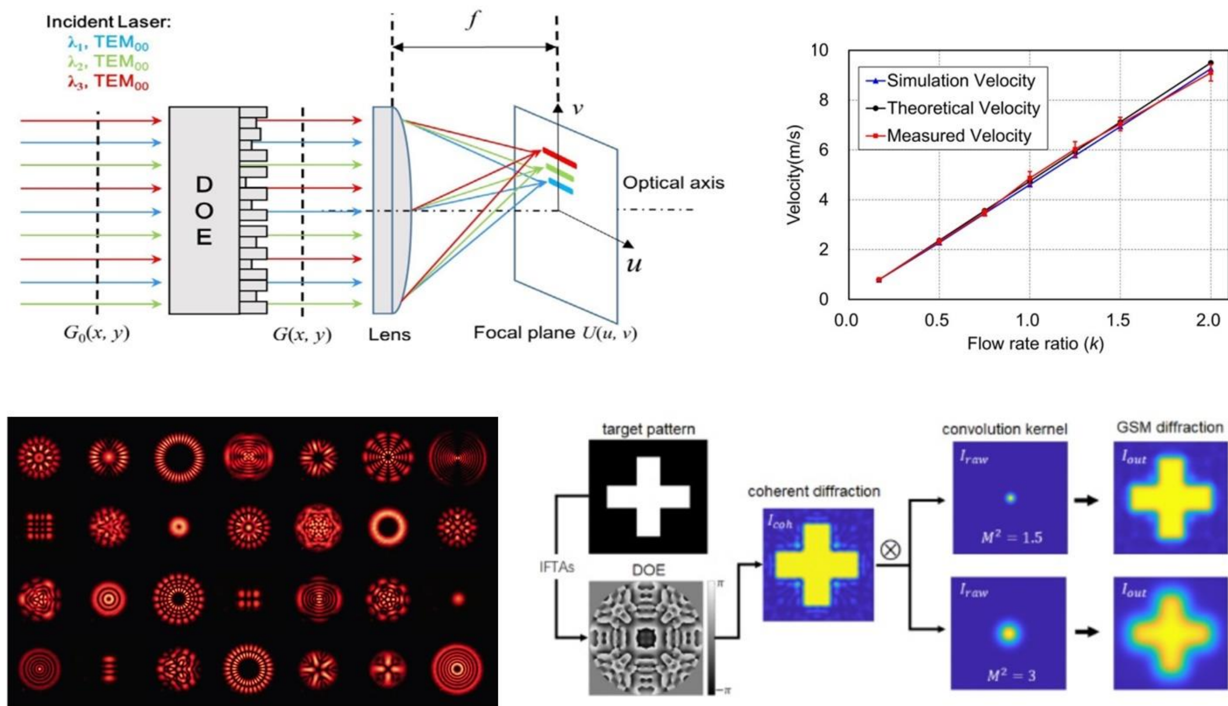

(Source: [87])

Figure 2-11 Research on Beam shaping DOE

2.3 Research Gaps

In the backside thinning process, each method has its own drawbacks. Mechanical Grinding (MG) causes surface damage and stress, leading to microcracks or defects, and achieving precise control over extremely thin thicknesses proves challenging. Chemical Mechanical Polishing (CMP) effectively

prevents surface damage; however, it is complex, costly, and carries potential environmental risks due to the use of liquid chemicals. Additionally, CMP results in uneven material removal, affecting surface quality. Electrochemical Mechanical Polishing (ECMP) enhances removal efficiency compared to CMP. However, it is highly sensitive to chemical environments and requires complex maintenance, leading to increased costs. Dry etching, while capable of high-precision thinning, has a slower removal rate, making it unsuitable for large surface areas, and increases surface roughness. Wet etching exhibits higher removal efficiency. However, it presents challenges in precisely controlling etch depth, leading to uneven removal, and involves substantial use of chemicals, complicating waste management. In laser thinning, traditional Gaussian beams offer high precision and speed; however, their non-uniform energy distribution results in uneven material removal, making it difficult to achieve the desired quality.

DOE-based beam can optimize energy distribution, resulting in a more uniform beam, reducing surface melting, and improving backside thinning effectiveness and surface flatness compared to GAU beam. However, research on the key characteristics of DOE remains insufficient, particularly regarding the impact of factors such as spot shape and energy distribution on their performance. Furthermore, the integration of DOE with other process equipment, especially with backside thinning systems, also lacks thorough investigation. The influence of various processing parameters, such as feed rate, frequency, and rotational speed, on DOE performance has not been systematically studied.

Chapter 3 Rotary laser thinning theoretical basis

3.1 Challenges in conventional linear & rotary laser thinning

Conventional laser thinning generally employ a galvanometer system to achieve precise control over the laser focus movement in the focal plane, facilitating line-by-line scanning and thinning of the silicon wafer surface [92] (see Figure 3-1 a). A typical approach involves a zigzag scanning pattern (see Figure 3-1 b). However, this method can lead to the following two issues with the processed surface (see Figure 3-1 c):

(i) Pits are commonly observed at the turning points of the zigzag scan path (see Figure 3-1 d). This phenomenon was because the deceleration of the galvanometer motor at the beginning and end of each trajectory, which resulted in multiple overlapping laser pulses ablated on a localized area, leading to overheating. Consequently, these turning points were deeper compared to those along the scanning paths, adversely affecting the quality of the processed surface.

(ii) Trenches became noticeable between adjacent scanning paths as a result of the Gaussian distribution of energy at the focal spots. The Gaussian profile caused the laser to remove material with a significant depth in the central region of each path, while the removal depth diminished towards the sides, thereby creating discernible trenches and impacting the overall machined surface quality (see Figure 3-1 e).

To address these issues, Shukla et al. [93] introduced an enhanced laser thinning method known as conventional rotary laser thinning. In this method, the silicon wafer was mounted on a uniformly rotating turntable, and the laser beam progressed linearly from the outer edge towards the centre of rotation (see Figure 3-1 f). This technique produced an arc-shaped thinning path, which effectively reduced pit formation associated with the pulsed trajectory's acceleration and deceleration (see Figure 3-1 g, h). Nonetheless, trenches between neighbouring scan paths persisted (see Figure 3-1 i). This phenomenon was because the Gaussian energy distribution, which resulted in non-uniform ablation pits, leading to a regular wavy drop-off on the wafer surface [94]. These defects not only compromised the smoothness and roughness necessary for high-precision manufacturing but also negatively impacted subsequent processing stages. Additionally, the redeposited material differs in

composition from the original wafer, potentially introducing impurities that could affect the electrical and optical properties of the final device.

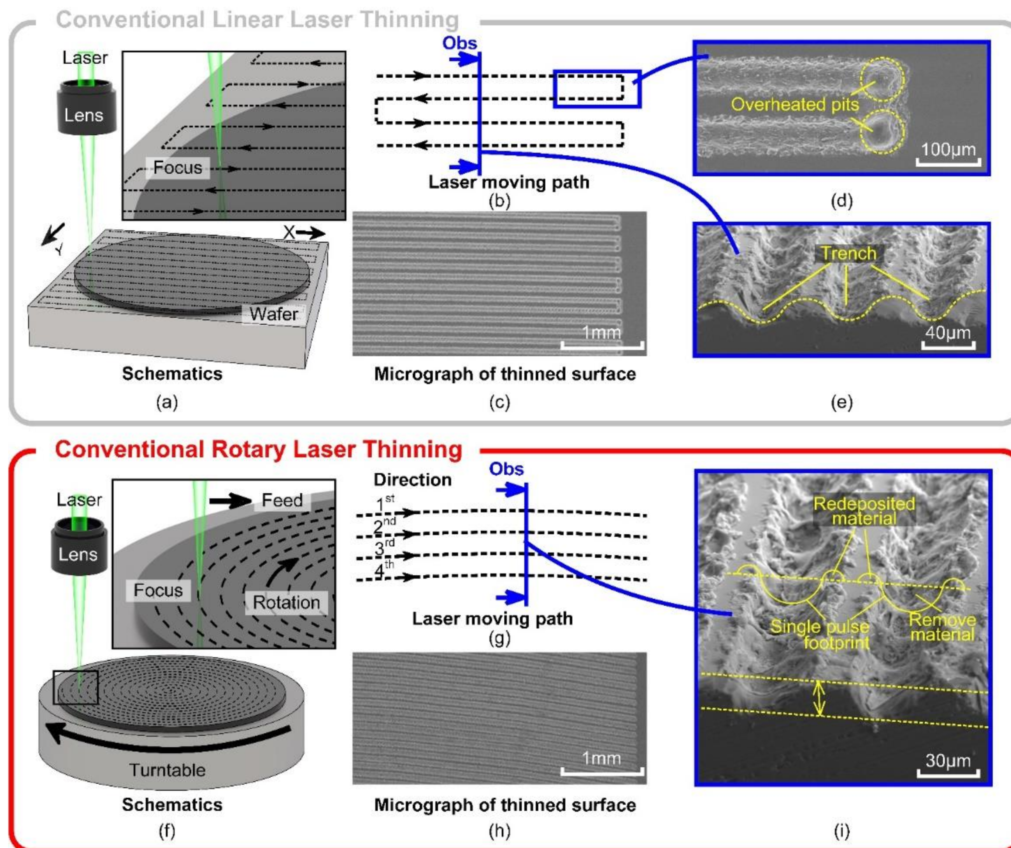

Figure 3-1 Conventional linear laser thinning (a) Schematic diagram of a wafer thinned using a galvanometer-moving laser spot; (b) Spot movement trajectory using a galvanometer-moving laser; (c) Visible trajectory topography of a galvanometer-thinned wafer using scanning electron microscope observation (SEM); (d) Overheated crater topography formed at an inflection point; (e) Highly protruding topography between neighbouring scanning paths; Conventional rotary laser thinning (f) Schematic diagram of a wafer thinned using a turntable; (g) Spot movement trajectory for rotary laser thinning; (h) Visible trajectory topography of a wafer thinned by rotary laser thinning using scanning electron microscopy (SEM); (i) Trenches still formed between neighbouring scanning paths

3.2 Rotary laser thinning based on diffractive optical elements

To overcome the previously discussed issues, a new laser thinning technique has been developed. The method utilized a linear spot created by a DOE, which was employed to diffract the laser beam, which was then focused onto the wafer surface using a focusing lens, resulting in an elongated laser spot. The wafer was mounted on a rotating platform that rotates at a constant angular velocity ω and simultaneously moved radially toward the centre of the platform at a constant linear velocity v. This combined movement ensured a uniform scan across the entire wafer surface (see Figure 3-2 a).

The width D of the laser spot remained unchanged compared to that of a Gaussian spot without the DOE. However, the length L of the spot was extended to 10 times its width D. As a result, for the same processing parameters and time duration, the linear spot covered a significantly larger area than a Gaussian spot, leading to a considerable improvement in thinning efficiency (see Figure 3-2 b).

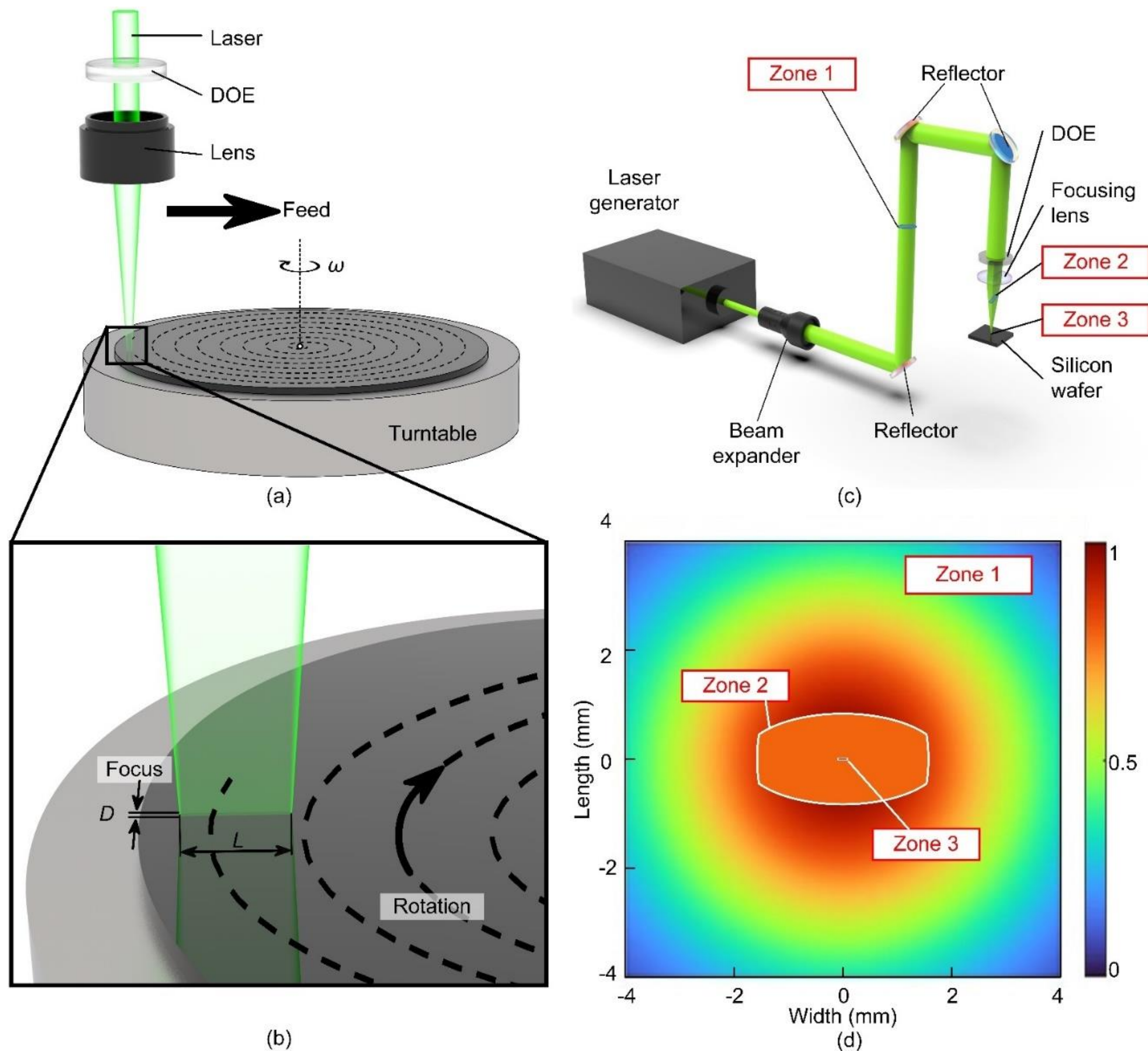

Figure 3-2 (a) Schematic diagram of DOE-based laser thinning; (b) Diagram of spot shape; (c) DOE-based laser thinning optical path diagram; (d) Spot size and beam energy distribution at different positions

The process began with the passing through a beam expander, which enlarged laser beam's diameter to 8 mm, thereby reducing beam divergence and producing a beam that closely approximates an ideal parallel beam (see Figure 3-2 c). At this point, zone 1 depicted the energy distribution with a concentration in the centre and a gradual decrease towards the edges. The beam was then redirected perpendicular to the thinning plane by three mirrors before it reached the DOE and focusing lens. As the beam converges, zone 2 represented the energy distribution after it had passed

through the DOE, showing a transition from a circular to a linear spot shape with a uniform energy distribution. Ultimately, when the beam was focused onto the wafer surface, it formed a linear spot, with its energy distribution illustrated in zone 3 (see Figure 3-2 d).

3.3 DOE design

To meet the requirements for laser spot shape and energy distribution, a diffractive optical element (DOE) is developed to generate linear spots (see Figure 3-3 a). This DOE features a diffraction grating, which is meticulously engineered by etching precise microstructures onto its surface (see Figure 3-3 b). The purpose of these microstructures is to impart specific phase shifts to the incident light. As the light interacts with the DOE, varying optical path lengths are introduced at different spatial locations within the beam, leading to distinct phase delays.

These phase delays result in interference effects as the modulated beam propagates. The interference pattern alters the spatial distribution of energy within the beam. Once this beam passes through a focusing lens, it transforms into a uniform linear spot at the target plane (see Figure 3-3 c).

The DOE employs a sawtooth-shaped grating structure, consisting of an array of flat and sawtooth-like grooves etched onto its surface (see Figure 3-3 d). The interaction of light with these jagged grooves produces a series of diffracted beams. The characteristics of these diffracted beams—such as their intensity and direction—are influenced by two key factors: (i) the angle of the bevelled surface and (ii) the spacing of the grooves.

(i) The spacing of the grooves is particularly crucial in determining the diffraction angle of the beams. This relationship is governed by the grating equation (see Eq. 1), which describes how the groove spacing affects the angle at which the light is diffracted. By carefully designing these parameters, the DOE ensures that the laser beam is modulated to produce the desired linear spot shape with accurate energy distribution.

$$d \sin\theta = n\lambda \tag{1}$$

where d is the distance between adjacent engraved lines, θ is the diffraction angle. $\lambda = 532$ nm is the wavelength of the light wave, and $n = 1$ is the diffraction order. In this study, a 532 nm

wavelength green laser source is selected for thinning silicon wafers because the 532 nm wavelength exhibits optimal absorption characteristics in silicon material, providing better energy conversion efficiency. Compared to the 1064 nm (near-infrared laser), it has a higher silicon absorption rate, which improves processing efficiency. Additionally, the shorter 532 nm wavelength offers higher spatial resolution than the 1064 nm wavelength, allowing for finer processing and better control over the spot size and focusing accuracy during the thinning of silicon wafers. Furthermore, the 532 nm wavelength, in comparison to the 255 nm (ultraviolet laser), helps avoid excessive thermal effects, reducing thermal damage and ensuring the quality of the silicon wafer surface during processing. Therefore, the 532 nm wavelength not only meets the system's high-resolution requirements but also optimizes the efficiency and stability of the optical system while minimizing thermal damage. Moreover, selecting an appropriate diffraction order is crucial for system performance. In this study, the first-order diffraction (1st order) is chosen because it carries a larger proportion of the light energy, resulting in higher light intensity, which enhances the system's efficiency. Higher diffraction orders disperse the light energy across multiple orders, weakening the intensity of each, which negatively impacts the system's output power. Additionally, higher diffraction orders increase the diffraction angle, causing the light beam to diverge, which affects the focusing ability and overall performance of the system By carefully designing the groove spacing and profile, both the diffraction angles and intensities of the resulting beams can be precisely controlled, directing the diffracted light to constructively interfere and form the desired linear beam profile with a uniform energy distribution (see Figure 3-3 e). The diffraction angle θ can be calculated by Eq. (2)

$$\theta = \tan^{-1}\frac{r-a}{2f} = \tan^{-1}\frac{8-0.02}{2\times 75} = 0.673^{\circ} \tag{2}$$

where $r = 8$ mm is the diameter of the incident light, $a = 20$ µm is the width of the spot target shape, and $f = 75$ mm is the focal length of the focusing mirror. In this study, an 8 mm incident light diameter is selected to optimize the performance of the optical system. A larger incident light diameter helps reduce the divergence angle of the beam, resulting in a smaller spot size, which improves focusing accuracy and system resolution. If a smaller incident light diameter were chosen, although the resolution could be improved, the beam might become excessively divergent, affecting the focusing performance and potentially leading to a decrease in light intensity, which would reduce

energy transmission efficiency. On the other hand, while choosing a larger incident light diameter would further control the beam divergence, an excessively large spot size could negatively impact the focusing ability and precision of the system. The 8 mm incident light diameter strikes a balance between these factors, ensuring a smaller spot size and higher resolution, while avoiding excessive light intensity reduction and maintaining the energy transmission efficiency of the system, thus optimizing overall performance to meet the requirements for high-precision processing.

(ii) The groove angle is a critical parameter in managing the angular distribution of the diffracted light, which significantly affects the shape and uniformity of the resultant beam profile. When light encounters the inclined facets of the grooves within the DOE, it undergoes refraction, as described by Snell's Law [101]. Snell's Law provides a relationship between the angles of incidence and refraction, depending on the refractive indices of the media on either side of the groove. In the context of our DOE design, Snell's Law is formulated as Eq. (3)

$$m\sin\beta = \sin\left(\theta + \beta\right) \tag{3}$$

where $m = 1.76$ is the refractive index of sapphire, and β is the inclination angle of the inclined surface of the diffraction grating groove. Therefore, the inclination angle of the inclined surface of the diffraction grating groove β can be calculated by Eq. (4)

$$\beta = \tan^{-1}\frac{\frac{n\lambda}{d}}{m - \sqrt{1 - \left(\frac{n\lambda}{d}\right)^2}} \approx 0.42^{\circ} \tag{4}$$

The angle of the diffraction grating directly influences the diffraction angle of the light beam. As the grating angle increases, the diffraction angle also increases. Selecting an appropriate grating angle is crucial for effectively controlling the diffraction angle, thereby optimizing the beam's propagation path and ensuring it travels in the correct direction. If the grating angle is too large, the diffraction angle will increase, potentially causing the beam to deviate from its intended path, which can adversely affect the system's focusing performance. A properly chosen grating angle ensures that the diffracted beam maintains a small divergence angle, which is essential for high-precision beam focusing. If the diffraction angle is too large, the beam's divergence will degrade the focusing precision, negatively impacting imaging quality and processing accuracy. Furthermore, the

relationship between the grating angle and the diffraction angle also determines the energy transmission efficiency. If the grating angle is too large, the beam's divergence may lead to energy loss. Therefore, by appropriately adjusting the grating angle, it is possible to maintain system focusing while maximizing the transmission efficiency of energy.

This relationship demonstrates that when multiple gratings interact collectively, they produce a composite diffraction pattern due to the specific diffraction characteristics of each individual grating. By meticulously adjusting the shape and spacing of the microscopic gratings on the DOE, it is possible to precisely control both the intensity and direction of the diffracted light, thereby achieving the desired linear light output. The result is a linear spot that exhibits a uniform energy distribution along its length and a Gaussian distribution across its width (see Figure 3-3 f). This spot configuration ensures uniform energy density in the feed direction and, when combined with rotational laser thinning, effectively removes the trenches between adjacent machining paths. Consequently, this results in a flatter surface with reduced roughness.

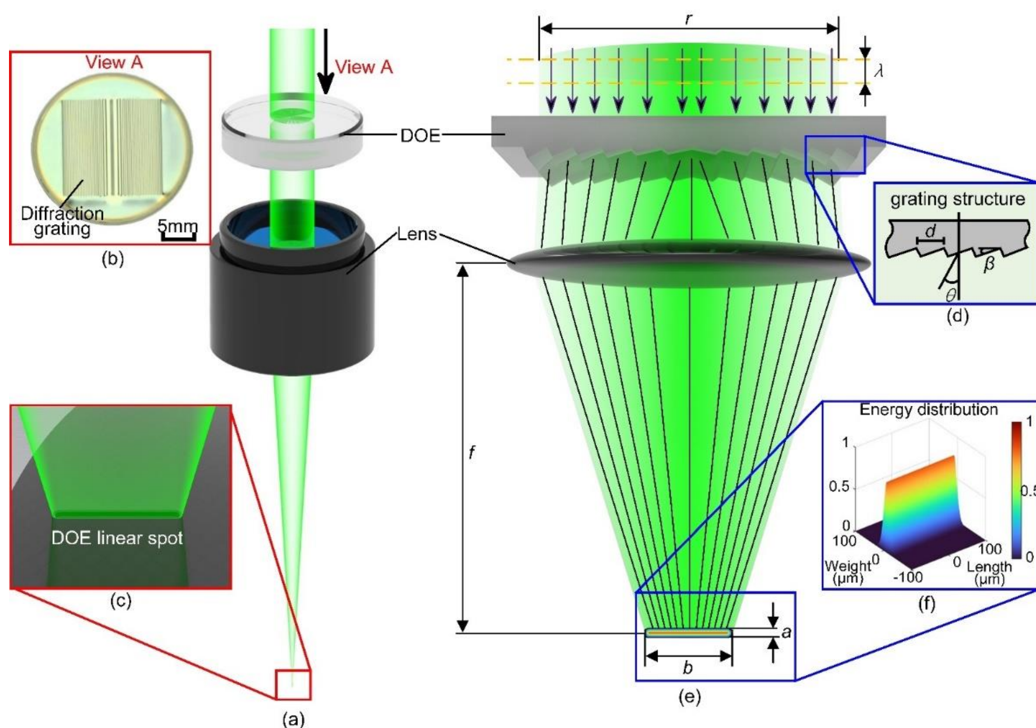

Figure 3-3 (a) Physical figure of DOE; (b) Shape of DOE under orthogonally polarized light; (c) Shape of the focused spot after the laser passes through the DOE; (d) Schematic of the microstructure of the grating on the surface of the DOE; (e) Diffraction schematic diagram of the laser passing through the DOE; (f) Energy distribution of the focused spot

3.4 Summary

This chapter begins by summarizing two inherent drawbacks of conventional laser thinning methods: pit formation at scan path turning points and trench formation between adjacent scan lines due to the Gaussian energy distribution of the laser beam. The proposed DOE-based rotary laser thinning technique addresses these two issues:

1. Conventional linear laser thinning employs galvanometer-controlled scanning, requiring rapid changes in direction at turning points. This leads to increased laser dwell time at these locations, causing localized overheating and subsequent pit formation. The rotary laser thinning method utilizes a continuously rotating platform, enabling the laser spot to move smoothly along an arc. This eliminates abrupt directional changes and the associated dwell time, effectively mitigating pit formation and promoting more uniform energy delivery.
2. Conventional laser thinning techniques often suffer from non-uniform material removal due to the inherent Gaussian energy distribution of the laser beam. This results in deeper ablation at the beam's center and shallower ablation at its edges, leading to the formation of trenches between adjacent scan lines and an uneven surface finish. To address this limitation, this study employs a specifically designed DOE to transform the Gaussian beam into a linear spot with a uniform energy distribution along its length. This engineered beam profile ensures consistent material removal across the entire spot width, minimizing depth variations and promoting a smoother, more uniform surface compared to conventional methods.

To achieve the desired linear spot shape and control its energy distribution, a DOE with specific parameters was designed and fabricated. This DOE utilizes a sawtooth grating structure. The grating period was calculated based on the grating equation and the target line spot width to precisely control the diffraction angle. The grating blaze angle was determined using Snell's Law to manage the angular distribution of the diffracted light, ensuring uniform energy distribution across the linear spot. Consequently, the DOE transforms the incident Gaussian beam into a linear spot with uniform energy distribution along its length and a Gaussian distribution across its width. This unique energy profile, coupled with the rotational scanning strategy, provides the foundation for highly efficient and high-quality silicon wafer thinning.

Chapter 4 Rotary laser thinning experimental results and discussion

4.1 Experiment platform

A five-axis laser thinning platform incorporating diffractive optical element (DOE) technology was developed (see Figure 4-1 a, b). The system expanded the laser beam using a beam expander, which then directed the beam through a series of three reflective mirrors before it reaches the DOE and focusing lens assembly. The machine tool's X-axis supported the Z-axis, allowing for both horizontal and vertical movement of the focusing lens. Additionally, the Y-axis was equipped with A and B axes, enabling forward/backward translation and rotational adjustment of the workpiece. This configuration provided the necessary degrees of freedom and precise control, making it possible to effectively harness the line-shaped beam produced by the DOE for high-quality and efficient laser thinning processes.

To perform laser experiments in an atmospheric environment using this platform, a standard single-sided thinned sample with dimensions of 10 × 10 × 0.6 mm was selected. The sample was irradiated with a picosecond YAG laser system, operating at a wavelength of 532 nm and a pulse width of 50 ps. The number of laser pulses applied to the sample was controlled by a pulse generator connected to a computer.

The experimental setup positioned the focal point of the laser beam directly on the material surface. This approach was preferred over positive defocus, where the focal point was situated above the surface, as positive defocus could lead to a decrease in energy density. Such a reduction in energy density resulted in thinning depth and potentially increased surface roughness due to the dispersion of energy. Similarly, negative defocus, where the focal point was located below the surface, was also avoided. Although negative defocus temporarily increased energy density, it reduced thinning efficiency and enlarged the heat-affected zone, which could lead to material deformation and the formation of micro-cracks. By maintaining the focal point precisely on the material surface, the setup optimized energy density and processing efficacy, thereby ensuring efficient and high-quality material removal (see Figure 4-1 c).

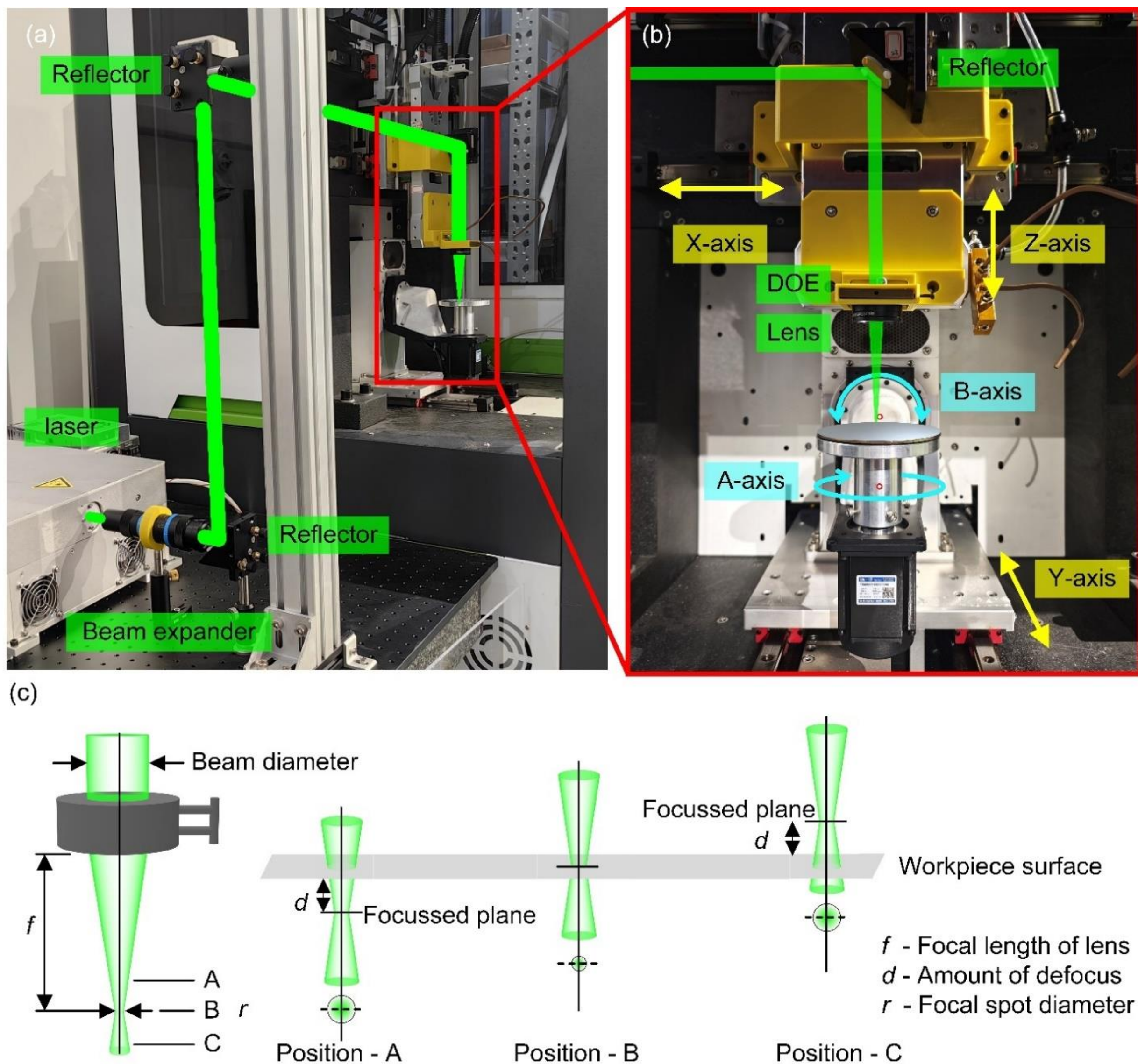

Figure 4-1 (a) Laser thinning platform; (b) Platform details and laser head; (c) Effect of laser focus and defocus

In this study, a range of advanced analytical instruments was employed to thoroughly investigate the effects of the laser thinning process. A scanning electron microscope (SEM, EVO 18, ZEISS, Germany) was used to observe the surface morphology of the samples, allowing for the identification of microstructural changes induced by the laser treatment. This was complemented by an energy dispersive spectrometer (EDS, EVO 18, ZEISS, Germany), which provided detailed information on the elemental composition of the samples. The crystal structure, phase changes, and structural stability of the samples were analysed using an X-ray diffractometer (XRD, D8 Advance, Bruker Corp., Germany). Additionally, an ultra-depth-of-field microscope (Model VHX-6000, Keyence Corp., Japan) offered high-resolution, three-dimensional surface imaging, facilitating a detailed examination of surface features such as roughness and defects. The wettability of the samples was evaluated using

a contact angle meter, assessing the impact of laser treatment on surface hydrophilicity. Atomic force microscopy (AFM, FastScan Bio, Bruker Dimension, Germany) was employed to acquire nanoscale information on surface morphology, precisely measure surface roughness, and observe microstructural changes. The integration of these diverse analytical techniques provided a comprehensive assessment of the laser thinning process, delivering extensive and nuanced data to support the study's conclusions.

4.2 Flat surface thinning with DOE-based laser compared to GAU laser

This chapter provides a comparative analysis of thinned flat surfaces processed using both a DOE-based and a GAU laser beam. The comparison is structured across four aspects: (i) machined surface morphology (Section 4.2.1), (ii) surface roughness (Section 4.2.2), (iii) material behaviours, including Amortization and oxidation (Section 4.2.3), and (iv) surface wettability (Section 4.2.4). Additionally, Section 4.2.5 discusses the ablation mechanisms associated with DOE-based processing in contrast to those of the GAU laser beam.

4.2.1 Machined surface morphology

The flat surfaces thinned using the GAU laser beam displayed distinct grooves with bowl-shaped cross-sectional profiles, where each groove had a central region that was deeper than the edges. This resulted in a pronounced wave-like surface pattern, characterized by a regular arrangement of peaks and valleys. This pattern was consistently observed across different processing parameters (see Figure 4-2 a, c, e, and g). This effect was attributed to the Gaussian intensity profile of the GAU laser beam and the resultant overlap of the ablation pits. The central region of the beam, which had the highest energy intensity, caused the deepest ablation, forming the lowest part of each groove. As the beam’s energy intensity decreased towards the edges, the depth of ablation also diminished, leading to the bevelled edges characteristic of Gaussian profiles. The overlapping of successive grooves during scanning created a uniform, wave-like surface pattern.

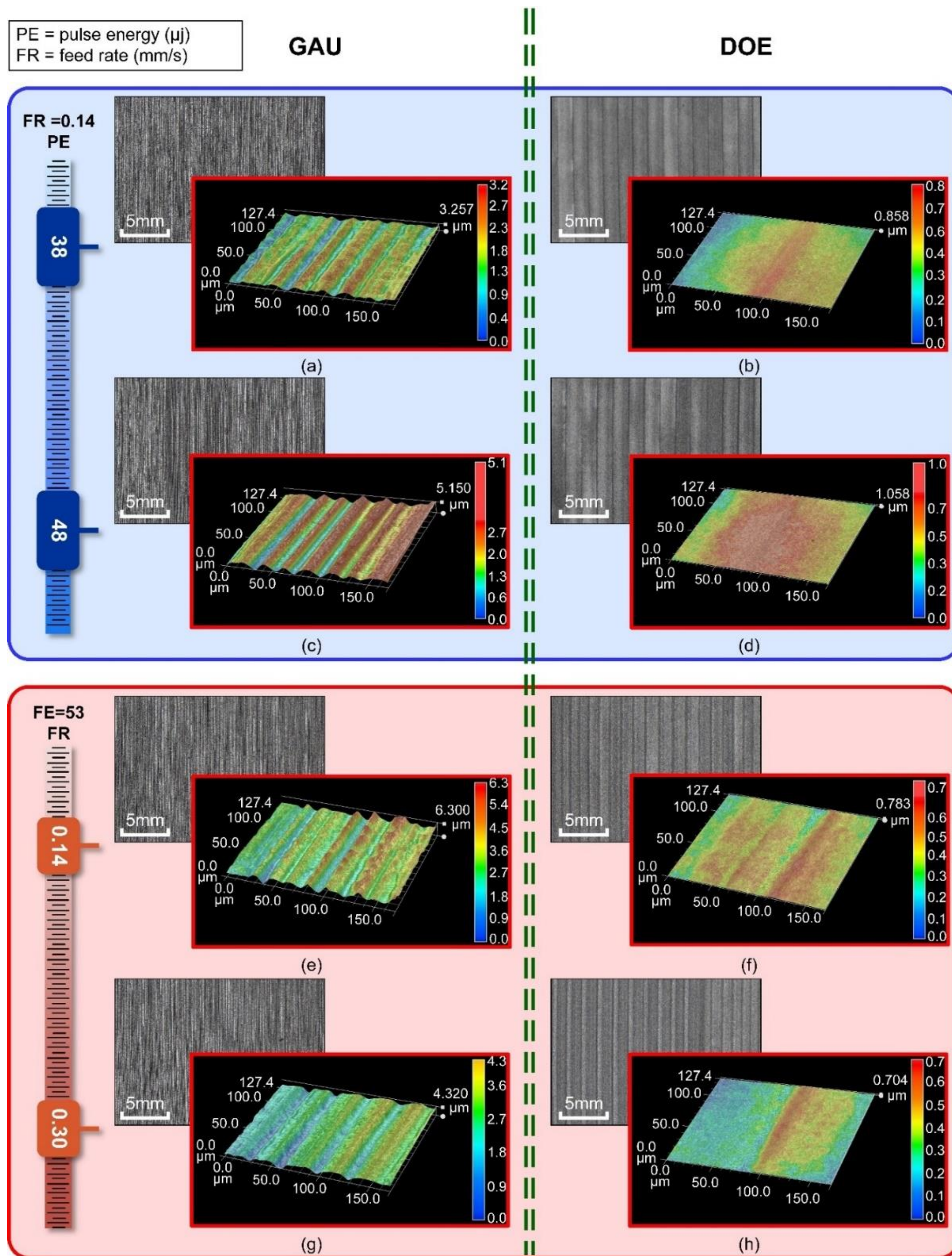

Figure 4-2 When the pulse energy is 38 μJ and the feed rate is 0.14mm/s, (a) The surface morphology of the wafer is treated by GAU laser beam; (b) Surface morphology of DOE-based laser beam treated silicon wafer; When the pulse energy was 48 μJ and the feed rate was 0.14 mm/s, (c) GAU laser beam treated the wafer surface morphology; (d) Surface morphology of DOE-based laser beam treated silicon wafer; When the pulse energy was 58 μJ and the feed rate was 0.14 mm/s; (e) GAU laser beam treated wafer surface morphology; (f) Surface morphology of DOE-based laser beam treated silicon wafer; When the pulse energy is 58 μJ and the feed rate is 0.30mm/s; (g) GAU laser beam is used to treat the wafer surface morphology; (h) Surface morphology of DOE-based laser beam treated silicon wafer

In contrast, the grooves produced using the DOE exhibited a flat-bottomed profile with a consistent ablation depth throughout each groove. This uniformity in ablation depth was maintained regardless

of the varying processing parameters (see Figure 4-2 b, d, f, and h). The flat-bottomed grooves resulted from the even energy distribution of the DOE-based linear laser spot, which ensured that material ablation was consistent across the entire groove without the formation of peaks or valleys. The uniform energy distribution of the DOE-based beam minimized the effects of overlapping channels, resulting in accurate and consistent material removal. Furthermore, this even distribution reduced the risk of collateral damage, facilitated cleaner ablation, and decreased the need for post-processing.

4.2.2 Surface roughness

In the semiconductor industry, there is a stringent requirement for high yield rates of products, making even minor variations in surface roughness significantly impactful on device performance. The maximum surface roughness (Rz) is chosen for evaluation due to its heightened sensitivity to fluctuations in surface peaks and valleys, which provides a more accurate reflection of the surface microstructure requirements for semiconductor products compared to other roughness parameters. Consequently, Rz is utilized as the primary metric for assessing surface quality.

The Rz values achieved with the DOE-based beam consistently exhibited lower surface roughness compared to those obtained with the GAU beam across varying laser parameters. This difference could be observed from three perspectives:

(i) As single-pulse energy increased, the DOE-based beam resulted in a significantly smaller increase in machined surface roughness compared to the GAU beam. At an energy of 34 μJ, the surface roughness difference between the two methods was approximately 50 nm. However, at a single-pulse energy of 58 μJ, this difference expanded to around 450 nm (see Figure 4-3 a). This discrepancy was attributed to the varying sputtering effects of redeposited material during processing. The DOE-based beam, with its uniform energy distribution, effectively minimized localized high-energy hotspots, thereby reducing non-uniform material removal and redeposition (see Figure 4-3 b). In contrast, the GAU beam’s concentrated energy peaks resulted in high energy densities that caused rapid vaporization and ejection of material, leading to deeper craters and increased surface roughness (see Figure 4-3 c).

(ii) The DOE-based beam exhibited a significantly smaller reduction in surface roughness with increasing thinning passes compared to the GAU beam. Initially, after a single pass, the surface roughness difference between the two methods was approximately 120 nm. However, after 50 thinning passes, this difference decreased to about 50 nm (see Figure 4-3 d). This could be attributed to the DOE-based beam's uniform energy distribution, which minimizes the formation of deep craters and allows for smoother surface evolution with each pass. The absence of pronounced peaks and valleys in the DOE-based beam's energy profile facilitated a consistent and gradual material removal process (see Figure 4-3 e). Conversely, the deep craters and sharp features generated by the GAU beam necessitate multiple passes for effective ablation and smoothing (see Figure 4-2 f).

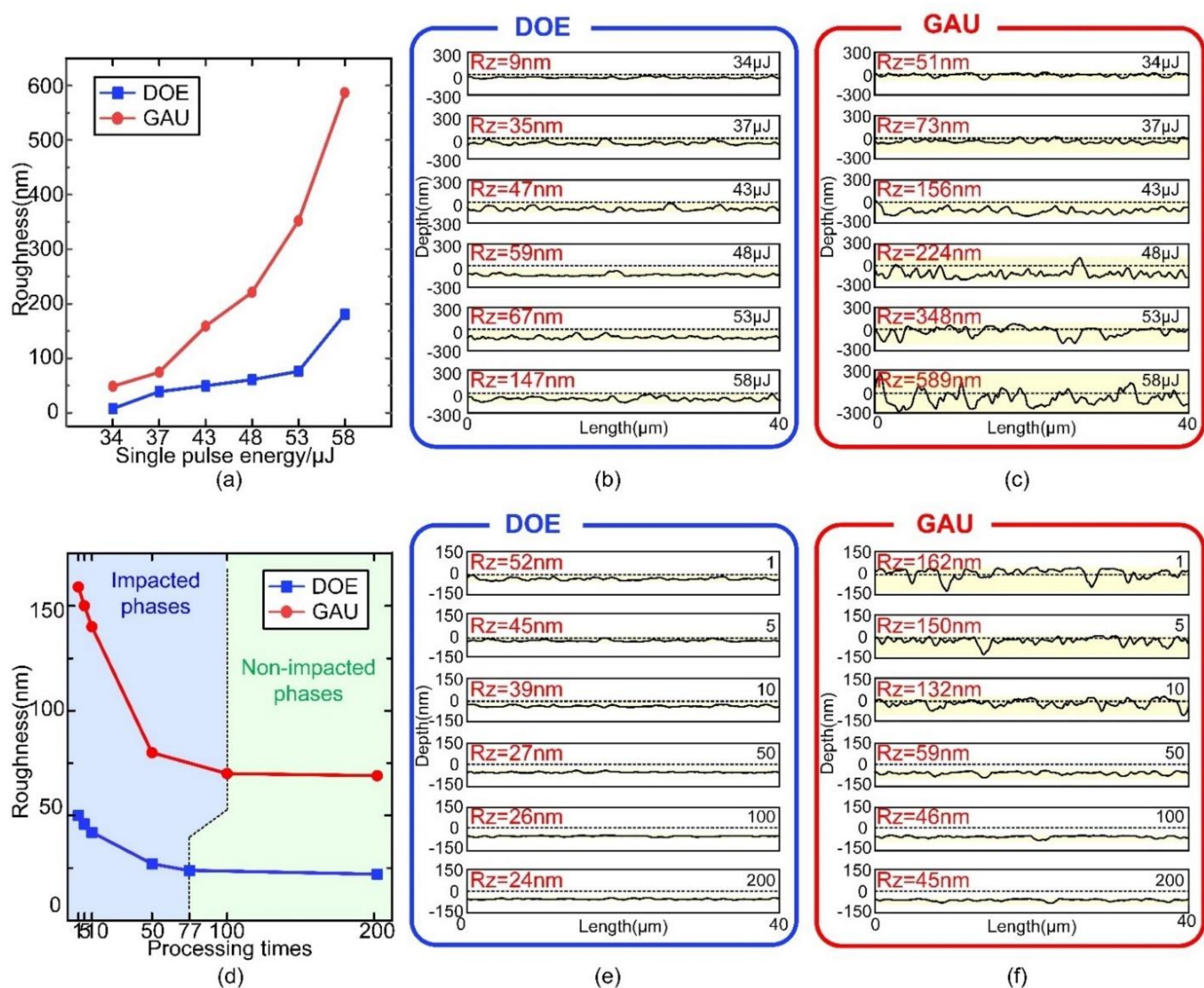

Figure 4-3 (a) Effect of different single pulse energies on roughness; (b) Surface morphology of silicon wafer thinned by DOE-based laser beam under different single pulse energies; (c) Surface morphology of silicon wafers thinned by GAU laser beam under different single pulse energies; (d) Effect of different thinning times on roughness; (e) Morphologies of silicon wafers thinned by DOE-based laser beam under different thinning thorns; (f) Morphology of silicon wafers thinned by GAU laser beam under different thinning spines

(iii) The variation in surface roughness could be divided into two phases: the impacted phase and

the non-impacted phase. During the impacted phase, surface roughness decreased with an increasing number of thinning passes for both DOE-based and GAU-based beams. However, in the non-impacted phase, surface roughness remained constant despite increases in the number of passes. The DOE-based beam transitioned into the non-impacted phase after 77 thinning passes, whereas the GAU beam required 100 passes to reach this phase (see Figure 4-3 d). This indicated that the DOE-based beam achieved a stable surface quality more rapidly than the GAU beam.

In conclusion, these observations underscored the superior performance of the DOE-based beam in achieving lower surface roughness and more efficient material removal compared to the GAU beam, attributable to its uniform energy distribution and reduced tendency for surface irregularities.

4.2.3 Material behaviours (Amortization and oxidation)

The formation of amorphous silicon and silicon dioxide (SiO_2) during the laser thinning process had a substantial impact on the electrical and thermal conductivity of the wafer, affecting both the physical properties of the material and subsequent processing and applications. The XRD analysis of the initial single-crystal silicon surface revealed a sharp, intense diffraction peak at 28.4° (see Figure 4-4 a, Initial Surface). In contrast, the diffraction peak for the thinned single-crystal silicon surface was broad and of low intensity, indicating a significantly reduced degree of crystallinity, measured at 0.68% (see Figure 4-4 a, 34 μJ).

The DOE-based laser beam thinning process effectively mitigated the formation of amorphous silicon. Although the surface crystallinity achieved with the DOE laser beam was initially lower than that of the GAU laser beam after a single thinning pass at a pulse energy of 34 μJ, the DOE beam demonstrated superior surface crystallinity as both the single-pulse energy and the number of thinning passes increased. The difference in crystallinity reached a maximum of 60.34% at 43 μJ and 29.38% at 100 thinning passes, respectively (see Figure 4-4 b). This improvement was attributed to the DOE-based beam’s uniform energy distribution, which ensures even ablation across the entire surface. Once the recrystallization threshold for single-crystal silicon was reached, this even distribution contributes to a stable crystallinity. Conversely, the GAU beam, with its non-uniform energy distribution, primarily reached the ablation threshold at the central region while generating a substantial amount of amorphous silicon at the edges.

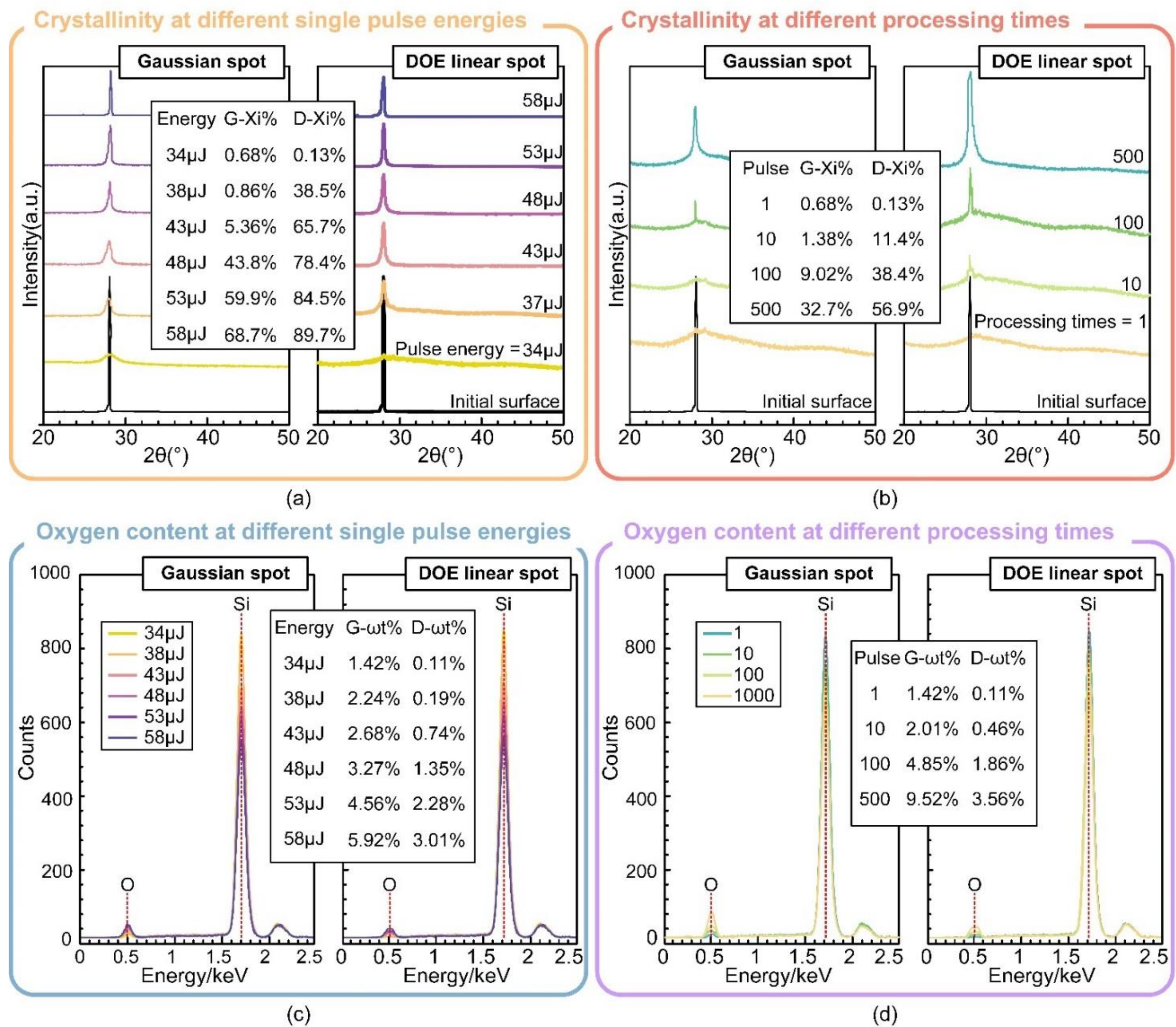

Figure 4-4 Comparison of crystallinity between Gaussian spot and DOE-based linear spot; (a) Different single pulse energy; (b) Different thinning times; Comparison of oxygen content between Gaussian spot and DOE-based linear spot; (c) Different single pulse energy; (d) Different thinning times

In addition, DOE laser thinning reduced the formation of SiO_2. The elemental oxygen percentage on surfaces treated with the DOE laser beam was consistently lower than that on surfaces treated with the GAU laser beam, regardless of single pulse energy and the number of thinning passes. The disparity in elemental oxygen mass percentage increased with higher single-pulse energies and a greater number of thinning passes. For instance, at a single pulse energy of 58 μJ, the crystallinity of the DOE-treated surface was 3.01%, compared to 5.92% for the GAU-treated surface, reflecting a difference of 2.91%. At 500 thinning cycles, the crystallinity of the DOE-treated surface was 3.56%, whereas the GAU-treated surface had a crystallinity of 9.52%, resulting in a difference of 5.96% (see Figure 4-4 c, d). This phenomenon could be explained by the DOE-based beam's uniform energy

distribution, which prevents localized overheating and minimizes oxidation reactions. In contrast, the GAU laser beam's high central energy density made it prone to localized oxidation.

In conclusion, DOE-based laser thinning significantly enhanced crystallinity and effectively reduced oxidation, thereby preserving the desirable electrical, mechanical, and chemical properties of single-crystal silicon.

4.2.4 Surface wettability

The hydrophilicity of the thinned surface was crucial for subsequent processing steps in silicon wafer fabrication. For instance, in Backside Wet Etching, a hydrophilic surface enhances the interaction between the etching solution and the wafer, thereby improving etching efficiency. To assess wettability, the water droplet contact angle was measured for surfaces thinned using both the DOE-based and GAU laser beams. A contact angle greater than 90° indicates hydrophobicity, whereas an angle less than 90° denotes hydrophilicity.

Surfaces thinned with the DOE-based laser beam demonstrated isotropic hydrophilicity, exhibiting consistent wettability in both radial and tangential directions. Specifically, the contact angle on DOE-thinned surfaces decreased from 93.04° to 77.82° in the tangential direction and from 86.84° to 75.71° in the radial direction as the single-pulse energy increased. In contrast, the GAU beam-thinned surfaces displayed anisotropic hydrophilicity. In the radial feed direction, the contact angle decreased from 96.21° to 88.68° with increasing energy, indicating increased hydrophilicity. Conversely, in the tangential feed direction, the contact angle increased from 97.51° to 104.51°, signifying enhanced hydrophobicity (see Figure 4-5 a).

This disparity could be attributed to the surface texture characteristics induced by each laser beam. The DOE-based laser thinning process resulted in surfaces with minimal and uniform texture, closely matching the path morphology (see Figure 4-5 b). This uniform texture led to consistent water droplet spreading in all directions. Conversely, the GAU laser beam produced surfaces with a distinctive striated texture along the tangential feed direction (see Figure 4-5 c). These striations, characterized by certain heights, impeded the spreading of water droplets in the tangential direction. As single-pulse energy increased, the height of these striations grew, further restricting water

droplet diffusion.

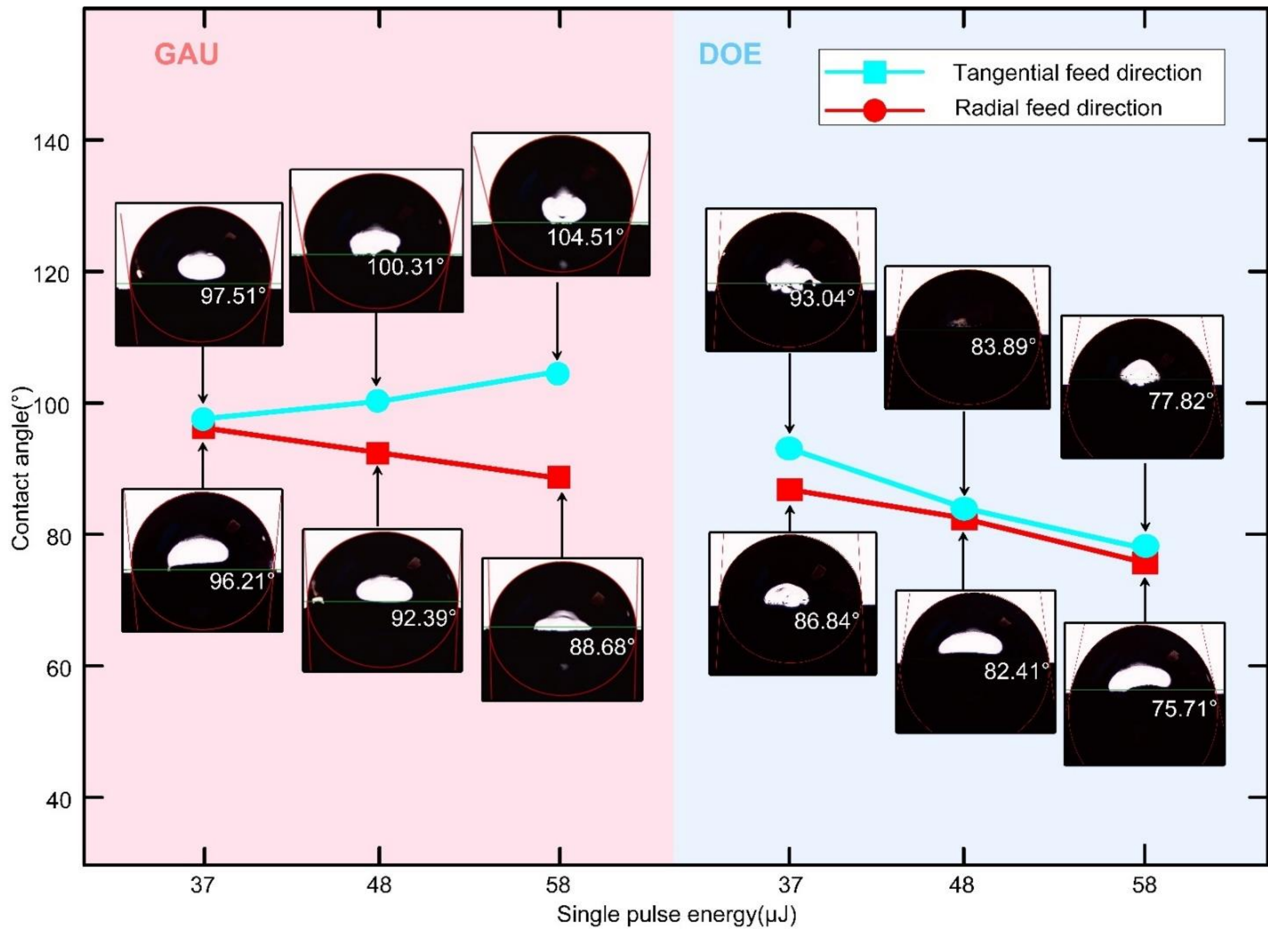

(a)

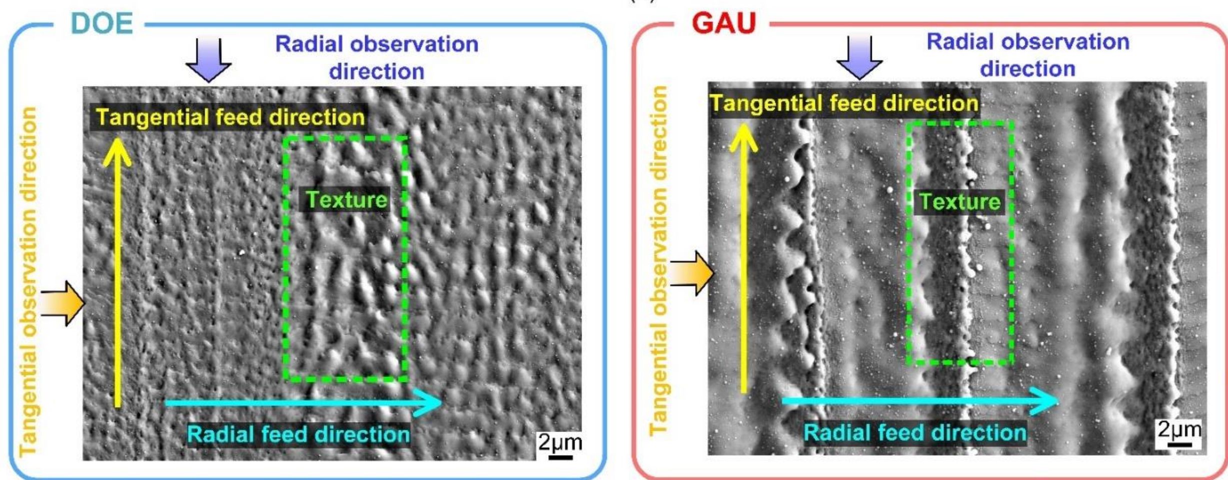

(b) (c)

Figure 4-5 (a) Contact angles of DOE-based and GAU beam-machined surfaces at different monopoles energies; (b) SEM image of surface texture processed by GAU beam; (c) SEM image of surface texture processed by DOE-based beam

The study highlights the advantages of DOE-based laser thinning over the GAU laser method in achieving optimal surface wettability for silicon wafer processing. DOE-based technology yields isotropic and hydrophilic surfaces, with uniform contact angles regardless of orientation. This

uniformity is particularly advantageous for processes such as backside wet etching, where consistent wetting ensures uniform interaction between the etchant and the silicon surface. This leads to consistent etch rates across the wafer, which is critical for precise dimensional control and reduced product variation. In contrast, the anisotropic hydrophilicity observed with GAU laser-thinned surfaces, due to their pronounced striated texture, impedes uniform wetting and introduces directional dependency, making it less suitable for processes requiring consistent wettability.

4.2.5 Different DOE-based ablation mechanisms compared with GAU laser beam

In the context of the discussed phenomena, the DOE-based laser thinning technology offers a significant advantage over the GAU laser approach in achieving optimal surface wettability in silicon wafer processing. To further elucidate the differences in ablation mechanisms between DOE-based and GAU lasers, a detailed examination was conducted.

When using a DOE-based linear beam on a rotating platform, the energy was distributed uniformly along a linear path. This even distribution of energy resulted in relatively lower thermal effects, favouring material melting rather than vaporization. Consequently, the material tended to form micro spherical ablation pits on the surface (see Figure 4-6 a). As the platform rotated and the laser scanned laterally, these ablation pits accumulated in the laser's feed direction, creating a surface with an irregular texture characterized by noticeable bumps and undulations (see Figure 4-6 b). In the radial direction of the laser, the DOE's uniform energy distribution ensured that adjacent sections of ablation tracks exhibit only relatively smooth projections (see Figure 4-6 c).

Conversely, when thinning was performed with a GAU beam on a rotating platform, the energy was concentrated at a single point. This concentration resulted in a sharp localized temperature rise and pronounced thermal effects, leading to significant melting or even vaporization of the material. This process created ablation pits with a deep central region and shallower edges, with molten material frequently extending beyond the pit's boundaries (see Figure 4-6 d). As the platform rotated and the laser scanned laterally, these ablation pits align along the laser's cutting direction, forming a texture reminiscent of fish scales (see Figure 4-6 e). In the radial direction, adjacent sections of the ablation tracks were positioned at the edges of the Gaussian pit, resulting in shallow ablation depths and forming ridge-like projections (see Figure 4-6 f).

This phenomenon was due to the unique energy distribution properties of DOE-based beams. Compared with GAU beam, which concentrated higher energy in the centre and lower energy at the edges, the DOE-based linear spot distributed energy more uniformly across its entire length. This uniform distribution resulted in a lower energy density at any given point compared to the peak energy density of a GAU beam with equivalent total energy. To quantitatively analyse the relationship between the pulse energy densities of these two beam types, a comparison of the peak energy densities of the two spots was made. The peak energy density of the DOE-based beam could be calculated using Eq. (5)

$$I_D = \frac{\mu E}{lw} \tag{5}$$

where I_D is the DOE-based peak single pulse energy density. μ is the energy transmission coefficient of DOE, which is determined by the transmittance of the material. For sapphire, μ is 98%. E is the single pulse energy, l is the length of the DOE-based beam at the intersection point, and w is the width of the DOE-based beam at the intersection point. The peak energy density of the GAU can be calculated from Eq. (6)

$$I_G = \frac{2E}{\pi r^2} \tag{6}$$

where I_G is the GAU peak single pulse energy density, r is the radius of the Gaussian beam at the focal point.

Table 4-1 DOE-based and GAU Peak Energy Density Calculations

Laser beam	Length (μm)	Width (μm)	Radius (μm)	Energy transmission coefficient (%)	Peak energy density (J/m^2)
DOE-based	200	20	N/A	98	2.45×10^8E
GAU	N/A	N/A	7.9	N/A	1×10^{10}E

From Table 4-1, the peak energy density of both beams at the focal point can be calculated. Comparing the peak energy densities of the two beams at the focal point, it can be found that the energy ratio of the DOE-based beam to the GAU beam is calculated by Eq. (7)

$$\frac{I_D}{I_G} = \frac{1}{40} \tag{7}$$

Based on this analysis, it can be clearly found that the peak single pulse energy density I_D of the DOE-based linear spot is approximately $\frac{1}{40}$ of the Gaussian spot I_G.

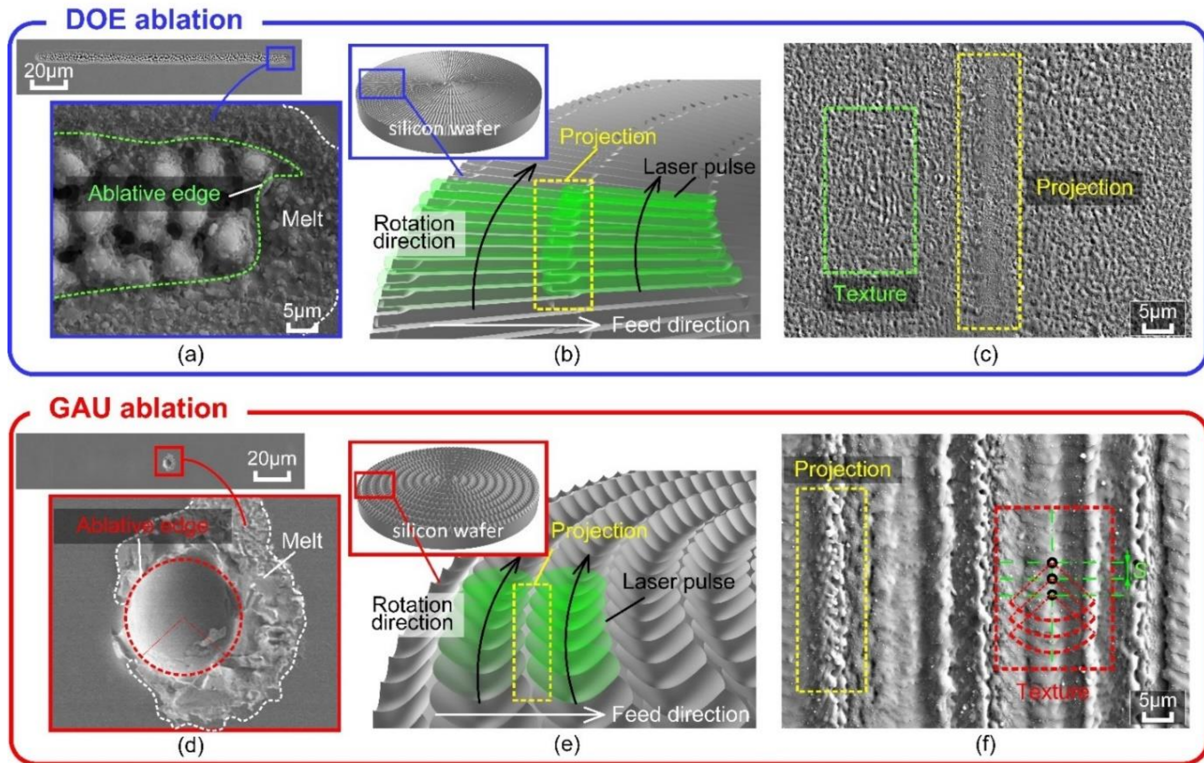

Figure 4-6 (a) Single hole ablation morphology of DOE-based beam machining; (b) DOE-based laser thinning diagram; (c) Planar morphology of DOE-based beam ablation; (d) Single hole ablation morphology of GAU beam machining; (e) GAU laser thinning diagram; (f) Planar morphology of GAU beam ablation

4.3 Non-flat surface thinning with DOE-based laser compared to GAU laser

In addition to processing flat surfaces, wafer surfaces exhibit defects such as scratches and cracks resulting from impacts during transport. Laser thinning is employed to address these imperfections. However, this process presents challenges due to the regenerative effect. Specifically, laser thinning of a surface with pre-existing scratches or cracks can exacerbate these defects. The thinning process not only reduces the top surface but also further thins the bottom of the scratches or cracks, thereby widening them. Consequently, surface defects persist even after achieving the desired thinning thickness, leading to increased scrap rates and reduced processing efficiency. To evaluate and compare the performance of different laser thinning methods, wafers with ten grooves of gradually

increasing depth were subjected to thinning using both the DOE-based laser beam and the Gaussian laser beam within the same timeframe (see Figure 4-7 a).

The DOE-based laser beam demonstrated a significant reduction in the regenerative effect. The depth of regeneration observed with the DOE-based beam was 1.31 μm, compared to 2.22 μm with the GAU beam, representing a 41% reduction in depth. In terms of groove width, the DOE-based beam increased the groove width from 3.23 μm to 3.62 μm, whereas the GAU beam expanded the groove width from 3.36 μm to 4.3 μm. This indicated a 59% reduction in the regeneration effect with the DOE-based beam in terms of width (see Figure 4-7 c). The reduced regeneration effect with the DOE-based beam could be attributed to its avoidance of the high peak energy concentration typical of the central region of the Gaussian beam. Additionally, the DOE-based beam's smaller depth of focus range compared to the GAU beam mitigated excessive removal at the edges of the grooves.

Beyond reducing the regeneration effect, the DOE-based beam also enhanced thinning efficiency and processing accuracy. The DOE-based beam achieved a thinning depth of 5.01 μm within the same timeframe that the GAU beam reached 3.91 μm (see Figure 4-7 c). Notably, the DOE-based method could complete ten thinning passes on the workpiece surface in the same amount of time required for a single pass with the GAU method (see Figure 4-7 b). This demonstrated that the DOE-based approach not only achieves greater thinning depth but also delivers superior accuracy and efficiency in the machining process.

This phenomenon was because the uniform linear distribution of the DOE beam and the optimized spot shape that allowed the laser energy to be distributed evenly over the workpiece surface during each thinning operation. This uniform distribution avoided the problem of large energy differences between the centre and edges of the spot with conventional GAU beams, resulting in thinner thinning depths and a significant reduction in surface roughness with the DOE beam. The spot length of the DOE beam was 10 times longer than that of the GAU beam, which resulted in the DOE beam taking 1/10th of the time required by the GAU beam to thin the same area of a wafer. Therefore, in the same amount of time it took the GAU beam to thin the surface once, the DOE beam could thin the surface 10 times, thus improving the final processed surface quality.

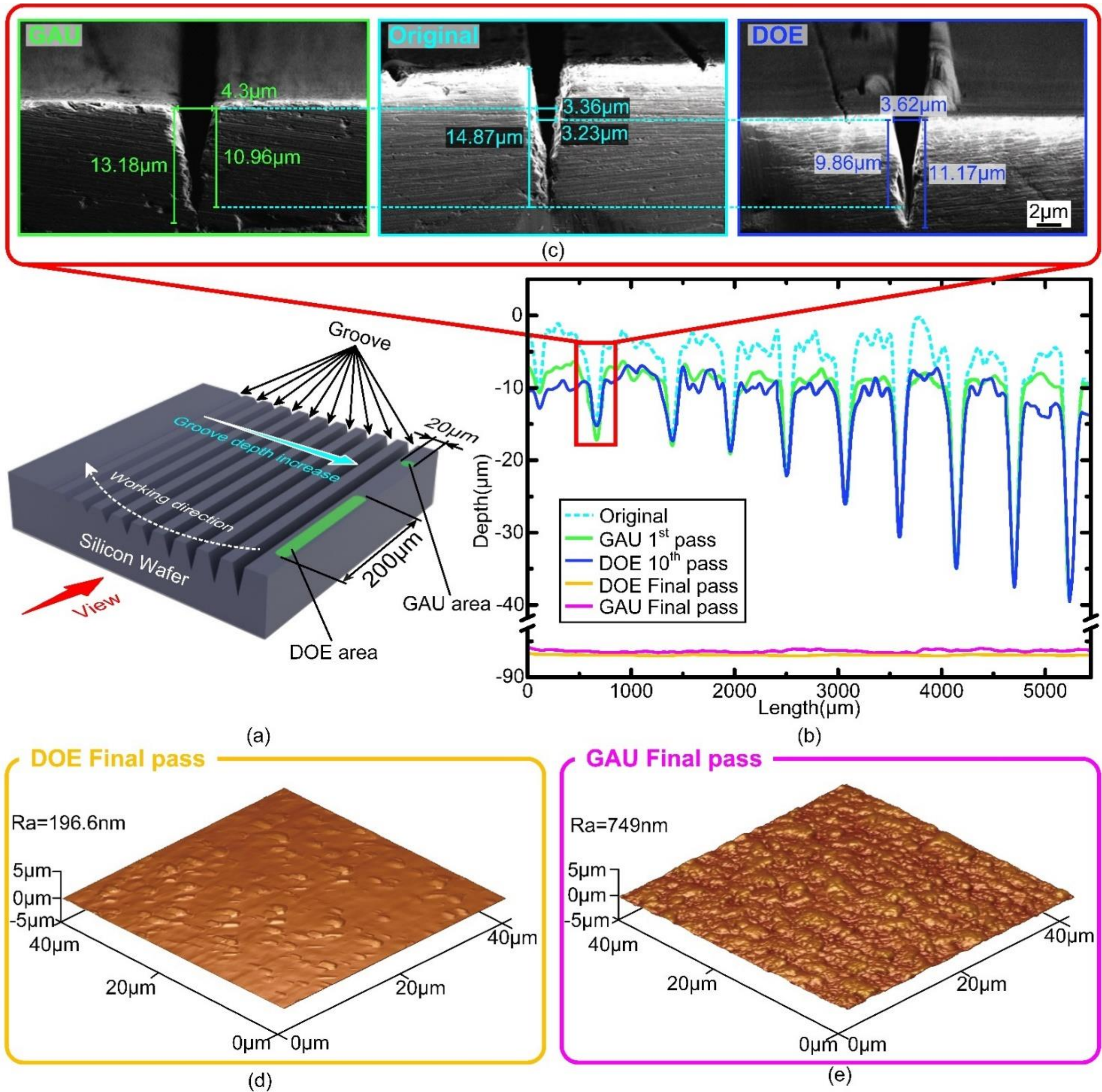

Figure 4-7 (a) Groove experiment and laser principle; (b) Depth curve of groove; (c) SEM image of groove; (d) AFM image of DOE-based laser thinning final pass; (e) AFM image of GAU laser thinning final pass

The surface thinned with the DOE-based beam is significantly flatter than that thinned with the GAU beam over the same duration. The DOE-based method achieved a notably low Rz of 198.6 nm, resulting in a smooth and uniform topography (see Figure 4-7 d). In contrast, the GAU method produced an Rz of 749 nm, indicating a relatively rougher surface with distinct peaks and valleys (see Figure 4-7 e).

4.4 Effects of process parameters in DOE-based laser thinning process

To elucidate the influence of key parameters in the laser thinning process, a series of experiments

were designed and conducted, focusing on the effects of (i) pulse frequency and (ii) rotational speed on machining efficiency and surface quality. The experiments employed single-crystal silicon specimens with dimensions of 10× 10 × 1 mm. By maintaining constant average laser power and radial feed rate, while precisely modulating pulse frequency and rotation speed, the impact of varied thinning conditions on material removal and surface morphology was observed.

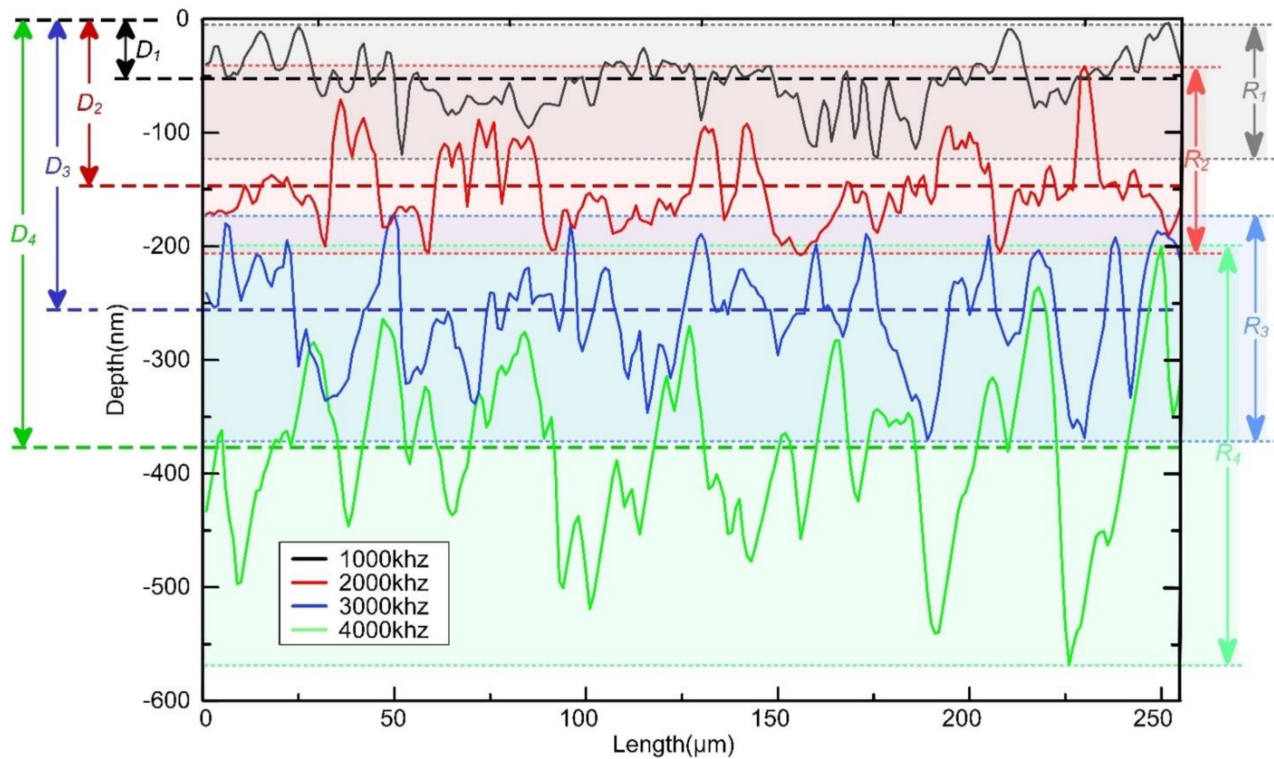

Figure 4-8 Surface depth and surface roughness curves of a wafer at different laser frequencies

(i) As the pulse frequency (1000 kHz to 4000 kHz) increased, the surface roughness and depth increased. This trend was further confirmed by the reference lines R1 - R4, representing the maximum depth difference, and D1 - D4, representing the average machining depth. At 4000 kHz, the surface roughness was maximum and the depth of cut was deepest (see Fig. 4-8). This was due to the fact that although each pulse had the same energy, the cumulative energy deposited on the material increased with frequency. High energy deposition resulted in a high ablation rate, meaning that much material was removed per pulse. The fast the pulse repetition frequency, the short time the material had to cool between pulses. This heat build-up led to localized melting and uneven material removal, further increasing surface roughness.

(ii) As the rotational speed decreased from 229 rpm to 57 rpm, the depth of ablation increased while the surface roughness decreased. Specifically, low speeds, such as 57 rpm, produced smooth

surfaces and significant depths, whereas high speeds, such as 229 rpm, resulted in irregular surfaces and reduced depths (see Fig. 4-9). This phenomenon was because the high spot overlap at low rotational speeds, which resulted in low surface roughness and deep ablation, thereby improving material removal efficiency.

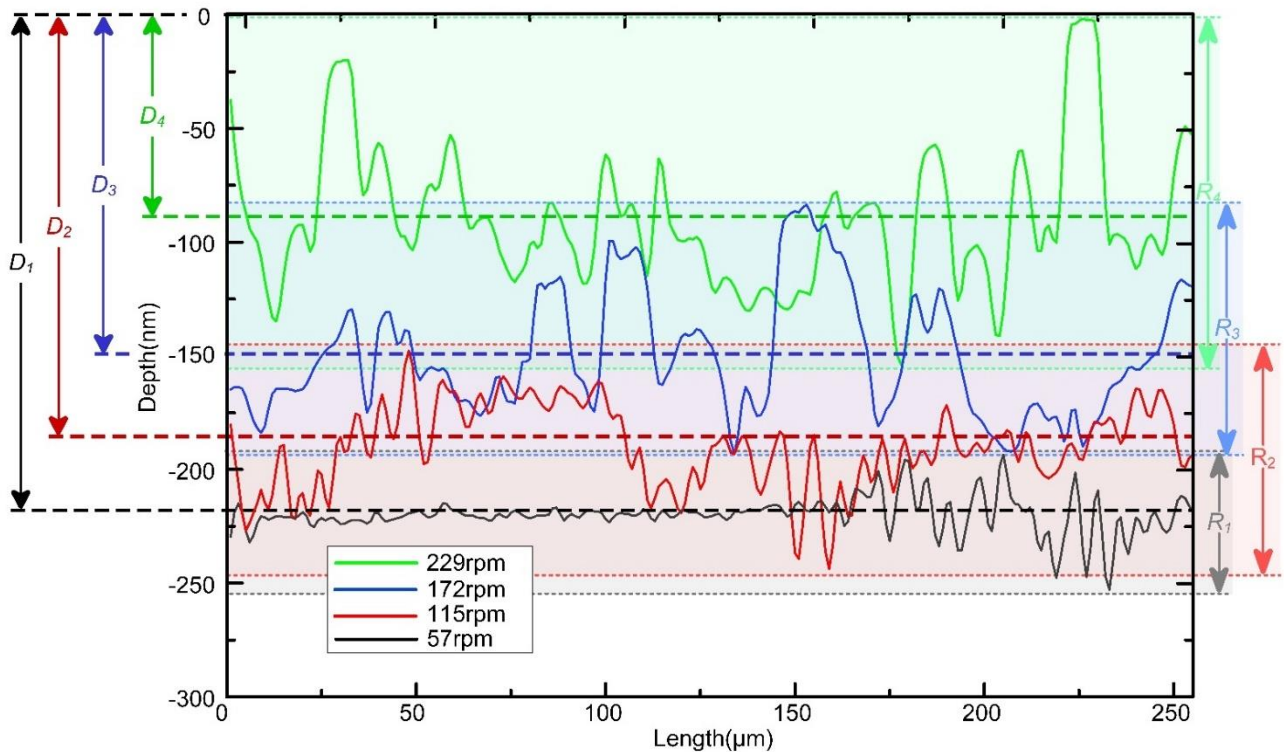

Figure 4-9 Surface depth and surface roughness curves of a wafer at rotational speed

A comparative analysis of the trends in the average depth of cut and maximum surface roughness (Rz) at different pulse frequencies and rotational speeds was conducted (see Fig. 4-10). Both the average depth of cut and Rz increased with rising pulse frequency. This relationship indicated that an increase in frequency led to greater material removal and enhanced surface refinement. Conversely, an increase in rotational speed resulted in a decrease in the mean depth of cut, while Rz exhibited an increase. This suggested that rapid movement resulted in irregular surface features. These findings indicated that low rotational speeds produced smooth surfaces with large average depths, whereas high pulse frequencies achieved pronounced surface modifications.

The interplay between pulse frequency and rotational speed was crucial for optimizing surface characteristics during laser thinning. Practical applications required a balanced selection of these parameters to achieve an ideal compromise between surface roughness and cutting depth, ensuring both high surface quality and efficient thinning. Analysis of the three graphs (see Fig. 4-8 - 4-10)

revealed that these parameters profoundly impacted surface quality, highlighting the complexity of laser surface refinement. Effective optimization was essential for tailoring surface properties to meet specific application needs, whether prioritizing smoothness, depth, or a combination. These findings underscored the importance of precise control over processing parameters in advanced manufacturing, providing insights that enhanced laser manufacturing processes and improved material performance and functionality.

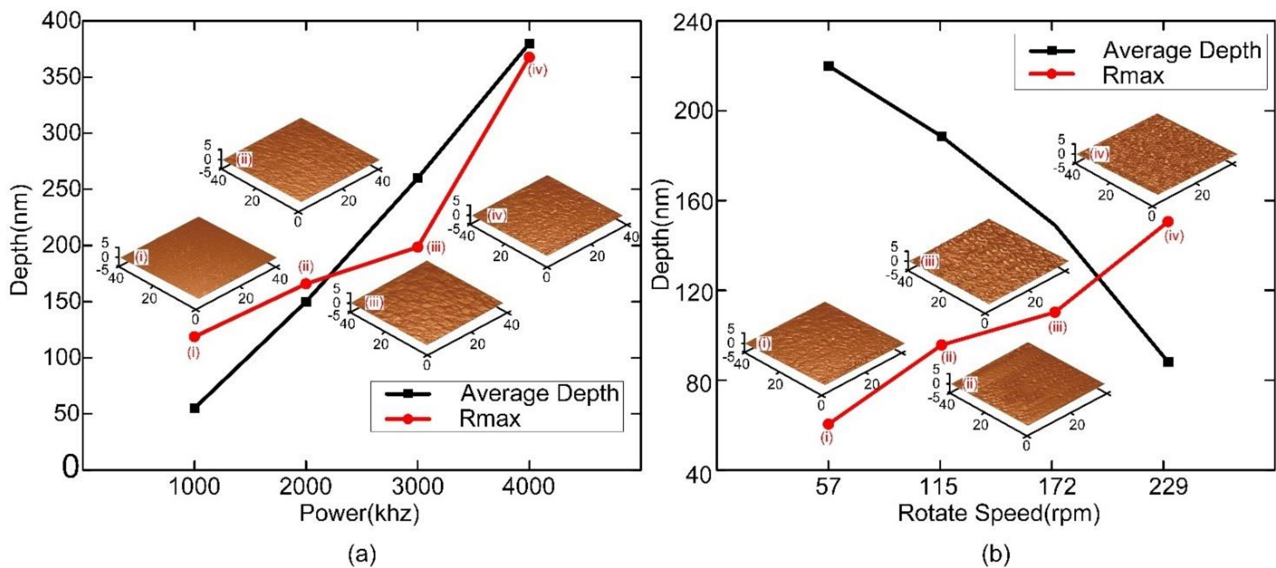

Figure 4-10 (a) Variation of mean depth and maximum roughness at different frequencies; (b) Variation of average depth and maximum roughness at different rotational speeds

4.5 Summary

The chapter begins by describing the constructed five-axis laser platform and experimental setup. A series of experiments were then conducted to compare the performance of DOE-based thinning against conventional Gaussian (GAU) beam thinning on both flat and non-flat silicon wafer surfaces.

For flat surfaces, the DOE-based method demonstrated significant improvements in surface morphology, creating smooth, flat-bottomed grooves compared to the wave-like pattern observed with GAU. Surface roughness measurements consistently showed lower values for DOE across different laser parameters, highlighting its ability to produce smoother surfaces. Material analysis revealed a crucial advantage of DOE in minimizing the formation of amorphous silicon and silicon dioxide, preserving the desirable properties of the silicon wafer. Furthermore, DOE-processed surfaces exhibited isotropic hydrophilicity, ensuring consistent wettability regardless of direction,

unlike the anisotropic behavior observed with GAU. These differences were attributed to the uniform energy distribution of the DOE beam, contrasting with the concentrated energy profile of the GAU beam. This was further confirmed by calculations showing a significantly lower peak energy density for the DOE beam.

Experiments on non-flat surfaces with pre-existing grooves demonstrated DOE's effectiveness in mitigating the regenerative effect, reducing both the depth and width expansion of the grooves compared to GAU. Moreover, DOE showcased superior thinning efficiency, achieving greater depth and completing multiple passes in the same timeframe as a single GAU pass.

Finally, the chapter explores the influence of key process parameters on DOE-based thinning. Increasing the pulse frequency led to greater material removal but also increased surface roughness, while decreasing the rotational speed resulted in smoother surfaces but at the cost of reduced cutting depth. These findings highlight the importance of parameter optimization to achieve the desired balance between surface quality and machining efficiency. Overall, Chapter 4 provides strong experimental evidence supporting the superiority of the DOE-based rotary laser thinning technique for achieving high-quality and efficient silicon wafer thinning.

Chapter 5 Conclusion

This thesis introduces a novel approach to rotary laser thinning of silicon wafers based on DOE, aimed at improving the surface quality and efficiency in semiconductor manufacturing. The study encompassed various stages, including the design and fabrication of a DOE (Section 3.3), the development of a customized five-axis laser processing platform (Section 4.1), and the comparative analysis of DOE-based laser thinning with conventional GAU beam thinning on both flat and non-flat silicon wafer structures (Sections 4.2 & 4.3). Subsequently, the influence of key process parameters, namely pulse frequency and rotation speed, was investigated to optimize the DOE laser thinning process (Section 4.4).

5.1 Research outcomes

The main research findings of this thesis can be summarized as follows:

(i) **DOE-Based Linear Spot Generation:** A customized DOE component and a five-axis laser processing platform were designed and implemented to generate linear laser spots with uniform energy distribution. This approach significantly enhanced processing efficiency compared to conventional Gaussian beams.

(ii) **Enhanced Surface Quality:** Experiments demonstrated that DOE-based linear spots significantly reduce surface roughness and generate smoother surfaces compared to traditional Gaussian beam processing.

(iii) **Improved Material Behaviour:** XRD and EDS analyses revealed a marked decrease in the formation of amorphous silicon and oxides on DOE-processed surfaces. This indicated that DOE-based laser beam can better control crystallinity and oxidation levels compared to Gaussian beam processing.

(iv) **Reduced Regenerative Effects:** The DOE-based method reduced the regenerative effects commonly encountered in traditional laser processing. In terms of both depth and width, regenerative effects were reduced by 41% and 59%, respectively.

(v) **Superior Surface Hydrophilicity:** Surfaces processed with DOE linear spots exhibited consistent

hydrophilicity in both feed and tangential directions, in contrast to the anisotropic wettability observed on Gaussian-processed surfaces.

(vi) **Optimal Processing Parameters:** An investigation into the influence of pulse frequency and rotational speed on machining depth and surface roughness revealed optimal processing parameters. High laser frequencies increased material removal and surface roughness, while low rotation speeds contributed to smoother surfaces with great depths.

5.2 Future works

Based on the findings of this thesis, we present the following future prospects:

(i) **Exploring DOE Designs for Complex Structures:** Investigating DOE designs that generate complex beam shapes beyond linear spots can enhances the versatility and applicability of this technique in processing intricate three-dimensional structures.

(ii) **Integration with Advanced Monitoring Techniques:** Integrating real-time monitoring techniques, such as optical emission spectroscopy or high-speed imaging, can provide valuable insights into the laser-material interaction dynamics and enable closed-loop control of the process for improved precision and efficiency.

(iii) **Expanding Applications:** Exploring the application of DOE-based laser thinning in other materials beyond silicon, such as ceramics or polymers, can open up new possibilities in various fields requiring high-quality surface precision machining.

(iv) **Investigating the Impact of Different DOE Materials:** Exploring the use of different DOE materials, such as fused silica or diamond, can lead to improved performance characteristics, such as higher diffraction efficiency and enhanced durability.

Reference

1. Kim, T. and J. Lee, *Fabrication and characterization of silicon-on-insulator wafers.* Micro and Nano Systems Letters, 2023. **11**(1).
2. Mariani, W.K.a.F., *Thinning and Singulation of Silicon: Root Causes of the Damage in Thin Chips* Electronic Components and Technology Conference, 2006.
3. Neuhaus, D.-H. and A. Münzer, *Industrial Silicon Wafer Solar Cells.* Advances in OptoElectronics, 2007. **2007**: p. 1-15.
4. *Processing technology of monocrystalline silicon wafer*. 2023; Available from: https://www.linkedin.com/pulse/processing-technology-monocrystalline-silicon-wafer.
5. Junduo Wang, Y.H., Lei Qian, Yameng Shan, and Wenjiang Shen, *A Method for Improving Heat Dissipation and Avoiding Charging Effects for Cavity Silicon-on-Glass Structures.* Actuators, 2023. **12**: p. 337.
6. Park, H., et al., *Surface Modifications for Light Trapping in Silicon Heterojunction Solar Cells: A Brief Review.* Transactions on Electrical and Electronic Materials, 2020. **21**(4): p. 349-354.
7. It. Liang , F.K., R. Sevilla, S. Anjur, *Wear phenomena in chemical mechanical polishing.* wear, 1997.
8. *Global Semiconductor Wafer Polishing and Grinding Equipment Market – Industry Trends and Forecast to 2028*. 2021; Available from: https://www.databridgemarketresearch.com/zh/reports/global-semiconductor-wafer-polishing-and-grinding-equipment-market.
9. *Semiconductor wafer polishing equipment market analysis*. 2023; Available from: https://exactitudeconsultancy.com/zh-CN/reports/21075/semiconductor-wafer-polishing-and-grinding-equipment-market/.
10. Chen, C.-C.A. and L.-S. Hsu, *A process model of wafer thinning by diamond grinding.* Journal of Materials Processing Technology, 2008. **201**(1-3): p. 606-611.
11. Camilletti, G.N.a.L.E., *Modeling of Chemical-Mechanical Polishing: A Review.* IEEE TRANSACTIONS ON SEMICONDUCTOR MANUFACTURING, 1995. **8**.
12. Mohammad, A.E.K. and D. Wang, *Electrochemical mechanical polishing technology: recent developments and future research and industrial needs.* The International Journal of Advanced Manufacturing Technology, 2016. **86**(5-8): p. 1909-1924.
13. Rangelo, I.W., *Dry etching-based silicon micro-machining for MEMS.* Vacuum, 2001. **63**: p. 279-291.
14. Gosálvez, M.A., I. Zubel, and E. Viinikka, *Wet etching of silicon*, in *Handbook of Silicon Based MEMS Materials and Technologies*. 2010. p. 447-480.
15. Huang, W., et al., *Surface topography and subsurface structure evolution in laser micro polishing of monocrystalline silicon.* Optics & Laser Technology, 2024. **177**.
16. Li, G., et al., *An experimental investigation of silicon wafer thinning by sequentially using constant-pressure diamond grinding and fixed-abrasive chemical mechanical polishing.* Journal of Materials Processing Technology, 2022. **301**.
17. Yang, K., et al., *Surface microtopography evolution of monocrystalline silicon in chemical mechanical polishing.* Journal of Materials Processing Technology, 2024. **328**.
18. Sun, J., et al., *Modelling and experimental study of roughness in silicon wafer self-rotating*

grinding. Precision Engineering, 2018. **51**: p. 625-637.

19. Zhang, X.H., Z.J. Pei, and G.R. Fisher, *A grinding-based manufacturing method for silicon wafers: generation mechanisms of central dimples on ground wafers.* International Journal of Machine Tools and Manufacture, 2006. **46**(3-4): p. 397-403.
20. Gao, S., et al., *Warping of silicon wafers subjected to back-grinding process.* Precision Engineering, 2015. **40**: p. 87-93.
21. Gao, S., et al., *Edge chipping of silicon wafers in diamond grinding.* International Journal of Machine Tools and Manufacture, 2013. **64**: p. 31-37.
22. Cheng, J. and Y.D. Gong, *Experimental study of surface generation and force modeling in micro-grinding of single crystal silicon considering crystallographic effects.* International Journal of Machine Tools and Manufacture, 2014. **77**: p. 1-15.
23. Pei, Z.J., et al., *A grinding-based manufacturing method for silicon wafers: an experimental investigation.* International Journal of Machine Tools and Manufacture, 2005. **45**(10): p. 1140-1151.
24. Xie, L., et al., *Mechanical wear behavior between CeO2(100), CeO2(110), CeO2(111), and silicon studied through atomic force microscopy.* Tribology International, 2021. **153**.
25. Gao, P., et al., *Non-spherical abrasives with ordered mesoporous structures for chemical mechanical polishing.* Science China Materials, 2021. **64**(11): p. 2747-2763.
26. B.J. Hoopera, G.B., S. Galliganb, *Pad conditioning in chemical mechanical polishing.* 2002.
27. Zhang, Z., Z. Jin, and J. Guo, *The effect of the interface reaction mode on chemical mechanical polishing.* CIRP Journal of Manufacturing Science and Technology, 2020. **31**: p. 539-547.
28. Chen, X., Y. Zhao, and Y. Wang, *Modeling the effects of particle deformation in chemical mechanical polishing.* Applied Surface Science, 2012. **258**(22): p. 8469-8474.
29. a, S.-S.P. and C.-H.C.b.c. , Yoomin Ahn c,, *Hydrodynamic analysis of chemical mechanical polishing process.* Tribology International, 2000.
30. Forsberg, M., *Effect of process parameters on material removal rate in chemical mechanical polishing of Si(100).* Microelectronic Engineering, 2005. **77**(3-4): p. 319-326.
31. Kwon, D., H. Kim, and H. Jeong, *Heat and its effects to chemical mechanical polishing.* Journal of Materials Processing Technology, 2006. **178**(1-3): p. 82-87.
32. Wang, W., et al., *Chemical–Mechanical Polishing of 4H Silicon Carbide Wafers.* Advanced Materials Interfaces, 2023. **10**(13).
33. Lee, H., H. Kim, and H. Jeong, *Approaches to Sustainability in Chemical Mechanical Polishing (CMP): A Review.* International Journal of Precision Engineering and Manufacturing-Green Technology, 2021. **9**(1): p. 349-367.
34. Chen, Y.-L., et al., *The technology combined electrochemical mechanical polishing.* Journal of Materials Processing Technology, 2003. **140**(1-3): p. 203-205.
35. Yang, X., et al., *Highly efficient planarization of sliced 4H–SiC (0001) wafer by slurryless electrochemical mechanical polishing.* International Journal of Machine Tools and Manufacture, 2019. **144**.
36. Yang, X., et al., *Novel SiC wafer manufacturing process employing three-step slurryless electrochemical mechanical polishing.* Journal of Manufacturing Processes, 2021. **70**: p. 350-360.
37. Murata, J., K. Yodogawa, and K. Ban, *Polishing-pad-free electrochemical mechanical polishing of single-crystalline SiC surfaces using polyurethane–CeO2 core–shell particles.* International Journal of Machine Tools and Manufacture, 2017. **114**: p. 1-7.

38. Luo, Y., et al., *Chemical mechanical polishing exploiting metal electrochemical corrosion of single-crystal SiC.* Materials Science in Semiconductor Processing, 2022. **152**.
39. Inada, N., et al., *Sustainable Electrochemical Mechanical Polishing (ECMP) for 4H-SiC wafer using chemical-free polishing slurry with hydrocarbon-based solid polymer electrolyte.* Applied Surface Science, 2024. **664**.
40. Murata, J., K. Hayama, and M. Takizawa, *Environment-friendly electrochemical mechanical polishing using solid polymer electrolyte/CeO2 composite pad for highly efficient finishing of 4H-SiC (0001) surface.* Applied Surface Science, 2023. **625**.
41. Yang, X., et al., *Selective electrochemical mechanical polishing of 4H–SiC surface employing porous material impregnated with electrolyte.* Ceramics International, 2023. **49**(22): p. 34569-34581.
42. Yang, X., X. Yang, and K. Yamamura, *Effects of electrolyte type and concentration on the anodic oxidation of 4H-SiC (0001) in slurryless electrochemical mechanical polishing.* Electrochimica Acta, 2024. **474**.
43. Baik, K.H. and S.J. Pearton, *Dry etching characteristics of GaN for blue/green light-emitting diode fabrication.* Applied Surface Science, 2009. **255**(11): p. 5948-5951.
44. Cecchetto, L., et al., *Highly textured multi-crystalline silicon surface obtained by dry etching multi-step process.* Solar Energy Materials and Solar Cells, 2013. **116**: p. 283-290.
45. Lee, J., H.W. Lee, and K.-H. Kwon, *Characteristics of etching residues on the upper sidewall after anisotropic plasma etching of silicon.* Applied Surface Science, 2020. **517**.
46. Streller, U., et al., *Photon-induced dry etching of Si(100) in the VUV.* Applied Surface Science, 1996. **96-98**: p. 448-452.
47. Han, C.-Y., et al., *Assessment of interface roughness during plasma etching through the use of real-time ellipsometry.* Applied Surface Science, 2011. **257**(7): p. 2536-2539.
48. Jiang, X., et al., *Kinetic etch front instability responsible for roughness formation in plasma etching.* Applied Surface Science, 2021. **543**.
49. Zhang, L., et al., *Highly efficient and atomic scale polishing of GaN via plasma-based atom-selective etching.* Applied Surface Science, 2023. **620**.
50. Heinke, R., et al., *Low surface damage laser processing of silicon by laser-induced plasma etching (LIPE).* Applied Surface Science, 2022. **597**.
51. Inoue, F., et al., *Influence of Si wafer thinning processes on (sub)surface defects.* Applied Surface Science, 2017. **404**: p. 82-87.
52. Zhou, S., B. Cao, and S. Liu, *Dry etching characteristics of GaN using Cl2/BCl3 inductively coupled plasmas.* Applied Surface Science, 2010. **257**(3): p. 905-910.
53. Chien, Y.-H.C., C.-C. Hu, and C.-M. Yang, *A Design for Selective Wet Etching of Si3N4/SiO2in Phosphoric Acid Using a Single Wafer Processor.* Journal of The Electrochemical Society, 2018. **165**(4): p. H3187-H3191.
54. Deng, Q., et al., *Effect of internal structure of a batch-processing wet-etch reactor on fluid flow and heat transfer.* Chinese Journal of Chemical Engineering, 2024. **72**: p. 177-186.
55. Monteiro, T., et al., *Dynamic Wet Etching of Silicon through Isopropanol Alcohol Evaporation.* Micromachines, 2015. **6**(10): p. 1534-1545.
56. Mohr, L., et al., *Numerical Simulation of an Entire Wafer Surface during Ozone-Based Wet Chemical Etching.* Industrial & Engineering Chemistry Research, 2020. **59**(40): p. 17680-17688.
57. Bauhuber, M., A. Mikrievskij, and A. Lechner, *Isotropic wet chemical etching of deep channels*

with optical surface quality in silicon with HNA based etching solutions. Materials Science in Semiconductor Processing, 2013. **16**(6): p. 1428-1433.

58. Zeng, Y., et al., *A new processing technique for fabrication of ultra-thin wafer.* The International Journal of Advanced Manufacturing Technology, 2018. **100**(5-8): p. 1287-1298.
59. Shin, D., et al., *Study on wet etching of dummy polysilicon in narrow pattern gap using alkaline solution.* Materials Science in Semiconductor Processing, 2022. **143**.
60. Habuka, H., S. Ohashi, and T. Kinoshita, *Numerical calculation model of a single wafer wet etcher using a swinging nozzle.* Materials Science in Semiconductor Processing, 2012. **15**(5): p. 543-548.
61. Qin, K. and Y. Li, *Mechanisms of particle removal from silicon wafer surface in wet chemical cleaning process.* J Colloid Interface Sci, 2003. **261**(2): p. 569-74.
62. F. Staudegger, M.W.H., and H.-J. Kruwinus, *Analyses and Modeling of a Wet-Chemical-Etch Process on Rotating Silicon Wafers with an Impinging Etchant Je.* The Electrochemical Society, 2009.
63. Chen, H., et al., *Improving polishing efficiency of RB-SiC through femtosecond laser pretreatment.* Applied Surface Science, 2023. **631**.
64. Yuan, C., et al., *Effects of incidence angle and optimization in femtosecond laser polishing of C/SiC composites.* Ceramics International, 2022. **48**(21): p. 32290-32304.
65. Zheng, Q., et al., *Investigation on ultrasonic vibration-assisted femtosecond laser polishing of C/SiC composites.* Journal of the European Ceramic Society, 2023. **43**(11): p. 4656-4672.
66. Wang, W., et al., *Surface morphology evolution mechanisms of laser polishing in ambient gas.* International Journal of Mechanical Sciences, 2023. **250**.
67. Zheng, Q., et al., *Influence of surface morphology and processing parameters on polishing of silicon carbide ceramics using femtosecond laser pulses.* Surfaces and Interfaces, 2023. **36**.
68. Shi, F., et al., *Polarized laser scattering detection of low-density and micron-scale subsurface cracks in silicon wafer.* Precision Engineering, 2024. **86**: p. 75-81.
69. Niitsu, K., et al., *Characterization of recrystallized depth and dopant distribution in laser recovery of grinding damage in single-crystal silicon.* Materials Science in Semiconductor Processing, 2018. **82**: p. 54-61.
70. Hallvard Angelskår, I.-R.J., Matthieu Lacolle, and Aasmund S. Sudbø, *Wood's anomalies and spectral uniformity of focusing diffractive optical elements.* 2010.
71. Liu, J., et al., *Diffractive micro-optical elements for implementing hollow beam and bi-focus simultaneously.* Optics & Laser Technology, 2008. **40**(7): p. 912-919.
72. Soria-Garcia, A., et al., *Fourier series diffractive lens with extended depth of focus.* Optics & Laser Technology, 2023. **164**.
73. Li, Y., et al., *Universal Polarization Transformations: Spatial Programming of Polarization Scattering Matrices Using a Deep Learning-Designed Diffractive Polarization Transformer.* Adv Mater, 2023. **35**(51): p. e2303395.
74. Pavelyev, V., et al., *Subwavelength Diffractive Optical Elements for Generation of Terahertz Coherent Beams with Pre-Given Polarization State.* Sensors (Basel), 2023. **23**(3).
75. Ramanujam, P.S., et al., *Polarisation-sensitive optical elements in azobenzene polyesters and peptides.* Optics and Lasers in Engineering, 2006. **44**(9): p. 912-925.
76. Tripathy, S.K., et al., *Holographic fabrication of polarization selective diffractive optical elements on azopolymer film.* Polymers for Advanced Technologies, 2000. **11**(8-12): p. 570-574.

77. Nakata, Y., M. Yoshida, and N. Miyanaga, *Parallel fabrication of spiral surface structures by interference pattern of circularly polarized beams.* Sci Rep, 2018. **8**(1): p. 13448.

78. Amako, J. and E. Fujii, *Beam delivery system with a non-digitized diffractive beam splitter for laser-drilling of silicon.* Optics and Lasers in Engineering, 2016. **77**: p. 1-7.

79. Tamulevičius, T., et al., *The calculation, fabrication and verification of diffraction grating based on laser beam splitters employing a white light scatterometry technique.* Optics and Lasers in Engineering, 2013. **51**(10): p. 1185-1191.

80. Wang, F., et al., *Distortion measurement of optical system using phase diffractive beam splitter.* Opt Express, 2019. **27**(21): p. 29803-29816.

81. Wang, C., et al., *Tunable beam splitter using bilayer geometric metasurfaces in the visible spectrum.* Opt Express, 2020. **28**(19): p. 28672-28685.

82. Wei, A.-C., W.-J. Chang, and J.-R. Sze, *A Side-Absorption Concentrated Module with a Diffractive Optical Element as a Spectral-Beam-Splitter for a Hybrid-Collecting Solar System.* Energies, 2020. **13**(1).

83. Wu, Y. and A. Ozcan, *Lensless digital holographic microscopy and its applications in biomedicine and environmental monitoring.* Methods, 2018. **136**: p. 4-16.

84. Xiong, J., et al., *Holo-imprinting polarization optics with a reflective liquid crystal hologram template.* Light Sci Appl, 2022. **11**(1): p. 54.

85. Pensia, L., M. Kumar, and R. Kumar, *A compact digital holographic system based on a multifunctional holographic optical element with improved resolution and field of view.* Optics and Lasers in Engineering, 2023. **169**.

86. Singh, A.K., et al., *Design and analysis of holographic optical elements for their use as couplers with appreciable efficiency at different optical transmission windows.* Optik, 2022. **261**.

87. Han, Y., et al., *Diffractive Beam Shaper for Multiwavelength Lasers for Flow Cytometry.* Cytometry A, 2021. **99**(2): p. 194-204.

88. Qi Li, H.G., Yunhua Dong, Zuochun Shen, Qi Wang, *Investigation of di�ractive optical element for shaping a Gaussian beam into a ring-shaped pattern.* Optics & Laser Technology, 1998. **30**: p. 511-514.

89. Weidong Qu, W.Q., H.G. Huarong Gu, and a.Q.T. and Qiaofeng Tan, *Design of refractive/diffractive hybrid optical elements for beam shaping with large diffraction pattern.* Chinese Optics Letters, 2016. **14**(3): p. 031404-31407.

90. M.R. Taghizadeh, P.B., K. BalluKder, A.J. Waddie, P. Rudman, N. Ross, *Design and fabrication of di!ractive elements for laser material processing applications.* Optics and Lasers in Engineering, 2000. **34**: p. 298-307.

91. Tan, Q., et al., *Fine design of diffractive optical element for true beam shaping.* Optik, 2001. **112**(8): p. 329-334.

92. Cwikla, M., R. Dziedzic, and J. Reiner, *Influence of Overlap on Surface Quality in the Laser Polishing of 3D Printed Inconel 718 under the Effect of Air and Argon.* Materials (Basel), 2021. **14**(6).

93. Tan, C., et al., *Morphology evolution mechanisms and localized structural modification of repaired sites on fused silica optics processed by CO2 laser rapid ablation mitigation.* Optics & Laser Technology, 2022. **147**.

94. Cha, D., D. Axinte, and J. Billingham, *Geometrical modelling of pulsed laser ablation of high performance metallic alloys.* International Journal of Machine Tools and Manufacture, 2019.

141: p. 78-88.